



**POLITECNICO**  
MILANO 1863

Scuola di Ingegneria Industriale e dell'Informazione

Master School in Mechanical Engineering

# **Bandwidth-optimized force platform for a multiaxial shaker**

Supervisor: Prof. Marco TARABINI

Co-Supervisors: Eng. Pietro MARZAROLI

Eng. Stefano MARELLI

M.Sc. thesis by

**Alberto Fontanieri**

ID number: 893758

Academic Year 2018/2019



# Acknowledgements

# Table of contents

Abstract .....	VIII
<i>Sommario</i> .....	VIII
Chapter 1	
Introduction and state of art .....	1
1.1 Shakers classification and main applications .....	1
1.1.1 Commercially available shakers.....	3
1.1.2 Shakers for research and safety applications.....	5
1.2 Serial and parallel robots: an overview .....	7
1.3 The current version of the ED shaker.....	9
1.4 Vibrations measurements for HSW.....	11
1.4.1 Vibrating phenomena and interaction with human body .....	11
1.4.2 Vibration work-related diseases and legislation.....	12
1.4.3 WBV and discomfort on standing people: the Shibata's experiment.....	13
1.4.4 Apparent mass experiments and WBV .....	14
1.5 Force measurements .....	15
1.5.1 Force sensors overview .....	15
1.5.2 Multiaxial load cells and their applications.....	16
1.5.3 The studies on the Stewart's platform as a force sensor .....	19
1.6 Purposes of this thesis .....	21
Chapter 2	
Shaker bandwidth optimization.....	22
2.1 Introduction and methods.....	22
2.2 Platform optimization.....	24
2.2.1 Thickness reduction.....	24
2.2.2 Double chamfering of platform external sides .....	26
2.2.3 Material changes .....	27
2.3 Connectors optimization .....	29
2.4 Shafts optimization.....	31
2.5 Wedges optimization.....	32
2.6 Effect of sliders stiffness .....	32
2.7 Other structural improvements.....	33
Chapter 3	
Platform optimization.....	35
3.1 Introduction and fixed kinematical parameters .....	35



---

3.2 Geometry optimization.....	36
3.3 Material choice.....	37
3.4 FEM model definition .....	38
3.4.1 Skins and orientation.....	38
3.4.2 Assembly.....	40
3.4.3 Constraints and mesh .....	41
3.5 Optimal parameter definition through FEM modal analysis.....	42
3.5.1 Number and pattern of skin layers .....	43
3.5.2 Thickness of the aluminum honeycomb layer.....	45
3.6 Effect of the apparent mass .....	48
3.7 Static model.....	50
3.7.1 Weight distributed on two footprints.....	50
3.7.2 Weight distributed on a single footprint.....	52
Chapter 4	
Static equilibrium of forces and instability .....	55
4.1 Introduction and previous works.....	55
4.2 Transportation of the forces acting on the structure.....	56
4.3 Singularities and conditioning problems.....	65
4.3.1 The Dwarakanath's studies on singularities.....	65
4.3.2 Conditions of instability of the old version of the shaker .....	66
Chapter 5	
Design of the force platform .....	69
5.1 Wheatstone's bridge and strain gauges overview .....	69
5.1.1 The Wheatstone's bridge.....	69
5.1.2 Strain gauge working principle .....	70
5.1.3 Configuration for axial strain measurement.....	71
5.2 Experimental equipment .....	72
5.3 Floor noise evaluation .....	73
5.4 Preliminary experiments .....	75
5.4.1 Strain gauges installation .....	75
5.4.2 Methodology .....	76
5.4.3 Results .....	77
5.4.4 Calibration curve.....	79
5.5 MonteCarlo simulations for error propagation.....	83
5.5.1 Methodology .....	83
5.5.2 Results .....	85

---

Chapter 6	
Discussion and future developments .....	88
6.1 Installation of strain gauge bridges on all the links .....	88
6.2 RC circuit for low-pass filter installation .....	88
6.3 Sensitivity improvement and amplification .....	89
6.3.1 Notch model .....	90
Conclusions and remarks .....	93
Appendix A	
Platform mechanical drawings .....	94
Appendix B	
MATLAB® script for instability .....	95
Appendix C	
MATLAB® script for MonteCarlo simulation .....	97
Bibliography .....	100

## List of figures

Figure 1: TeamCorporation's hydraulic shakers: a) Mantis™; b) The Cube®; c) Tensor™.....	3
Figure 2: MAST™ family's hydraulic shakers: a) Orthogonal; b) Hexapod.....	4
Figure 3: ED shakers: a) Sentek Electronics' MA-Series™; b) IMV Corporation's TS-Series™ ....	4
Figure 4: CALCE's M-DOF shaker (College Park, MD, United States).....	5
Figure 5: MAST™353 at INAIL Research Center (Monte Porzio Catone, Italy) .....	6
Figure 6: Industrial manipulators: a) Serial robot; b) Parallel robot .....	7
Figure 7: Clavel's Delta robots: a) Linear; b) Revolute.....	9
Figure 8: Current version of the ED shaker: a) Side view; b) Top view.....	9
Figure 9: Current version of the ED shaker: CAD model.....	10
Figure 10: MSDs: a) Causes for MSDs in the EU; b) Activities exposed to vibrations .....	12
Figure 11: Shibata's experimental test setup .....	13
Figure 12: Monoaxial load cells: a) Tension/Compression; b) Bending; c) Torsion.....	15
Figure 13: Tactile load cells: artificial fingers .....	15
Figure 14: Multiaxial load cells .....	16
Figure 15: Gough-Stewart's platform examples .....	18
Figure 16: Single DOF undamped mechanical system .....	22
Figure 17: Double-chamfered platform.....	27
Figure 18: Chamfering of the cubes: a) Sketch; b) Cubes on platform; c) Cubes on sliders .....	30
Figure 19: Shaft geometry: a) Current; b) Two millings; c) Four millings.....	31
Figure 20: Virtual springs on the sliders: a) Side view; b) Top view.....	32
Figure 21: Fixed kinematical parameters .....	35
Figure 22: The current platform: a) Top view; b) Bottom view.....	36
Figure 23: The new platform (top view).....	37
Figure 24: ABAQUS® - Local reference system of a skin.....	39
Figure 25: ABAQUS® - Composite layup: a) Pattern A; b) Pattern B.....	40
Figure 26: ABAQUS® - Sandwich panel model .....	41
Figure 27: ABAQUS® - Face-to-face positional constraint .....	41
Figure 28: ABAQUS® - Tie constraint .....	42
Figure 29: First Mode frequency vs Number of carbon fiber woven layers .....	45
Figure 30: First Mode frequency vs Total platform thickness .....	47
Figure 31: Matsumoto and Griffin: a) Human body scheme; b) FEM model of human body.....	49
Figure 32: ABAQUS® - Load application on two footprints: a) Model; b) Commands.....	51
Figure 33: Static loading, two feet - Max principal stress: a) Global top view; b) Bottom view.....	51
Figure 34: Static loading, two feet - Max deflection on the whole structure .....	52
Figure 35: Static loading, two feet - Max deflection on the platform only (Bottom view).....	52
Figure 36: Static loading, one foot - Max principal stress: a) Global top view; b) Bottom view ....	53
Figure 37: Static loading, one foot - Max deflection on the whole structure.....	53
Figure 38: Static loading, one foot - Max deflection on the platform only (Bottom view) .....	54
Figure 39: Link angles: a) $\theta_i$ on the xy plane; b) $\beta_i$ on the xz plane.....	56
Figure 40: Reference frames - a) Link centre: $\{x_L y_L z_L\}$ ; b) Bearings centre: $\{x_B y_B z_B\}$ .....	57
Figure 41: Reference frames - Cube centre: $\{x_C y_C z_C\}$ .....	58
Figure 42: Reference frames - Translations: $\{x_{BLC} y_{BLC} z_{BLC}\}$ , $\{x_{TLC} y_{TLC} z_{TLC}\}$ , $\{x_S y_S z_S\}$ .....	59
Figure 43: Reference frames - Central $\{x_P y_P z_P\}$ and peripheral $\{x_S y_S z_S\}$ frames on the platform	62
Figure 44: The old version of the shaker: a) Single link; b) Assembly.....	66
Figure 45: The Wheatstone's full bridge .....	69

---

Figure 46: Examples of strain gauges .....	71
Figure 47: Full bridge type III: a) Gauges arrangement on a beam; b) Electrical scheme.....	71
Figure 48: National Instruments' 9237 simultaneous bridge module .....	73
Figure 49: Floor noise evaluation - a) Setup; b) Top view; c) Bottom view.....	73
Figure 50: Floor noise evaluation - First series.....	74
Figure 51: Floor noise evaluation - Second series .....	74
Figure 52: Floor noise evaluation - Third series .....	74
Figure 53: Strain gauges installation on a link: a) Left view; b) Right view .....	76
Figure 54: Signal acquisition - Continuous series.....	77
Figure 55: Signal acquisition - First series.....	77
Figure 56: Signal acquisition - Second series .....	78
Figure 57: Signal acquisition - Third series .....	78
Figure 58: Signal acquisition - Scatterplot with error bands.....	80
Figure 59: Signal acquisition - Calibration curve and uncertainty bands (plot).....	82
Figure 60: Normal distributions from histograms for the measured force components.....	87
Figure 61: RC circuit for low-pass filter installation .....	89
Figure 62: Link geometry: a) Full section; b) Notched section .....	90
Figure 63: Notch coefficient $k_t$ diagram [65] .....	91
Figure 64: Measured forces vs Notch diameter for fixed strain values.....	91
Figure 65: Measured force vs Notch diameter for a fixed strain value of $0.763 \mu\epsilon$ .....	92

## List of tables

Table 1: Shakers classification.....	1
Table 2: Features of TeamCorporation’s shakers [3].....	3
Table 3: MAST™ 353 dimensions and rototranslational performances [9].....	6
Table 4: Features of serial and parallel robots [11].....	8
Table 5: Current masses of the shaker components.....	23
Table 6: First four vibration modes of the current shaker version.....	24
Table 7: Vibration modes - Platform thickness reduction.....	25
Table 8: Vibration modes - Double chamfering of platform external sides.....	27
Table 9: Material density and Young's modulus changes.....	27
Table 10: Vibration modes - Platform material changes.....	29
Table 11: Vibration modes - Chamfering of cubes external sides.....	30
Table 12: Vibration modes - Shafts milling.....	31
Table 13: Vibration modes - Wedges removal.....	32
Table 14: Vibration modes - Block of sliders rotation.....	33
Table 15: Vibration modes - Mixed modifications effects on bandwidth.....	34
Table 16: Elastic properties of aluminum honeycomb [59].....	37
Table 17: Elastic properties of HM carbon fiber [60] [61].....	38
Table 18: Pattern A for composite layup.....	40
Table 19: Pattern B for composite layup.....	40
Table 20: Relative tie constraints of composite layup.....	42
Table 21: Vibration modes - Changes in number and pattern of skin layers.....	44
Table 22: Vibration modes - Changes in total platform thickness.....	47
Table 23: Mass-normalized parameters for Matsumoto and Griffin’s model.....	49
Table 24: Vibration modes - Standing subject and platform.....	50
Table 25: HBM’s LY-41 10/120 strain gauge features.....	72
Table 26: Floor noise evaluation - Variance and RMS of the three series.....	75
Table 27: MeasLab© setup for signal acquisition.....	76
Table 28: Mean and standard deviation of the first series of signals.....	79
Table 29: Mean and standard deviation of the second series of signals.....	79
Table 30: Mean and standard deviation of the third series of signals.....	80
Table 31: Signal acquisition - Calibration curve and uncertainty bands (values).....	83
Table 32: MSEs from MonteCarlo simulations.....	85
Table 33: Normal distributions parameters of Figure 60.....	86
Table 34: Geometric and elastic properties of a link.....	90
Table 35: Measured force in function of notch diameter for a fixed strain value of $0.763 \mu\epsilon$ .....	92

# Abstract

## *Sommario*

The aim of this work is to improve the dynamic performances and the bandwidth of a novel multiaxial shaker, to be employed for measuring the three-dimensional apparent mass of a standing person subjected to vibrations. In particular, the first part of the thesis involves the employment of lightweight design principles and composite materials, with the aim of optimizing the mass and the stiffness of the moving parts of the structure: hence, a series of numerical simulations would address the most effective changes to be applied in order to enlarge the system bandwidth. Then, the second part of the work focuses on the implementation of a force measurement system to be installed on the same structure, intended to convert the shaker in a force-sensing platform. The proposed system would allow the measurement of the three spatial components of the force and torque vectors generated at the centre of the moving platform by a standing human body subjected to multiaxial vibrations, thus allowing the evaluation of its apparent mass.

*Il presente lavoro si propone di migliorare le prestazioni dinamiche e la banda passante di uno shaker multiassiale, atto a misurare la massa apparente tridimensionale di una persona in postura eretta soggetta a vibrazioni. Nel dettaglio, la prima parte della tesi si fonda sull'utilizzo dei principi del lightweight design e sull'impiego dei materiali compositi, con lo scopo di ottimizzare la massa e la rigidità delle parti sospese della struttura. Pertanto, grazie all'utilizzo di una serie di simulazioni numeriche, sono state individuate le modifiche più efficaci da apportare al sistema, al fine di incrementarne la banda passante. La seconda parte del lavoro, invece, prevede la trasformazione dello shaker in un sensore di forza, in grado di misurare, lungo i tre assi coordinati, le forze e i momenti generati da una persona in piedi soggetta a vibrazioni multiassiali, facilitandone così la determinazione della massa apparente tridimensionale.*

Keywords: multiaxial shaker, apparent mass, lightweight design, FEM simulations, force platform, MonteCarlo method.

# Chapter 1

## Introduction and state of art

### 1.1 Shakers classification and main applications

A shaker is a mechanical device that allows to perform vibration tests on an entity, either simulating the actual environmental conditions (*field-dependent testing*) or focusing on the product weaknesses that may lead to a failure (*product-dependent testing*) [1]. The shakers can be classified in function of the number of vibrating axes and of the actuating system that provides the excitation, as shown in Table 1:





Shakers classification		Actuating system	
		Hydraulic	Electrodynamic
Number of axes	Monoaxial		
	Multiaxial		

Table 1: Shakers classification

In detail, a *monoaxial shaker* (also called *linear*) can generate a mechanical oscillation, either sinusoidal, random or deterministic, along only one axis. The multiaxial response of the object to be tested is estimated as the sum of the responses along each direction of excitation. However, the concurrent effect of triaxial vibrations is often different from the sum of the effects due to subsequent uniaxial excitations. Moreover, being the latter highly dependent

on the time history of the excitation signal, a significant variance in time-to-failure can be observed. For these reasons, the *multiaxial shakers* have been developed, particularly succeeding in the aerospace and automotive fields, being pushed by the growing needs for product quality and in presence of particular tests, where [1]:

- A single attachment point could damage the test article when applying the loading forces (e.g. long missiles)
- The physical configuration of the unit under test required a greatly expensive fixture
- The required force was greater than the one available from a single shaker
- More waveforms needed to be simulated at the same time and at different locations of a large structure

Additionally, the multiaxial shakers further split into two main families, depending on the typology of actuating device. In particular [2]:

- *Hydraulic shakers*: the end-effector of the shaker is moved through hydraulic actuators, each one controlled by a servo-valve. The motion of the pistons is obtained through negative or positive voltage control, for downwards and upwards movements respectively, while the voltage signal is generated by means of a frequency generator.
- *Electrodynamic (ED) shakers*: each motor has a frequency generator that sends a signal to a current amplifier, thus creating an electromagnetic force. This force drives the armature of the shaker along the field coils, which are large polarized electromagnets within the shaker body.

The proposed classification groups the great part of the existing shakers, although some differences still hold between the industrial and academic worlds, due to different purposes and employment. Therefore, the subsequent paragraphs are intended to address some basic distinctions among the commercially available shakers and the devices for research applications, with particular mention to laboratories and testing centers.



### 1.1.1 Commercially available shakers

Nowadays, many different models of shakers are commercially available, each one suitable for specific testing purposes. In particular, the models gathered in Table 2, provided by one of the main manufacturers of the sector (*TeamCorporation*), can be assumed as a valid overview of the present state of art, with particular reference to the hydraulic devices [3]:

Performance Characteristics	Mantis™	CUBE®	Tensor™ (Servo-hydraulics)	Electro-dynamic Systems
Degrees of Freedom	6	6	6	6
Frequency Bandwidth	100Hz	250Hz	700Hz	2000Hz
Displacement Pk-Pk	150mm	100mm vert. 50mm horz.	13mm	Shaker Dependent
Payload, typical	50-2000Kg	25-500Kg	5-50Kg	Shaker Dependent
Max. force rating	315 kN	62 kN	36 kN	Shaker Dependent

Table 2: Features of TeamCorporation's shakers [3]

As inferred from Table 2, the values of force rating, stroke and admissible payload are strictly related, increasing with the size of the shaker. Instead, greater, heavier structures involve a narrower frequency bandwidth, that reduce the adaptability of the shaker to a wide range of testing fields. In Figure 1, the just-mentioned hydraulic shakers are shown:



Figure 1: TeamCorporation's hydraulic shakers: a) Mantis™; b) The Cube®; c) Tensor™

Furthermore, among the hydraulic shakers, the *MTS Systems'* trademark *Multiaxial Simulation Tables* (MAST™) includes bulky platforms, suitable for testing heavy structures at low or medium frequencies in presence of high forces and significant stroke length. Among them, the *orthogonal* platforms can reach up to 50 Hz of excitation, while the *hexapod* ones provide a bandwidth of 250 Hz [4]. Both the shakers are shown in Figure 2:

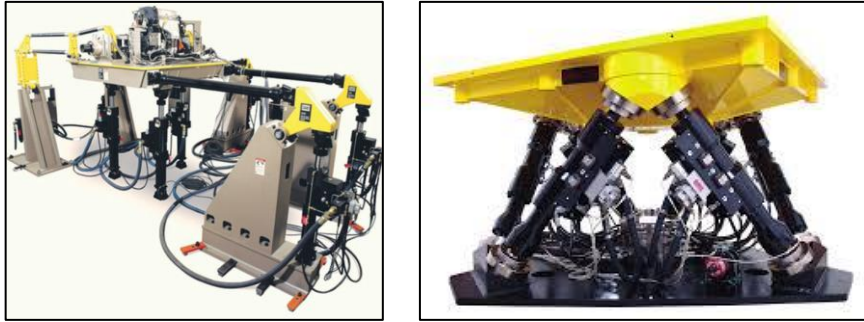


Figure 2: MAST™ family's hydraulic shakers: a) Orthogonal; b) Hexapod

Nowadays, for not particularly demanding applications, the electrodynamic shakers gained more popularity, because they are more compact and cost-effective than the hydraulic ones. In fact, with respect to the hydraulic devices, they require less maintenance, providing also a greater bandwidth of excitation and a faster response in frequency control [2].

Among the most important producers, *Sentek Electronics* developed the *MA-Series™*, in which three ED shakers provide the motion, through the application of forces that range from 10 to 60 kN, for a testing bandwidth of 2 kHz [5]. Similar devices have been proposed by *IMV Corporation*: their *TS-Series™* allow a high grade of customization, offering a broad selection of shakers that provide forces from 9 to 95 kN, and up to 1 kHz of excitation bandwidth [6]. Both the described products are then shown in Figure 3:

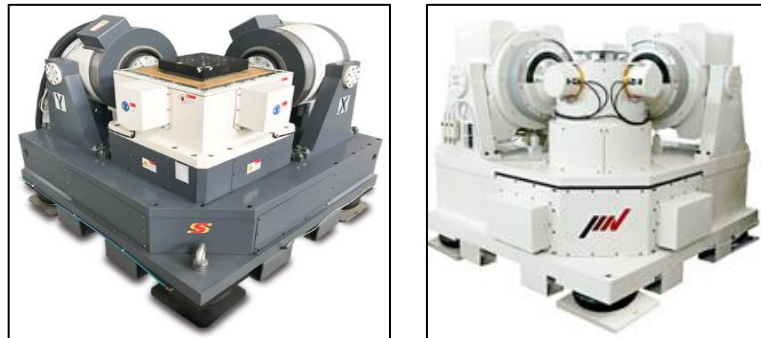


Figure 3: ED shakers: a) Sentek Electronics' MA-Series™; b) IMV Corporation's TS-Series™

After explaining the main features of the commercial devices, it is worth to move on the research laboratories, where shakers are employed for academic purposes or to perform on-commission tests for ministerial or public entities, especially in the *health and safety at work* (HSW) field.

### 1.1.2 Shakers for research and safety applications

As inferred from the previous paragraph, commercially available ED shakers can provide excitation over three axes at most, but in research laboratories also *multiple degrees of freedom* (M-DOF) systems have been developed. In fact, as stated in [7], the *Center for Advanced Life Cycle Engineering* (CALCE) in Maryland employs the particular ED shaker shown in Figure 4, employed for simulating the damages occurring in a battlefield context. The equipment is characterized by eight in-plane and four out-of-plane actuators, the latter lying under the table. This way, each one of the three axes has got four shakers that can be excited independently up to an acceleration of 30 G and a frequency of 3 kHz. Moreover, an excellent control of the excitation profile shape, jointly with the perfect coherence between the axes arises from the plots reported in [7]. All these features allow the identification of the main failure mechanisms of the system, by pointing out the DOF that stirs up higher damages to the components after a firefight in a battlefield.

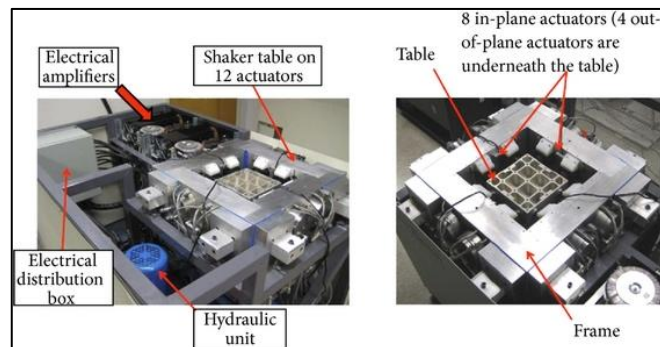


Figure 4: CALCE's M-DOF shaker (College Park, MD, United States)

Anyway, a multiaxial shaker would require a large amount of space and controlled field conditions to properly simulate the vibrating environment: therefore, only few laboratories own the adequate room to host a shaker as the one shown in Figure 5, located at the *Italian Workers' Compensation Authority* (INAIL) *Research Center* in Monte Porzio Catone, Rome. In this Institute, known for its research on work-related accidents and diseases, many vibration tests have been performed on standing and seated subjects, but also on medium-sized machinery, and then gathered in the *National Institute of Occupational Prevention and Safety* (ISPESL) vibration database, as mentioned in [8]. For these purposes, a hydraulic *MAST™ 353* has been employed, entailing a maximum payload of 680 kg, to be applied on a round table with a radius of 2 m, with a resonant frequency of 200 Hz. The shaker covers

an excitation range of frequencies from 0.1 to 100 Hz, while its dimensions and its rototranslational performances are shown in Table 3:

<b>Features</b>	<b>Direction</b>		
<b>Machine dimensions</b>	<b>Height</b>	<b>Width</b>	<b>Length</b>
Size	1.32 m	3.3 m	3.7 m
<b>Translational performance</b>	<b>Vertical</b>	<b>Lateral</b>	<b>Longitudinal</b>
Double amplitude displacement	300 mm	300 mm	200 mm
Velocity	1 m/s	0.9 m/s	0.9 m/s
Max acceleration (max payload)	4 G	3 G	3 G
Max acceleration (no payload)	6 G	6 G	5 G
<b>Rotational performance</b>	<b>Yaw</b>	<b>Pitch</b>	<b>Roll</b>
Tilting angle	$\pm 6.0^\circ$	$\pm 7.0^\circ$	$\pm 7.0^\circ$

Table 3: MAST™ 353 dimensions and rototranslational performances [9]



Figure 5: MAST™ 353 at INAIL Research Center (Monte Porzio Catone, Italy)

As mentioned before, not all the laboratories own the necessary room to host such a structure, also because, in order to avoid any undesired vibration, the optimal positioning for the shaker would be embedded in the ground, thus calling for a meter-deep dig on the floor.

For these reasons, alternative structural solutions have been developed to perform the same kind of tests and measurements, in order to optimize costs and space utilization. Many examples in this field exploit a robotic architecture, that provides compact devices with a high grade of customization, as explained in the brief overview proposed in the following paragraph.

## 1.2 Serial and parallel robots: an overview

According to the *Robotic Institute of America* (RIA), a robot can be defined as “a reprogrammable, multifunctional manipulator designed to move materials, parts, tools or specialized devices through variable programmed motions for the performance of a variety of tasks” [10]. These entities can be divided in two main categories:

- *Serial manipulators* (Figure 6a): consist in several links connected in series by various types of joints, typically revolute and prismatic. One end of the robot (called *base*) is fixed to the ground, while the other end (*end-effector*) is free to move in space. Typically, a gripper or a mechanical hand is attached to the *end-effector*.
- *Parallel manipulators* (Figure 6b): consist in two or more closed-loop kinematic chains in which the *end-effector* (mobile platform) is connected to the fixed *base* platform by, at least, two independent kinematic chains. Then, between the base and the end-effector platforms, some serial chains (called *limbs* or *legs*) are installed.



Figure 6: Industrial manipulators: a) Serial robot; b) Parallel robot

Moreover, Table 4 shows up the main differences between the two robot typologies. In detail, serial manipulators are suitable for repetitive tasks over long periods of time, operations in hazardous environments (exposed to nuclear radiation, performed underwater, related to space exploration...) and precision works with high degree of reliability. Some examples of their applications are welding, painting, polishing, injection molding, laser and plasma cutting, assembly, packaging and material handling. Instead, parallel robots ensure high accuracy, rigidity, speed and large load-carrying capability, although implying more complex kinematics, dynamics and smaller workspace. The current industrial applications

of parallel robots lie in fine positioning devices, simulators, moving platforms, machine tools, pick-and-place tasks, medical applications and force-sensing purposes [11].

<i>Feature</i>	<i>Serial robot</i>	<i>Parallel robot</i>
<i>Workspace</i>	<i>Large</i>	<i>Small and complex</i>
<i>Solving forward kinematics</i>	<i>Easy</i>	<i>Very difficult</i>
<i>Solving inverse kinematics</i>	<i>Difficult</i>	<i>Easy</i>
<i>Position error</i>	<i>Accumulates</i>	<i>Averages</i>
<i>Force error</i>	<i>Averages</i>	<i>Accumulates</i>
<i>Maximum force</i>	<i>Limited by minimum actuator force</i>	<i>Summation of all actuator forces</i>
<i>Stiffness</i>	<i>Low</i>	<i>High</i>
<i>Dynamics characteristics</i>	<i>Poor, especially with increasing the size</i>	<i>Very high</i>
<i>Modelling and solving dynamics</i>	<i>Relatively simple</i>	<i>Very complex</i>
<i>Inertia</i>	<i>Large</i>	<i>Small</i>
<i>Areas of application</i>	<i>A great number in different areas, especially in industry</i>	<i>Currently limited, especially in industry</i>
<i>Payload/weight ratio</i>	<i>Low</i>	<i>High</i>
<i>Speed and acceleration</i>	<i>Low</i>	<i>High</i>
<i>Accuracy</i>	<i>Low</i>	<i>High</i>
<i>Uniformity of components</i>	<i>Low</i>	<i>High</i>
<i>Calibration</i>	<i>Relatively simple</i>	<i>Complicated</i>
<i>Workspace/robot size ratio</i>	<i>High</i>	<i>Low</i>

Table 4: Features of serial and parallel robots [11]

Among the parallel manipulators, the Clavel's *Delta robot* is surely the most successful layout. This device is made up of two platforms (one fixed to the ground, one moving in space) mutually connected by a series of links. The moving platform is forced to remain parallel to the ground, by means of linkages arranged in a triple parallelogram structure. Additionally, in function of the joint typology, the *Delta robot* can be *linear* when it uses prismatic joints (the three translational DOFs are  $q_1$ ,  $q_2$  and  $q_3$ ), or *revolute* if it employs spherical joints (the three rotational DOFs are  $\theta_1$ ,  $\theta_2$  and  $\theta_3$ ). The two different typologies are then shown in Figure 7:



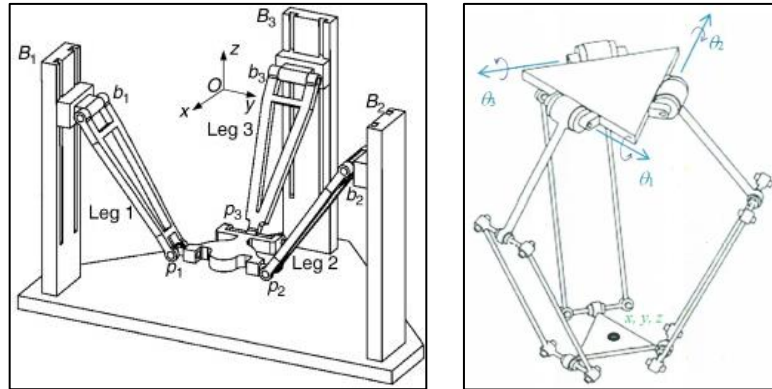


Figure 7: Clavel's Delta robots: a) Linear; b) Revolute

Hence, the compact design and the high stiffness of linear *Delta robots*, jointly with their identical performances on every horizontal working plane and the chance of a relatively large vertical displacement (up to 60 mm for the most common devices [12]), threw the basis for the development of the shaker hosted in Lecco Campus of *Politecnico di Milano*, starting point of the present work. This way, the room-related issues of multiaxial shakers have been partially solved.

### 1.3 The current version of the ED shaker

Starting from the design of a linear *Delta robot*, a novel multiaxial ED shaker has been developed by Marzaroli in 2017 [13]. This compact structure allows to perform laboratory tests without needing a dedicated room, thus saving on space and costs. In Figure 8, the current version of the shaker is displayed:

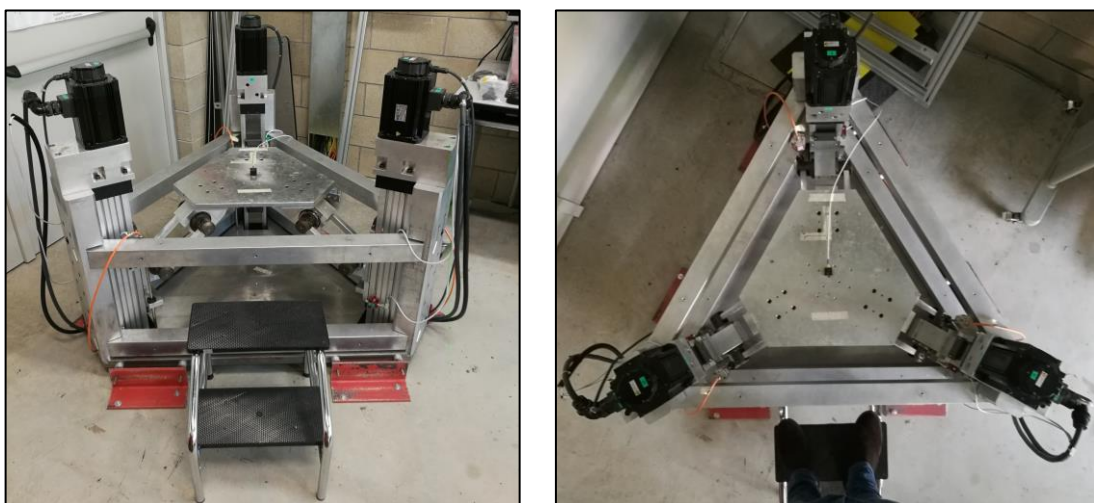


Figure 8: Current version of the ED shaker: a) Side view; b) Top view

Three brushless motors *OMRON R88M-M3K020C* (400 V, 3 kW) jointed to three ballscrews provide the actuation force. The ballscrews are held by aluminum vertical columns, which are placed on a grounded steel basement and linked each other by horizontal stiffening bars. Each actuator is equipped with a slider, that moves up and down proper guiding grooves on the columnar body. Then, an aluminum hollow cube is mounted on each slider, hosting two *SKF 32912*, tapered, single row roller bearings, whose inner ring is in contact with an aluminum shaft, properly modeled with two grooves at its extremities. In fact, each slot has to allow the in-plane rotation of the prismatic aluminum links, which occurs around a steel pin. This pin is connected to the shaft body by means of two *SKF BEP 7200*, angular contact, single row ball bearings. On the other extremity of each link, the same bearings, shafts, pins and cubes are installed: the latter cubes, then, are all connected to a moving platform by means of three aluminum wedges. Finally, the platform is made of an aluminum plate, with a thickness of 25 mm, presenting ribs and grooves on its bottom face, aimed to remove superfluous material and to maintain the right amount of stiffness [14]. Additionally, a *Computer Aided Design* (CAD) model of the shaker is shown in Figure 9:

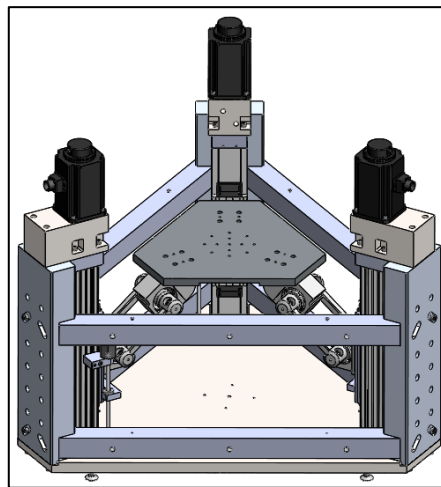


Figure 9: Current version of the ED shaker: CAD model

Then, once described the structural features of the current shaker, it is worth to underline its main functionalities. In fact, as mentioned in the paragraph 1.1.2, multiaxial ED shakers can be successfully employed in the measurement of vibrations that affect the human body, with special attention to the HSW. Thus, also this structure was initially intended to perform this kind of measurements, with particular reference to the *whole-body vibrations* (WBV), as inferred from the studies carried out by Marzaroli [13] and others [14] [15] [16]. Anyway, a



similar equipment can be also employed as an autonomous multiaxial force sensing structure, through a calibration process which would relate the measured loads to the actual ones. For these reasons, an overview of both vibration and force measurements will be provided in the next paragraphs.

## **1.4 Vibrations measurements for HSW**

### **1.4.1 Vibrating phenomena and interaction with human body**

Vibration is a mechanical phenomenon whereby oscillations occur around an equilibrium point, in a periodic or random fashion. Depending on which forces are acting on the body, two definition of vibration exist: *free vibration*, when only internal forces make the system oscillate, and *forced vibration*, when the phenomenon is caused by external forces [17]. Nowadays, the increasing usage of powerful tools in workplaces involves a higher generation and transfer of mechanical and acoustical vibrations to the human workers. Indeed, the ground is able to damp only a portion of the vibration energy, while the remaining part inevitably reaches the nearby workers' bodies, compressing their tissues and organs [18]. Thus, scientific research [19] [20] grew its interest in this field, demonstrating that the most relevant parameters in the human-wave interaction are the exposure time, combined with frequency and magnitude of the vibration. Indeed, prolonged exposure, higher amplitudes and the presence of sudden shocks may represent a health risk for the human body, especially for the muscles. In fact, their contraction (voluntary or not) helps in the vibration energy absorption, but results in a local fatigue tension, which also wears the joints cartilage, whose purpose lies in smoothing the relative motion between bones and muscles themselves.

The effects of vibrations on humans range from simple stress and annoyance, to harmful mechanical damages, caused by resonance within various organs. Namely, resonance occurs when the vibration frequency and the natural frequency of a body coincide, thus generating large oscillations within the body itself, with potentially catastrophic effects. Moreover, each part of the body can act as a vibrating entity by itself, with its own range of resonance frequencies [21], which can be observed in a detailed table provided by Wieckowski [22]. The assumption of independent behavior of the body parts is valid for excitation frequencies that range from 2 to 80 Hz, while for frequencies higher than this threshold, the damping

effect of the organs becomes predominant. Instead, for frequencies lower than 2 Hz, body will respond as a homogeneous and unique mass [23].

### 1.4.2 Vibration work-related diseases and legislation

Recent studies by the *European Agency for Safety and Health at Work* (EU-OSHA) [24] demonstrated that the prolonged standing position during the shifts and the poor ergonomic conditions of the workstations, led to a rise of *musculoskeletal disorders* (MSDs), which account for 38.1% of the occupational diseases in the *European Union* (EU). In particular, women suffer from MSDs more than men do, generally because occupied in manufacturing activities that require more repetitive tasks, although this fact is still underrecognized. Moreover, the same affection has a rising trend in younger workers, especially if employed in the services or in heavy industries. In detail, Figure 10a shows the main causes for MSDs in the EU, while Figure 10b displays the most exposed sectors of activities:

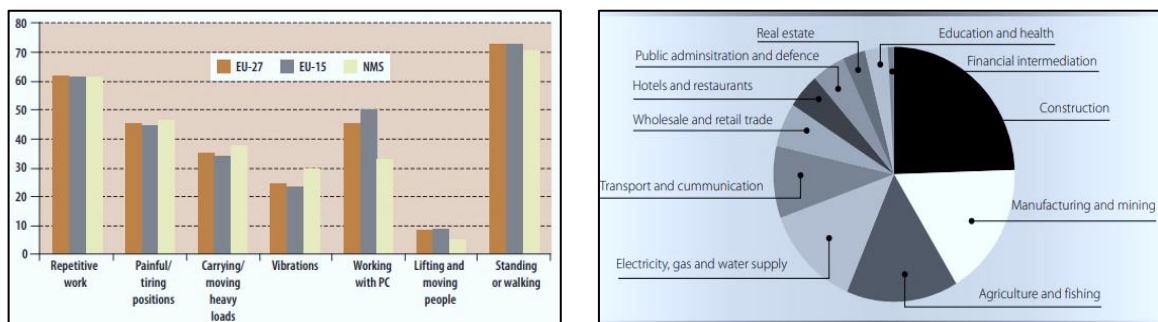


Figure 10: MSDs: a) Causes for MSDs in the EU; b) Activities exposed to vibrations

Among the main factors for MSDs in the EU, vibrations represent the sixth cause [24], mainly involving sectors like construction (63% of workers affected by), manufacturing and mining (44%), agriculture and fishing (38%), electricity, gas and water supply (34%) and transportation (23%) [25]. For these reasons, proper legislation has been adopted in order to regulate the working environments, providing minimum health and safety requirements and describing the methods and techniques for their evaluation.

Among them, the *Directive 2002/44/EC* of the European Parliament [26], actuated in Italy through the *Legislative Decree 81/2008, Section III* [27] establishes the daily exposure limits to *hand-arm system vibrations* (HAV) and *whole-body vibrations* (WBV), while other scientific studies also focused on the *foot-transmitted vibrations* (FTV) [18]. Namely, WBV is defined as “the mechanical vibration that, when transmitted to the whole body, entails

risks to the health and safety of workers, in particular lower-back morbidity and trauma of the spine”. Scientific literature too confirms that WBV are one of the main causes for MSDs onset, especially for low-back pain [28] [29] and ailments related to shoulders and neck [30].

The *International Standard ISO 2631-1:2014* [31], instead, provides methods and indexes for measuring the acceptance of the vibration levels that interfere with human body. It defines the reference systems to be adopted for measuring linear and rotational vibrations in different body positions, specifying that the origin (namely the contact point between the body and the vibration source) needs to host the transducer [18]. The standard also provides the frequency-weighting curves, which act as a filter on the obtained measurements, fitting them on a human-based scale [32]. Moreover, the *root mean square* (RMS) value of the signal, properly filtered through the frequency-weighting curves, is employed to compute the *vibration exposure*  $A(8)$  parameter, whose limit and action thresholds are provided by the Standard, in function of the exposure duration [17].

### 1.4.3 WBV and discomfort on standing people: the Shibata’s experiment

The most recent and complete study of the vibrational effects on standing subjects has been carried out by Shibata [33], with the aim of measuring the discomfort caused by fore-aft, side-side and vertical WBV. In detail, twelve people experienced three levels of acceleration ( $0.2; 0.4; 0.8 \text{ m/s}^2$ ) in three different directions and, at the end, they fulfilled a form on the perceived discomfort level, according to a semantic scale from 1 (Not uncomfortable) to 5 (Very uncomfortable), properly designed by the author. The experimental setup (Figure 11) consisted of a rigid platform, actuated by seven shakers (two powered in the lateral direction, four in the vertical, and the last in the fore-aft one). A feedback loop controlled the motion of the platform, thanks to seven accelerometers mounted on it.

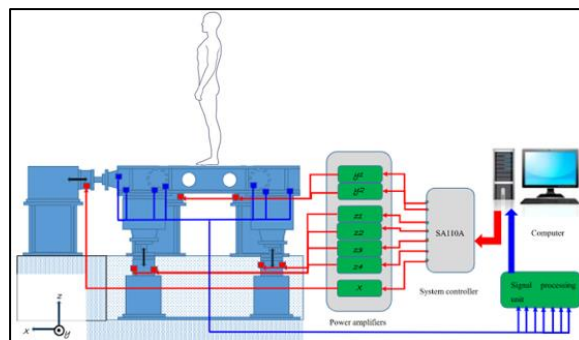


Figure 11: Shibata's experimental test setup

The obtained results showed that, for increasing levels of acceleration, the grade of discomfort raised for all the directions of excitation. Moreover, the highest discomfort ratings were registered for the vertical vibrations, then the fore-aft, then the lateral ones. Hence, Shibata demonstrated how to employ a shaker for WBV generation, but further attention needs to be paid on the response that human body offers to such excitation, jointly to the apparent mass effects, studied by Subashi et al. [34]. Indeed, the apparent mass matrix determination becomes crucial for correctly evaluating the human response to WBV, and many research studies have been addressed on it, mainly focusing on its nonlinearity [35].

#### **1.4.4 Apparent mass experiments and WBV**

When a structure supports a human body, the dynamic behavior of the two entities can mutually affect. In fact, in presence of a dynamic load, if one of the two entities start to vibrate, the other one would start too, as it happens when a man walks on a bridge, or when a shaker operates with a standing subject on it. In particular, when this occurs, the dynamic response of the overall system to the vibration can experience a 50–100% amplification of its expected value, due to the mutual excitation of the two entities, as in presence of a resonance phenomenon. In these conditions, the structure supporting the human body perceives its mass (thus known as *apparent*) as it was 1.5-2 times greater than its static value. Therefore, in a vibrational context, the only consideration of the static mass value can lead to an underestimation of the effect that the human body actually has on the structure [36]. According to Subashi et al. [34] and to Matsumoto and Griffin [36], the apparent mass value can be obtained from a series of experiments. Indeed, dynamic loads at five different magnitudes (0.125; 0.25; 0.5; 1; 2 m/s<sup>2</sup> RMS) and at random frequencies (from 0.5 Hz to 30 Hz) have been applied through a force platform to a subject standing on it, while accelerometers measured the perceived accelerations for each loading condition. Then, the ratio between the provided force and the measured acceleration for a specific frequency has returned the apparent mass value for that frequency of excitation. Finally, after performing the tests on twelve male subjects, the curves relating the ratio between apparent and static mass in function of the frequency have been derived, showing a resonating peak around 5 Hz. This meant that, for this frequency, the supporting platform perceived the mass of the standing subject as it was almost twice its static value.

Therefore, given that the apparent mass evaluation calls for the employment of a force platform, the present work aims for developing a similar structure, which would be able to measure multiaxial loads. Hence, in order to introduce the force measurements, an overview of the most common devices and applications has been provided in the next paragraphs.

## 1.5 Force measurements

### 1.5.1 Force sensors overview

The force sensors provide a measurement of the load acting on the structure where the sensor itself is placed. These sensors can be classified in three broad families, in function of the transmitted force and way of application [37]:

- *Monoaxial sensors* (Figure 12): they can quantify a force/torque applied in only one direction, starting from stress and strain values measured by uniaxial strain gauges mounted on a simple-shaped component. These sensors are cheap, stiff and robust and provide high resolution and reliability, making them suitable for highly accurate static force measurements.

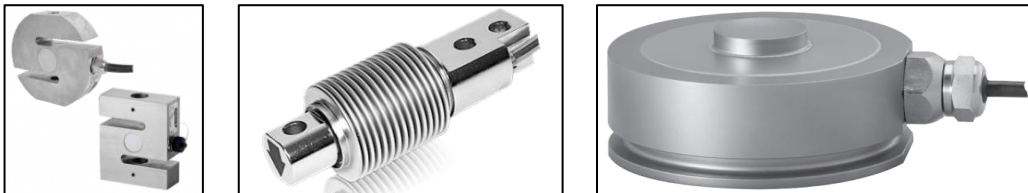


Figure 12: Monoaxial load cells: a) Tension/Compression; b) Bending; c) Torsion

- *Tactile force sensors* (Figure 13): the force is applied directly on the sensor, which provides a haptic feedback. Usually, arrays of pressure sensors or strain gauges cover the entire surface to be monitored (e.g. artificial skin), transmitting either pressure distribution or force/torque patterns. The tactile load cells have been used in robotics for contact force determination, grasping control and recognition of objects.



Figure 13: Tactile load cells: artificial fingers

- *Multiaxial sensors* (Figure 14): they can measure all the three components of force/torque vectors in space, through the evaluation of the reaction forces of the entity on which they are applied. The fullscale of this kind of sensors can reach the order of magnitude of thousands of Newton of force, and they are particularly suitable for the industrial applications.



Figure 14: Multiaxial load cells

### 1.5.2 Multiaxial load cells and their applications

Wind tunnel and thrust-stand-testing of rocket engines required multiaxial force transducers since 70s. In fact, the field conditions involved more loads acting on the testing items at the same time, and a monoaxial sensor would not be able to measure them all. Especially robotics witnessed a growing interest in these sensing devices, due to the request of increasingly autonomous and dexterous tasks. Indeed, any manipulator needs to be controlled in terms of positioning of the arms, but only a proper evaluation of the forces and torques acting on them can prevent from any failures due to overloads or fatigue [38]. Unlike the actuators, hidden inside the various parts of the robot, a multiaxial force/torque sensor is located externally, acting as an offshoot which acquires data through an intelligent system and transmits them to the processing unit of the manipulator. Obviously, the whole system is equipped with a compliant structure, which combines sensing elements inside a shielded cover with a flexible cable and the above-mentioned data acquisition center [37].

#### *Surgical and medical worlds: need for precision and sensitivity*

Especially surgical and medical rehabilitation worlds noticed great contribution from the adoption of the six-axis load cells. For example, the *Shiley Center for Orthopaedic Research & Education at Scripps Clinic* in La Jolla, CA [39] designed a total knee replacement tibial prosthesis as multiaxial sensor, in order to accurately measure the spatial components of tibial forces, thus evaluating the stress state of the implant. Moreover, in the plastic and

reconstructive surgery, the force sensing makes the surgeon aware of applied load on the delicate tissues and prevent him from damage them. Some examples involve the studies of Sommer on the measurement of deformations acting on adipose [40] or esophageal [41] tissues, respectively preventing from a shear excess that would imply unaesthetic scars on skin, or guiding the operation for the implantation of new tissues in babies with congenital defects. Then, research on force sensing of robotic hands has been carried out, thus connecting the worlds of surgery and industry, starting from the studies of Bejczy [42] and arriving to the most recent considerations about gripping items by Hogleve and Tracht [43]. In particular, in order to safely seize, push and pull an unknown object using intelligent fingers, the hand has to perceive the weight, which is calculated from measured forces/torques from a load cell installed on the wrist. G. Kim, in 2007 [44], stressed the fact that the existing manufactured sensors were not proper in size for being mounted on a robotic wrist, thus a six-axis load cell needed to be designed time by time. Few years later, Jacq et al. [45] demonstrated the opposite, proposing an innovative manufacturing process for wrist rehabilitation multiaxial load cells. This involved a steel base, on which piezoresistive load-sensing bridges were deposited, by means of single-film deposition or a foil bonding process, resulting in the so-called *thick-film technology*. Moreover, some new techniques involved the additive manufacturing of these sensors, reducing in a sensible way the production costs. Among these, K. Kim et al. [46] proposed their realization using *carbon nanotube* (CNT) and *thermoplastic polyurethane* (TPU) filaments, while Yao et al. [47] employed a fine Ti6Al4V powder deposition. Finally, in 2016, the same authors [48] elaborated a task-oriented design method on force compliant experiment of six-axis wrist load cells, based on force and moment ellipsoids.

### ***Industrial research world: need for stiffness and bandwidth increase***

The industrial world was initially wary towards such sensing techniques, mainly due to economic issues, complex interface, lack of support, and the need of installation in harsh conditions. In fact, an adequate sensor protection needed to be adopted, and other factors like noise, temperature stability, accuracy, data rates and interfacing methods could mean the difference between success and failure of some applications [49]. Moreover, in order to employ the same device for force measurements involving as many different objects as possible, a larger bandwidth would be necessary. In fact, the more heterogeneous are the

objects, the more various will be their range of natural frequencies. Therefore, for increasing the stability of the sensors and enhancing their versatility, a continuous improvement on the stiffness of the sensors has been carried out, in order to enlarge the testing bandwidth. Nowadays, the force measurements experienced growing interest in the industrial field, although the most important results still arrive from laboratory research for special purposes.

For example, research efforts of the last years focused on space applications, especially thanks to Chinese contributors, who studied about the new issues of the *Chinese Space Station* (CSS). In particular, Sun et al. [50] developed an interesting tool for completing space tasks, like maintenance, on-orbit assembly and support, manipulation assistance and payload care. Considering compatibility and dimension, they designed a six-axis force/torque sensor based on strain gauges, whose positions have been determined by strain distribution analysis on path. Instead, Chen et al. [51] proposed an elastic body based on cross-beam with anti-overloading capability, in order to obtain a large measurement range of force/torques. Then, optimization by *Finite Element Analysis* (FEA) has been carried out, so as to ensure both high stiffness and sensitivity of the six-axis force/torque sensor.

Furthermore, many of the research studies about multiaxial load cells are based on the Gough-Stewart's platform (Figure 15), a parallel manipulator with six prismatic actuators, attached in pairs to three points of the platform baseplate and to three other points on the upper end-effector. The joints can be spherical on the top and universal on the bottom, or all spherical. Devices placed on the top plate can be moved through the three linear translations  $x$ ,  $y$ ,  $z$  (lateral, longitudinal and vertical), and the three rotations (roll, pitch and yaw), corresponding to six DOFs. The original employment of this platform was the flight simulation, but further considerations about its applications as a force/torque sensor have been addressed in the following paragraph.

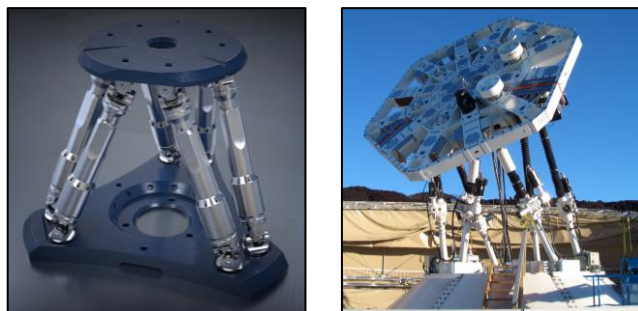


Figure 15: Gough-Stewart's platform examples



### 1.5.3 The studies on the Stewart's platform as a force sensor

Dasgupta [52] offered a review about the state of art of the Gough-Stewart's platform in 2000, including all the studies already developed about this apparatus. In particular, Gaillet and Reboulet [53] showed that the platform mechanism with articulated rods, each one carrying a sensing device, could measure force and torque acting on the mechanism, behaving like a six-axis load cell. Moreover, the Stewart's platform-based force sensor provided passive compliance, often needed during a robotic assembly task. Kerr [54], instead, instrumented the platform with elastic links, studying its behavior as a transducer.

However, both the previous studies have been developed in the 80s, by means of analytical techniques, that soon resulted in marked singularities of the Jacobian force transformation matrix. A research by Svinin and Uchiyama [55] demonstrated that the conditioning number of this compliance matrix could be used as a performance index. Though, the impossibility of reaching optimal values for this criterion has been stated for the regular polygon form-based sensors, while partial solutions of the optimization problem have been found out for the regular polyhedron form-based sensors, thus tending towards structural isotropy.

The latter results allowed the breakthrough of new numerical-based methods, looking for a better force control. As an example, Dwarakanath et al.' [56] design of the Stewart's platform intended minimizing the conditioning number of the 6x6 transformation matrix  $\mathbf{H}$ , which related the applied forces/torques vector  $\mathbf{W}$  (namely the platform generic *wrench*) and the  $\mathbf{F}$  vector containing the measured forces on the legs, according to the expression:

$$\mathbf{W} = \mathbf{H} \cdot \mathbf{F} \quad (1.1)$$

In particular, the study showed that the conditioning problem is strongly affected by the singularity of the matrix  $\mathbf{H}$ , which loses its maximum rank when the  $\mathbf{W}$  components are not perfectly balanced by the six leg forces included in  $\mathbf{F}$ , that become linearly dependent. This condition would result in highly uneven distribution of leg forces in response to loads in specific directions, thus strongly complicating the force control. For these reasons, the computation of the conditioning number would act as a warning procedure, in order to detect and correct any incipient singularity. Then, the structural design would involve the choice

of the leg shape, which could affect the sensor performances in terms of sensitivity, accuracy, repeatability and ease of strain gauges installation. The leg form could be obtained by maximizing the *signal-to-noise* (S/N) ratio, thus choosing the external load values that would exert the maximum axial force on each leg, inducing the maximum strain on it. Hence, another optimization problem would be formulated.

In another study proposed by Kang [38], instead, the calculation of the forces along the six legs has been carried out by means of the linear elastic theory. In fact, the six-axis force transducer based on the Stewart's platform was equipped with *linear voltage differential transformers* (LVDT) mounted along the legs, in order to measure the deflection of springs, which would be used for computing leg forces along the leg directions. All the calculations have been done assuming that the maximum displacement of the springs (i.e. the change of leg lengths) would be small enough, if compared to the leg length. Here too, a linear relationship between external wrench and forces upon the links has been proposed although, in this case, the Jacobian matrix has been expressed as a function of the end-effector position. However, an error analysis has been carried out, because the exact solution of forward kinematics, which would allow computing the position of the end-effector, was not available, thus calling for an approximated solution. Actually, the errors resulted in line with the noise levels related to the sensor features and the environmental changes, thus confirming the validity of the linear transformation matrix method, instead of deploying numerical-based methods for solving nonlinear equations.

Other interesting studies investigated the effects of singularities on a Stewart's force sensing platform, thus providing design strategies to prevent their occurrence. In this field, Jiang and Gosselin [57] aimed to determine the maximal singularity-free orientation workspace at a prescribed position of the Gough–Stewart's platform. Using the roll, pitch and yaw angles, the orientation workspace at a prescribed position could be defined by up to twelve workspace surfaces, derived through a numerical algorithm. This would allow to choose a proper set of parameters in design phase, thus avoiding singularities which would result in undesired effects on the project.

Finally, Ranganath et al. [58] confirmed that at near-singular configurations, small applied forces/torques in a certain direction could result in a mechanical magnification of the link forces. In fact, in such a condition, the parallel mechanism could gain one or more degrees

of freedom instantaneously. However, working near the singularity can be beneficial for designing a highly sensitive multiaxial force sensor: indeed, by means of flexural hinges, it is possible to naturally amplify the forces in the legs, in correspondence of small external forces and torques applied in certain directions.

## **1.6 Purposes of this thesis**

The aim of this thesis is to transform a pre-existing shaker into a force-sensing autonomous structure. Anyway, before deriving the static equilibrium equations, an optimization of the current structure in terms of bandwidth will be carried out. In fact, as specified in the paragraph 1.5.2, a larger bandwidth would allow testing objects at more excitation frequencies, thus increasing the force platform versatility. Therefore, in order to reach the 40 Hz that would allow testing the apparent mass of a person up to that frequency, studies on the reduction of the shaker mass have been performed, also paying attention to its structural stiffness. Indeed, only a stiff structure would ensure a linear relationship between the measured loads and the actually applied ones, thus allowing the design of a force sensing system as the ones proposed in the previous paragraphs.

# Chapter 2

## Shaker bandwidth optimization

### 2.1 Introduction and methods

In this chapter, a series of *Finite Element Method* (FEM) simulations have been performed, in order to detect the zones where the applied changes would result more effective in terms of bandwidth enlargement. In particular, the bandwidth of an instrument is the range of frequencies that span from 0 Hz to the frequency related to the first vibration mode, so the first resonant frequency of the instrument body. The latter is an inherent property of the structure, depending only on stiffness and mass of the involved body. In order to better understand this concept, it is worth to take a single DOF undamped mechanical system, made up by a spring and a mass, like the one of Figure 16:

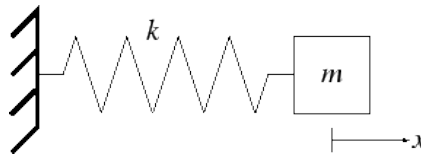


Figure 16: Single DOF undamped mechanical system

Solving the equation of motion for this system, it is possible to obtain two complex conjugate solutions expressed as angular speeds  $\omega$   $\left[\frac{rad}{s}\right]$ , depending on  $k$   $\left[\frac{N}{m}\right]$  and  $m$   $[kg]$  only, which easily let to obtain the natural frequency  $f$   $[Hz]$  as:

$$f = \frac{\omega}{2\pi} = \frac{1}{2\pi} \sqrt{\frac{k}{m}} \quad (2.1)$$

For a multibody system, instead,  $k$  and  $m$  are intended as generalized components of stiffness and inertia. In fact, the stiffness and inertia proper of each body composing the system, will take part in the determination of the first natural frequency of the overall multibody system. For these reasons, any change in the structural properties of a single body

can affect the vibrational behavior of the entire assembly, but it is necessary to determine in which measure this can happen. Moreover, given that bandwidth of an instrument includes all the frequencies up to the first resonant one, any increase in this latter value is needed for a bandwidth enlargement. Therefore, the reduction of the mass and the increase of the global stiffness of the system result worthwhile when attempting to enhance the bandwidth.

It is known that a reduction in mass is rather easier than an increase in stiffness, so the first efforts have been addressed in this direction. The analysis started with the evaluation of the mass of each existing component, in order to carry out improvements from the heavier to the lighter one, expecting a decreasing influence on the overall vibrational behavior. Table 5 reports the current mass values in decreasing order of mass:

<b>Item</b>	<b>Unitary mass [kg]</b>	<b>Quantity</b>	<b>Total mass [kg]</b>
Platform	12.61	1x	12.61
Cubes	1.28	6x	7.68
Shafts	1.23	6x	7.38
Wedges	1.36	3x	4.08
Links	0.35	6x	2.10

*Table 5: Current masses of the shaker components*

From Table 5 arises that the platform deserves more attention than the other components. Then, the cubes can be modified removing material from external surfaces, while the inner ones need to remain as they are, because designed to host the bearings. The same reasoning holds for the six shafts, where a little change in their structure would affect all the connected components, except for the central body. Finally, the wedges are intended to be completely removed, while the links result in a critical component which will be analyzed later.

In order to evaluate the effects of the adopted changes on the overall structure, a series of FEM analyses became necessary, because the structure revealed too complex to be studied analytically. These simulations have been focused on the lumped masses only, thus neglecting the presence of the basement, fixed to the ground and impossible to be modified. This helped in saving on computational cost, without influencing the final mode shapes. Moreover, no analysis has been performed on the bearings and their housings, because a change in their geometry would involve the complete redesign of the cluster linkages.

Finally, the first four modes of the current system have been evaluated and gathered in Table 6. This is intended as a benchmark for evaluating the effects of the applied modifications on the structure, and to testify that no mode inversion would ever occur.

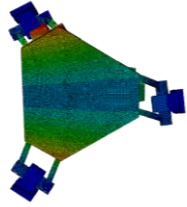
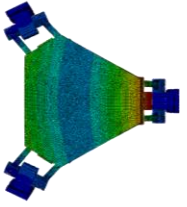
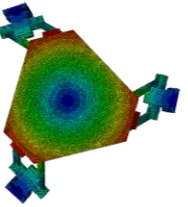
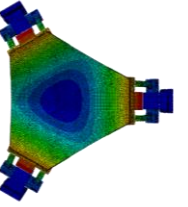
First four vibration modes of the current structure				
Structure	MODE 1 (Hz)	MODE 2 (Hz)	MODE 3 (Hz)	MODE 4 (Hz)
Current	32.7 	32.7 	39.9 	124.0 

Table 6: First four vibration modes of the current shaker version

## 2.2 Platform optimization

The actual platform has been realized starting from an aluminum block, flattened to a thickness of 25 mm and shaped as an irregular hexagon. These features have been replicated in the existing FEM model, which has been also divided in two layers in order to ease the meshing process. In particular, the upper part (15 mm thick) is made up of a solid section, whilst the lower one (10 mm thick) is designed as pattern of concentric ribs, a lighter structure intended to reduce the mass without undermining the stiffness.

Hereafter, a series of modifications have been carried out on the platform, starting with a simple reduction in thickness, followed by the tapering of the external sides, in order to diminish the rotating attitude in pitch and roll modes. Subsequently, some hypothetical changes in the material have been evaluated too.

### 2.2.1 Thickness reduction

In order to remove material more efficiently, the tests have been performed as a virtual milling of upper layer, through subsequent reductions of 2 mm of thickness. In Table 7, the first four mode shapes are shown, in function of the changing thickness:

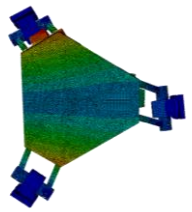
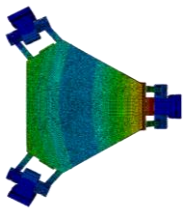
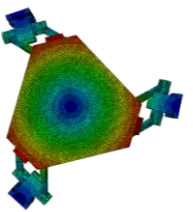
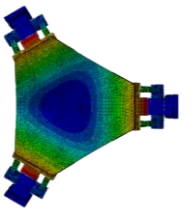
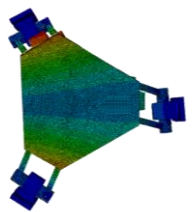
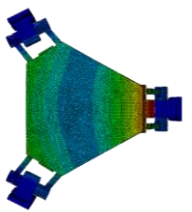
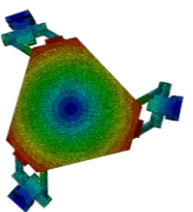
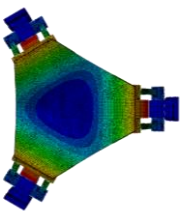
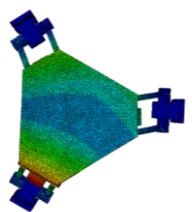
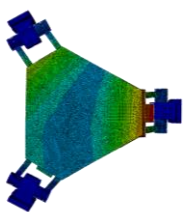
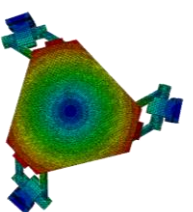
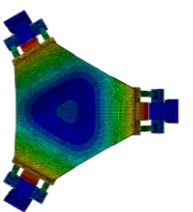
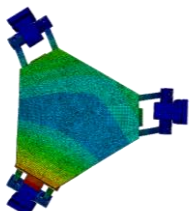
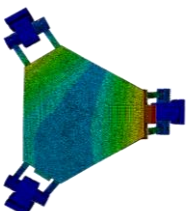
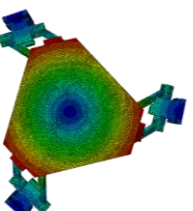
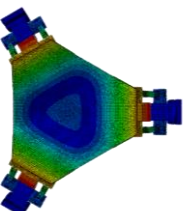
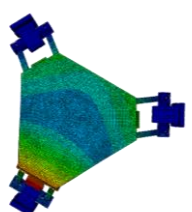
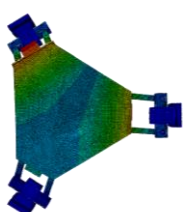
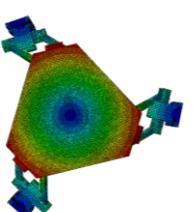
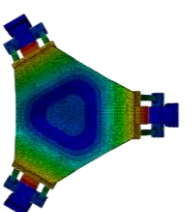
Vibration modes - Platform thickness reduction				
Thickness	MODE 1 (Hz)	MODE 2 (Hz)	MODE 3 (Hz)	MODE 4 (Hz)
23 mm	32.0 	32.0 	40.5 	112.1 
21 mm	30.5 	30.5 	41.1 	99.8 
19 mm	25.0 	25.0 	41.4 	75.2 
17 mm	23.1 	23.1 	42.1 	68.0 
15 mm	21.0 	21.0 	42.7 	60.2 

Table 7: Vibration modes - Platform thickness reduction

As inferred from Table 7, a reduction in the platform thickness would not be an efficient way for enlarging the bandwidth. In fact, on one hand, the mass is strongly decreased (linearly for the platform, nonlinearly for the whole assembly), but on the other hand the stiffness undergoes a decline too, resulting in an overall cut of the first mode frequency. For these reasons, the new modifications need to be addressed on a change in the platform shape, or in an alternative material employment.

### 2.2.2 Double chamfering of platform external sides

The second modification on the platform involved the double chamfering of its external sides, in order to obtain higher resistance to rotation. In fact, from the general expression of the kinetic energy of a body of mass  $m$  and rotational speed  $\omega$ :

$$E_K = \frac{1}{2} m \omega^2 R^2 = \frac{1}{2} I \omega^2 \quad (2.2)$$

it is possible to obtain the inertial moment  $I \left[ \frac{kg}{s^2} \right]$ , whose influence is more relevant for greater distances  $R [m]$  from the rotation axis, as its formulation shows:

$$I = mR^2 \quad (2.3)$$

In this case, the  $\omega$  of interest is the one corresponding to the natural frequency  $f$  of the body, according to the expression  $\omega = 2\pi f$ . Thus, in order to improve the bandwidth, it is worth to reduce the value of  $I$  so that, for the same amount of kinetic energy, the rotational speed  $\omega$  necessarily needs to raise. To be more effective, it is preferable acting on the sides, where the distance from the rotation axis is maximum, so to strongly limit the influence of the squared radius. For these reasons, the geometry has been modified using six couples of planes, mutually intersecting at the interface between the two platform layers, in order to obtain a taper angle of  $45^\circ$  on both sides. The obtained profile is then shown in Figure 17, as well as the vibration modes, gathered in Table 8:



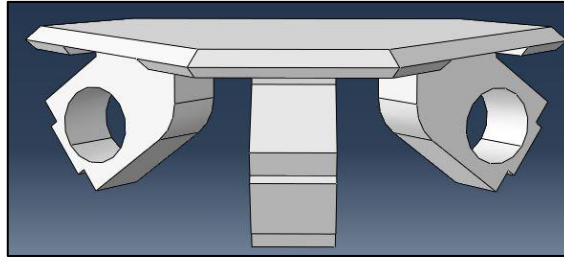


Figure 17: Double-chamfered platform

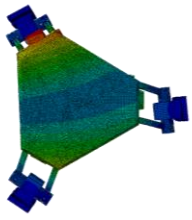
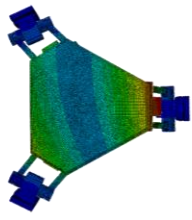
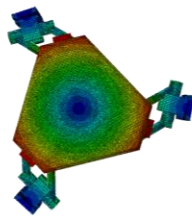
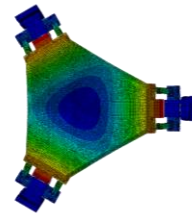
Vibration modes - Double chamfering of platform external sides				
Chamfer	MODE 1 (Hz)	MODE 2 (Hz)	MODE 3 (Hz)	MODE 4 (Hz)
45° x 45°	33.8	33.8	40.7	130.0
				

Table 8: Vibration modes - Double chamfering of platform external sides

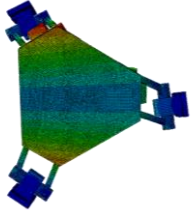
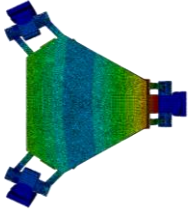
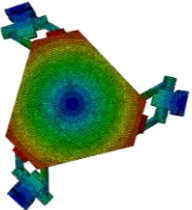
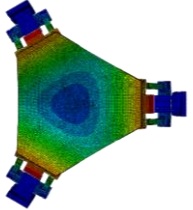
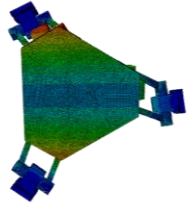
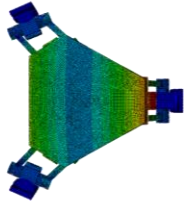
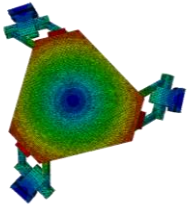
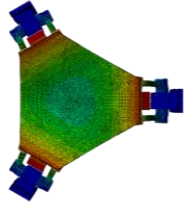
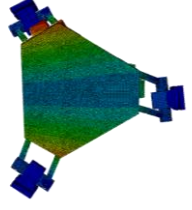
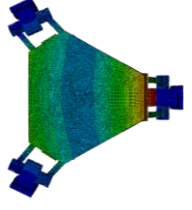
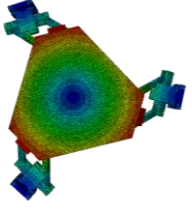
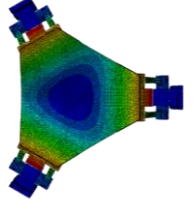
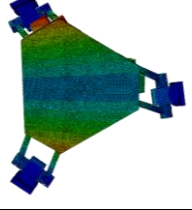
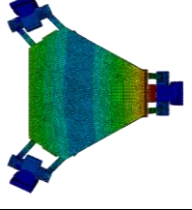
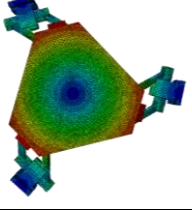
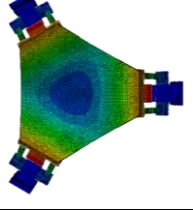
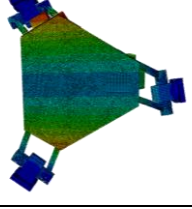
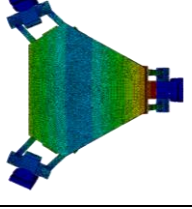
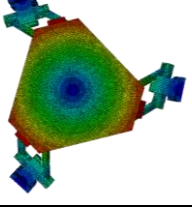
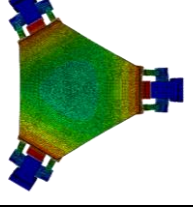
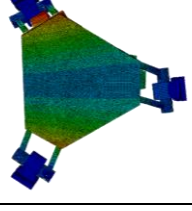
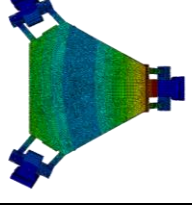
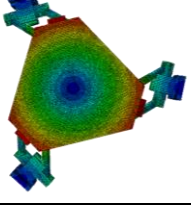
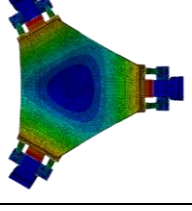
As inferred from Table 8, this solution revealed not so effective in the enlargement of the bandwidth, providing only a 3.4% improvement.

### 2.2.3 Material changes

In addition to the geometrical variants operated on the platform, the following analysis is intended to address a possible change of material. Indeed, another set of FEM simulations has been carried out (results in Table 10), combining the effects of a mass reduction and a stiffness increase, so as to show which variable was going to have more influence on the bandwidth improvement. In order to easily get the point, the mass value has been cut to 50% and to 20% through a reduction in density, while the stiffness value has been magnified two and five times, acting on the elastic modulus properties, as shown in Table 9:

<b>Mass</b>	$\rho_{\text{standard}}$ [ton/mm <sup>3</sup> ]	$\rho_{0.5x}$ [ton/mm <sup>3</sup> ]	$\rho_{0.2x}$ [ton/mm <sup>3</sup> ]
	2.81E-09	1.41E-09	0.56E-09
<b>Stiffness</b>	$E_{\text{standard}}$ [MPa]	$E_{2x}$ [MPa]	$E_{5x}$ [MPa]
	69000	138000	345000

Table 9: Material density and Young's modulus changes

Vibration modes - Platform material changes				
Properties	MODE 1 (Hz)	MODE 2 (Hz)	MODE 3 (Hz)	MODE 4 (Hz)
$\rho_{\text{standard}}$ $E_{2x}$	35.7 	35.7 	40.0 	162.4 
$\rho_{\text{standard}}$ $E_{5x}$	37.6 	37.6 	40.1 	210.8 
$\rho_{0.5x}$ $E_{\text{standard}}$	35.6 	35.6 	44.0 	131.9 
$\rho_{0.5x}$ $E_{2x}$	38.4 	38.4 	44.1 	174.2 
$\rho_{0.5x}$ $E_{5x}$	40.4 	40.4 	44.2 	230.8 
$\rho_{0.2x}$ $E_{\text{standard}}$	37.5 	37.5 	47.2 	137.5 

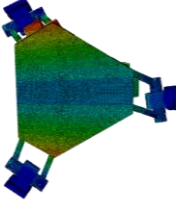
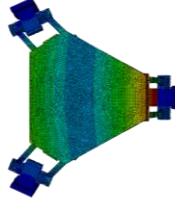
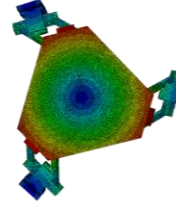
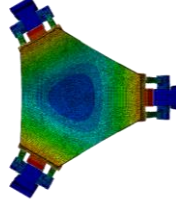
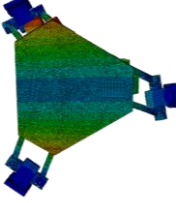
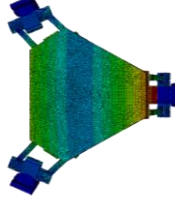
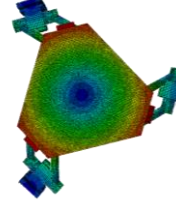
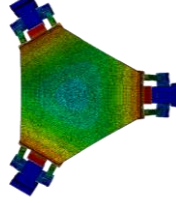
$\rho_{0.2x}$ $E_{2x}$	40.4 	40.4 	47.3 	182.6 
$\rho_{0.2x}$ $E_{5x}$	42.6 	42.6 	47.4 	245.7 

Table 10: Vibration modes - Platform material changes

From Table 10 arises that the same benefits on bandwidth are obtained either magnifying the stiffness or reducing the mass of the same coefficient, but leaving the other quantity to its standard value (i.e. 9% when halving the density or doubling elasticity, 14.8% when using 20% of standard density or a Young's modulus five times greater than the standard). Instead, mixing the effects of the two quantities would lead to a significant bandwidth improvement.

Therefore, a material change would be advisable, starting from a reduced density but without worsening the global stiffness of the system. From an economical point of view, the most suitable material would be the carbon woven fiber. Indeed, it shows great elastic properties in the direction normal to the in-plane texture, and a strongly reduced density with respect to aluminum. However, creating a platform with a thickness of at least 25 mm would imply many woven carbon layers, thus dramatically increasing the purchasing costs. For these reasons, an aluminum honeycomb insert would be ideal for connecting two carbon skins, saving on money and entailing a further improvement in terms of stiffness and density. Anyway, the features of the new materials will be better addressed in the next chapter.

### 2.3 Cubic connectors optimization

Knowing that the cubes need to host the bearings, the chance of redesign them in terms of material is strongly hindered, because of economic and technological issues. Anyway, adopting the little changes of Figure 18 (i.e. chamfering the external sides through a conventional milling process), a slight improvement would be perceived, as Table 11 shows.

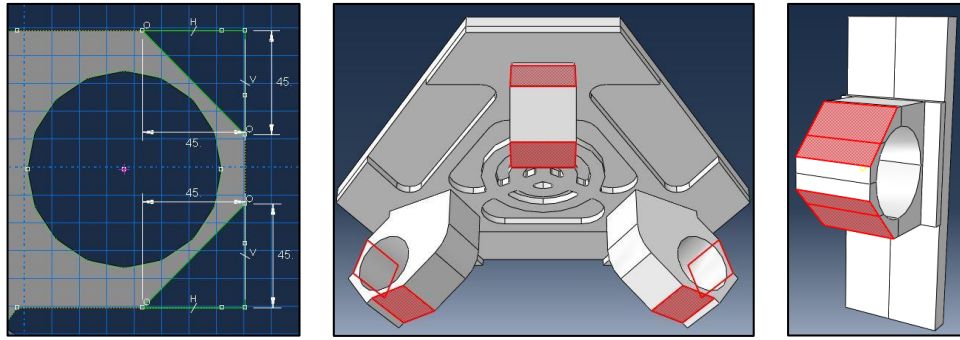


Figure 18: Chamfering of the cubes: a) Sketch; b) Cubes on platform; c) Cubes on sliders

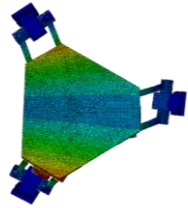
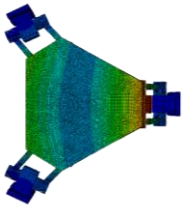
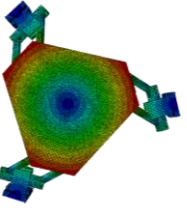
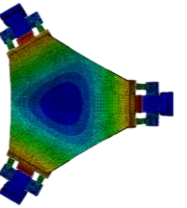
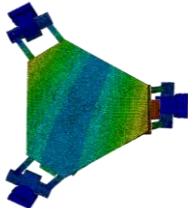
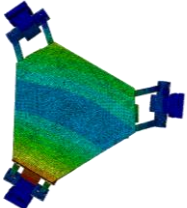
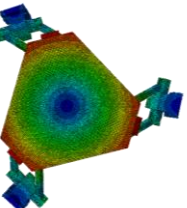
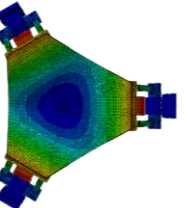
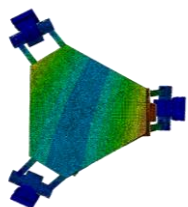
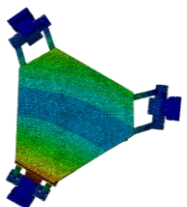
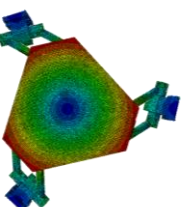
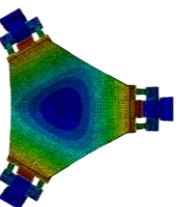
Vibration modes - Chamfering of cubes external sides				
Cubes location	MODE 1 (Hz)	MODE 2 (Hz)	MODE 3 (Hz)	MODE 4 (Hz)
On platform	34.3 	34.3 	41.0 	129.7 
On sliders	33.1 	33.1 	40.0 	124.0 
On platform and on sliders	34.3 	34.3 	41.2 	129.7 

Table 11: Vibration modes - Chamfering of cubes external sides

As inferred from Table 11, the cubes mounted on the sliders do not influence at all the bandwidth enlargement. In fact, chamfering only the cubes at the bottom of the platform, or chamfering all the six cubes of the structure, would lead to the same results, corresponding to a 4.9% bandwidth increase. Hence, the cubes located on the sliders will be left as they are.

## 2.4 Shafts optimization

The geometry of the six shafts is very complex (Figure 19a) because adapted for hosting the ball bearings that connect them to the cubes. Thus, the only changes can be performed on the central body, an aluminum full cylinder of diameter 56 mm and a length of 37 mm. In particular, a horizontal milling can be operated, first milling only two sides (Figure 19b) and then all the four sides (Figure 19c), leaving a central body with a squared section. The vibrational modes are then obtained and shown in Table 12.

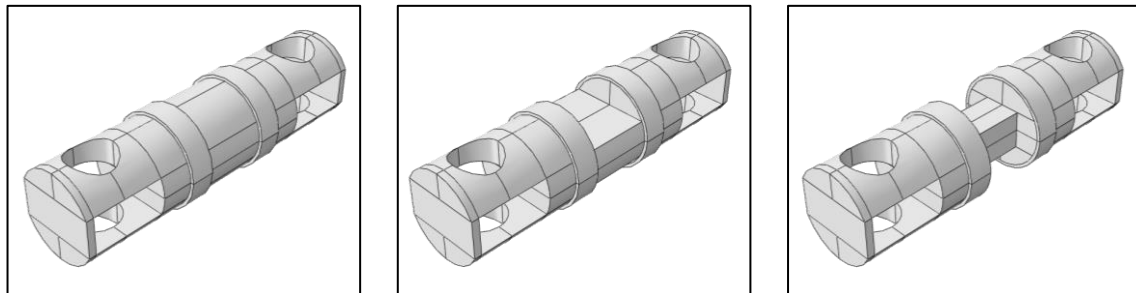


Figure 19: Shaft geometry: a) Current; b) Two millings; c) Four millings

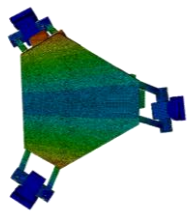
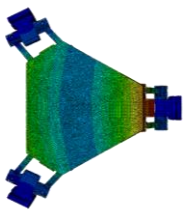
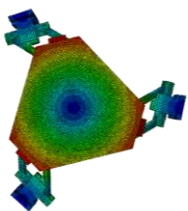
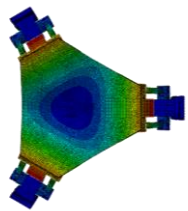
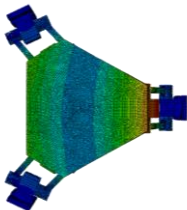
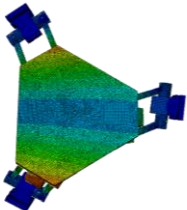
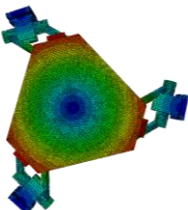
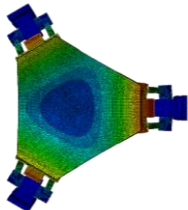
Vibration modes - Shafts milling				
Millings number	MODE 1 (Hz)	MODE 2 (Hz)	MODE 3 (Hz)	MODE 4 (Hz)
Two millings	33.2 	33.2 	40.2 	125.4 
Four millings	32.0 	32.0 	40.2 	122.4 

Table 12: Vibration modes - Shafts milling

Table 12 clearly shows that only minor improvements (1.5%) can be obtained through the milling of the six shafts, and only in the case of two millings. In fact, performing other two vertical millings to obtain a squared section of the central body, would result in worsening the current bandwidth by a 2.1%. For these reasons, the shafts have not been modified at all.



## 2.5 Wedges optimization

The three wedges were originally designed to connect the already existing platform to the cubes. On one hand, they avoided a global rethinking of the platform but, on the other hand, they added redundant mass to the structure, in spite of a little contribution in stiffness. For these reasons, after a series of geometrical modifications with no relevant outcome, the three wedges are intended to be eliminated through a smarter redesign of the platform. Thus, in order to simulate their absence, a very little value of density has been chosen. As shown in Table 13, the wedges removal would lead to a bandwidth improvement of 10.4%.

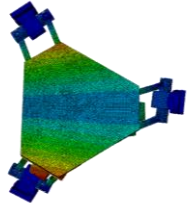
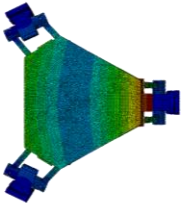
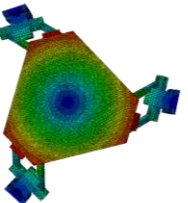
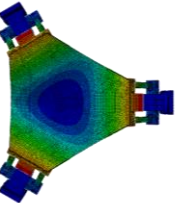
Vibration modes - Wedges removal				
Wedges	MODE 1 (Hz)	MODE 2 (Hz)	MODE 3 (Hz)	MODE 4 (Hz)
No wedges	36.1 	36.1 	42.7 	132.9 

Table 13: Vibration modes - Wedges removal

## 2.6 Effect of sliders stiffness

The three sliders that move along the guides of the basement have two degrees of freedom: one vertical translation, in order to accomplish their function of sliding, and one undesired rotation  $R_z$  around the axis of motion. This fact causes unwanted vibrations that, apart from mass and stiffness of the structure, are responsible for the bandwidth reduction. In order to represent this phenomenon, four rotational springs have been modeled at the corners of each slider (Figure 20), and their stiffness set to 5500 N/mm from experimental evidences [14].

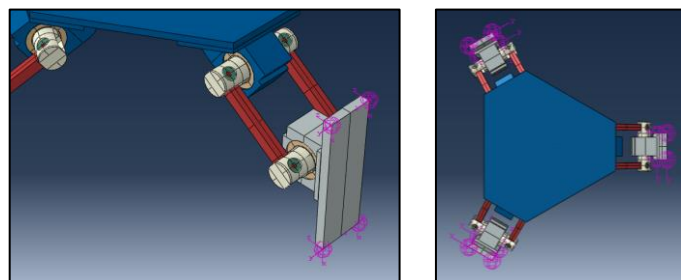


Figure 20: Virtual springs on the sliders: a) Side view; b) Top view

Of course, if  $R_z$  would be completely hindered, the first mode frequency should raise, thus enhancing the bandwidth. Hence, a clamp constraint has been applied on the back surfaces of the sliders, temporarily dismissing the virtual springs, leading to the results of Table 14:

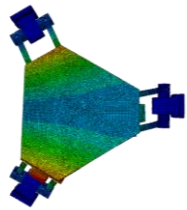
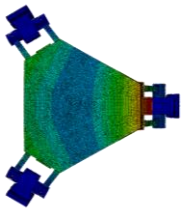
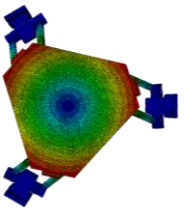
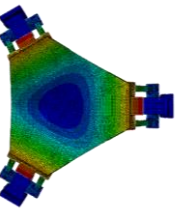
<b>Vibration modes - Block of sliders rotation</b>				
$R_z$	MODE 1 (Hz)	MODE 2 (Hz)	MODE 3 (Hz)	MODE 4 (Hz)
Blocked $R_z$	45.5 	45.7 	115.6 	124.4 

Table 14: Vibration modes - Block of sliders rotation

As inferred from Table 14, blocking the undesired motion would lead to 39.1% bandwidth enlargement.

## 2.7 Other structural improvements

According to the results of the previous sections, the most effective changes have been mixed in a new analysis, whose results have been provided in Table 15, in order to understand the reachable bandwidth improvement. In particular, the single modifications chosen are:

- Chamfering  $45^\circ \times 45^\circ$  of the platform
- Change of the platform material to five times larger stiffness and five times smaller mass
- Chamfering 45 mm x 45 mm of the cubes attached to the platform
- Two millings on the shafts
- Absence of the wedges
- Block of sliders rotation

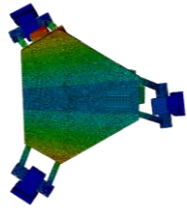
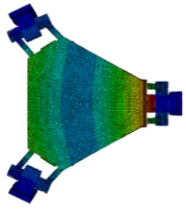
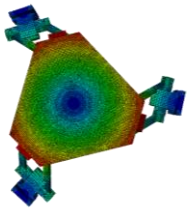
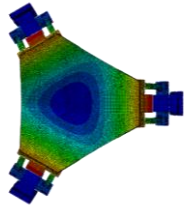
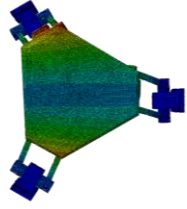
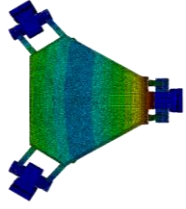
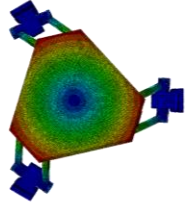
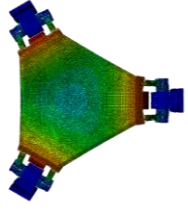
Vibration modes - Mixed modifications effects on bandwidth				
Structure	MODE 1 (Hz)	MODE 2 (Hz)	MODE 3 (Hz)	MODE 4 (Hz)
Current	32.7 	32.7 	39.9 	124.0 
Modified	85.2 	86.4 	179.2 	304.6 

Table 15: Vibration modes - Mixed modifications effects on bandwidth

As inferred from Table 15, the mixed modifications would enlarge the bandwidth up to 85.2 Hz, corresponding to an improvement of 160%. This means that the overall enhancement due to the concurrent changes is more effective than the sum of the single contributions taken individually. In particular, the first mode picture shows the complete hindering of the sliders rotation (blue color points out almost zero displacement in that zones), while in the fourth mode figure, the effect of the platform stiffening and lightening can be inferred (almost no blue zone at the centre, meaning about no downwards deflection). Anyway, it is important to remark that the vibrating behavior of the lumped masses system is strongly dependent on the basement, because directly connected to it by means of the three sliders. Consequently, blocking any undesired vibration on the shaker basement results of the utmost importance, in order to make the described modifications worthwhile. Summarizing, the simulations pointed out that minor changes on cubes and shafts would have a very low impact on the shaker bandwidth enlargement, thus they have been left as they are. Instead, blocking the undesired rotations  $R_z$  on the sliders would provide relevant enhancements, as well as the changes in the platform material or in the wedges removal, representing almost the 40% of the whole weight of the lumped masses (Table 5). For these reasons, a detailed redesign of the platform will be discussed in the next chapter, focusing on the wedges suppression and on the choice of new materials. Then, the optimization of the structural parameters will be carried out, in order to enlarge the shaker bandwidth as much as possible.



# Chapter 3

## Platform optimization

### 3.1 Introduction and fixed kinematical parameters

From the previous chapter arose that the current platform accounted for more than one third of the whole complex of lumped masses, reaching almost the 40% if considered jointed with the three aluminum wedges. Hence, trying first to remove redundant mass on these entities would be advisable in terms of bandwidth enlargement.

However, in order not to undermine the kinematic studies already performed on the structure [13], some geometrical features, like the length of the links  $l$  [mm] the platform radius  $R_p$  [mm] and the distance between the platform centre and the vertical guides  $s$  [mm] have been considered fixed, according to Figure 21:

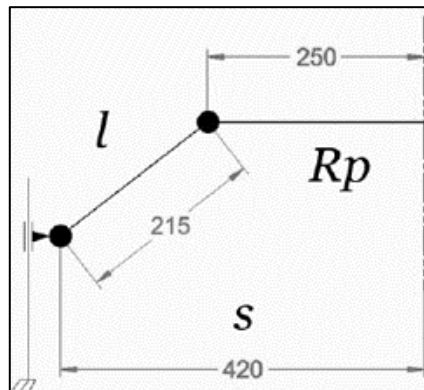


Figure 21: Fixed kinematical parameters

The platform, from a kinematic point of view, can be considered as a circle of radius  $R_p$ , representing the distance between the centre of the platform and the centre of the prismatic joints (i.e. the cubes), connected to the platform by means of the three wedges. However, the platform can assume any geometric shape, as long as this radius  $R_p$  remains fixed to 250 mm. For what concerns  $s$ , instead, the fixed basement can be seen as a reference frame, from which the centre of the platform needs to be 420 mm far in the zero-position.

### 3.2 Geometry optimization

The current platform (Figure 22) is made up of an aluminum irregular hexagon, ideally divided in two layers. The upper one, 15 mm thick, is constituted by a solid section, whilst the lower one, 10 mm thick, is designed as pattern of concentric ribs, a lighter structure which aims to reduce the mass without undermining the stiffness. Moreover, on the three short sides, three patterns of four holes each are needed to join the platform with the wedges, while three couples of small holes are designed for hosting centering pins. Instead, at the centre, the circular pattern of thirteen holes was initially employed for fixing mechanical devices for testing (e.g. accelerometers and little shakers).

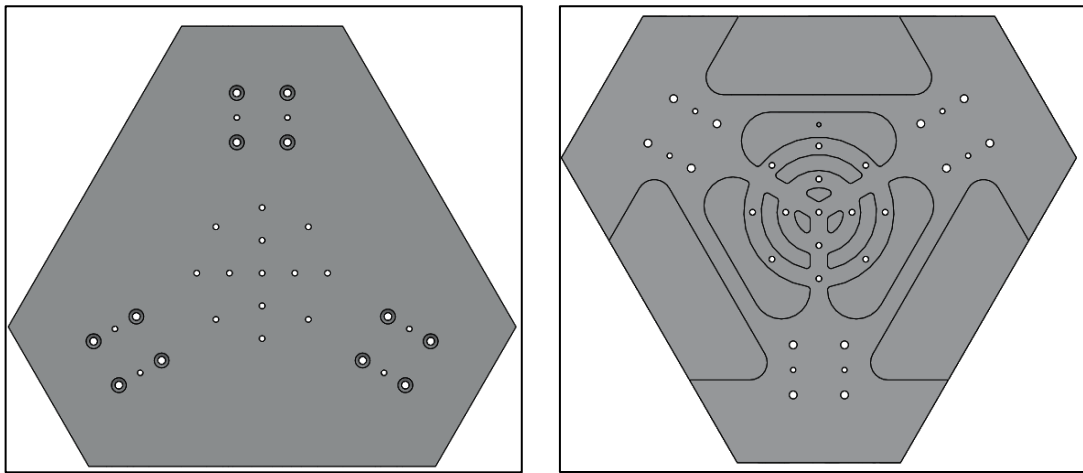


Figure 22: The current platform: a) Top view; b) Bottom view

The new geometry (Figure 23) has been created respecting the current structure as much as possible, also because a different shape would not grant enough space to host the standing subject's feet when performing vibration measurements. Anyway, no more mechanical devices will be fixed on the new platform, thus entailing the removal of the central pattern of holes. Moreover, no patterns of ribs are provided, because the use of an alternative material already provides for a structural lightening. Then, in order to definitely eliminate the wedges, a different arrangement of holes for bolts and centering pins has been designed on the short sides, so to fix the platform directly on the cubes through proper composite-designed fasteners. This fact involved a slight enlargement of the platform but allowed to save on 4 kg of redundant masses. Finally, for aesthetic and safety reasons, the six corners have been rounded.

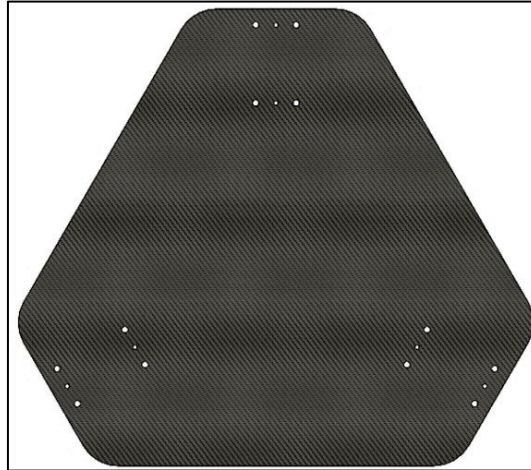


Figure 23: The new platform (top view)

### 3.3 Material choice

The aluminum full section resulted too heavy and, in order to lighten it, a research on possible alternative materials has been carried out. For the sake of not undermining the stiffness, a sandwich panel made up of an aluminum honeycomb layer, covered by two carbon fiber skins, has been chosen.

In fact, the honeycomb pattern provides the same (even better) stiffness of a full section item made of the same material, but its strongly reduced density allows saving on much redundant mass. Many materials are available to create a honeycomb structure, namely the aramidic *NOMEX*®, the glass fiber, the *KEVLAR*® and the aluminum. The first three ones, however, involve high purchasing costs, but poor structural properties for the required purposes. Hence, a 5052 aluminum honeycomb has been chosen and, among the available products, the denser one (3.175 mm of cell size) provided the best mechanical features, although accounting for a little higher mass [59]. The material properties are then shown in Table 16:

Aluminum honeycomb I.MA.TEC 1/8 – 5052 - .003									
$\rho$	$E_1$	$E_2$	$E_3$	$\nu_{12}$	$\nu_{13}$	$\nu_{23}$	$G_{12}$	$G_{13}$	$G_{23}$
[ton/mm <sup>3</sup> ]	[GPa]						[GPa]		
1.92E-10	-	-	6.205	0.33	-	-	-	1.448	0.538

Table 16: Elastic properties of aluminum honeycomb [59]

As shown in Table 16, the honeycomb has a very low relative density (only  $0.192 \text{ ton/mm}^3$  with respect to  $2.81 \text{ ton/mm}^3$  of the full section), because the material concentrates only on the hexagons profiles, leaving voids among them. However, it has very poor elastic modulus in vertical direction, which calls for the employment of two carbon fiber woven skins (properties in Table 17), that provide a great contribution in stiffness. It is worth to underline that no great differences exist between the *High Strength* (HS) and the *High Modulus* (HM) carbon fibers but, in terms of stiffness, it arises that HM could provide higher contribution with respect to the others [60] [61].

<b>High Modulus Carbon fiber DELTA-TECH</b>									
$\rho$	$E_1$	$E_2$	$E_3$	$\nu_{12}$	$\nu_{13}$	$\nu_{23}$	$G_{12}$	$G_{13}$	$G_{23}$
[ $\text{ton/mm}^3$ ]	[GPa]						[GPa]		
1.4E-09	390	6	6	0.35	0.35	0.35	20	20	-

Table 17: Elastic properties of HM carbon fiber [60] [61]

### 3.4 FEM model definition

In order to correctly represent the new platform in *ABAQUS*®, the sandwich structure has been modeled by means of three superimposed layers of solid elements: two carbon fiber skins that enclose a central aluminum structure. Given the strong anisotropy of the materials, the elastic properties have been defined through the “Engineering Constants” command.

In particular, the central honeycomb has been modeled as a hexagonal prism with full section, to which the properties of Table 16 have been assigned. Instead, the properties of Table 17 have been referred to a single carbon fiber, which needed to be woven to other fibers in order to recreate a composite sheet. The procedure to model a similar structure is then described in the next paragraph.

#### 3.4.1 Skins and orientation

The two skins are made up by stacks of woven carbon fiber layers, which called for the creation of a “Composite Layup” in the “Property” table of *ABAQUS*®. This feature allows to define the composite stack by means of subsequent plies, that can be intended as the representation of the single, oriented fibers. Anyway, a geometrical model of the plate needs

to be provided, along with its thickness, so that layup can be added as a material property to the structure. For these reasons, the ply thickness, intended as the fiber diameter, needs to be fixed and, according to [60], it would be reasonable to assume a value of 0.15 mm. Then, each couple of plies represent a layer, so each layer would be 0.3 mm thick. Finally, once chosen the number of desired layers, the total skin thickness could be obtained by multiplying this number times the thickness of each layer. However, the thickness is defined as a unity by the *ABAQUS*® “Composite Layup Manager”, so each ply would be expressed as a percentage of the total thickness.

Furthermore, in order to give the right orientation to the fibers, the geometrical model has been given a local reference system, placed in the middle of the body, with indices 1, 2 and 3 (Figure 24). In particular, 1 and 2 refer to the in-plane directions, while the 3 corresponds to the out-of-plane normal axis, pointing out the stacking direction.

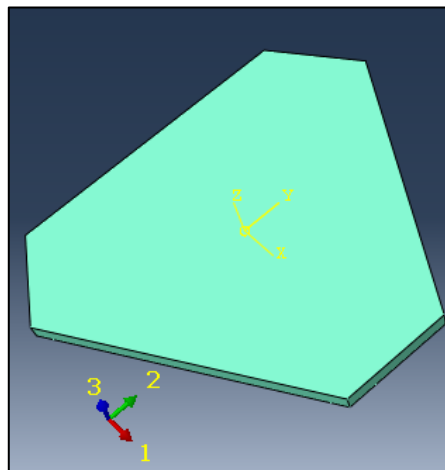


Figure 24: ABAQUS® - Local reference system of a skin

Depending on the orientation angle of each ply with respect to the direction 1, two woven patterns have been defined, both showing the perpendicularity of the warp and the weft of each layer, made up by two subsequent plies. However, changes can occur in the relative orientation between the single layers, as shown in Figure 25, where two different arrangements are shown. In particular, the pattern A (Table 18) provides a  $90^\circ$  shift between two layers, it results easier to manage and it is suitable for an even number of layers; instead, the pattern B (Table 19) involves a  $30^\circ$  shift between three layers, making it proper for stacks composed by multiples of three layers. Of course, each pattern represents the basic structure of the stack, and it can be repeated more times, so as to build up thicker plates.

		Ply Name	Region	Material	Element Relative Thickness	CSYS	Rotation Angle	Integration Points
1	✓	Fibra_0_layer1	(Picked)	Fibra_di_carbonio	0.25	<Layup>	0	1
2	✓	Fibra_90_layer1	(Picked)	Fibra_di_carbonio	0.25	<Layup>	90	1
3	✓	Fibra_45_layer2	(Picked)	Fibra_di_carbonio	0.25	<Layup>	45	1
4	✓	Fibra_135_layer2	(Picked)	Fibra_di_carbonio	0.25	<Layup>	135	1

Table 18: Pattern A for composite layup

		Ply Name	Region	Material	Element Relative Thickness	CSYS	Rotation Angle	Integration Points
1	✓	Fibra_0_layer1	(Picked)	Fibra_di_carbonio	0.16667	<Layup>	0	1
2	✓	Fibra_90_layer1	(Picked)	Fibra_di_carbonio	0.16667	<Layup>	90	1
3	✓	Fibra_30_layer2	(Picked)	Fibra_di_carbonio	0.16667	<Layup>	30	1
4	✓	Fibra_120_layer2	(Picked)	Fibra_di_carbonio	0.16667	<Layup>	120	1
5	✓	Fibra_60_layer3	(Picked)	Fibra_di_carbonio	0.16667	<Layup>	60	1
6	✓	Fibra_150_layer3	(Picked)	Fibra_di_carbonio	0.16667	<Layup>	150	1

Table 19: Pattern B for composite layup

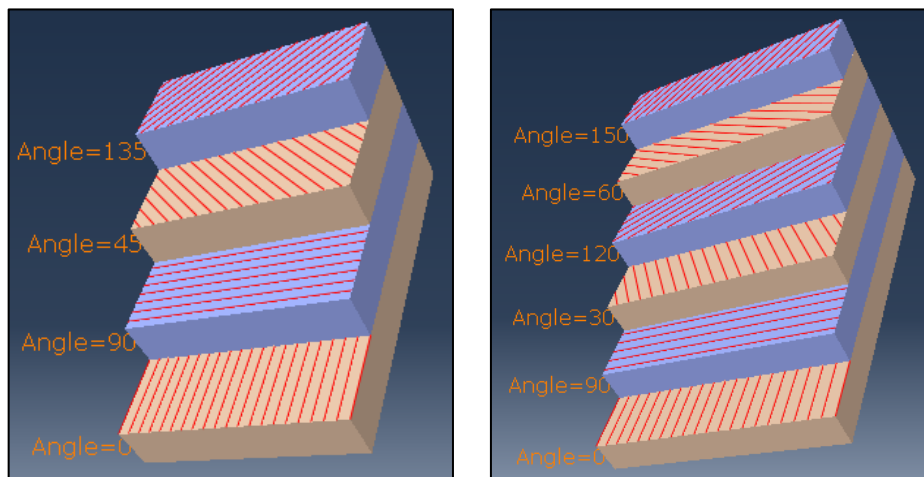


Figure 25: ABAQUS® - Composite layup: a) Pattern A; b) Pattern B

### 3.4.2 Assembly

Once defined the material properties of the three layers, the final assembly needs to be created. In particular, the two skins will be attached to the upper and lower surfaces of the central aluminum honeycomb, thus obtaining the sandwich-panel structure. Hence, the final assembly is provided in Figure 26, where the skins are represented by dark grey layers, while the honeycomb appears as the light grey one.

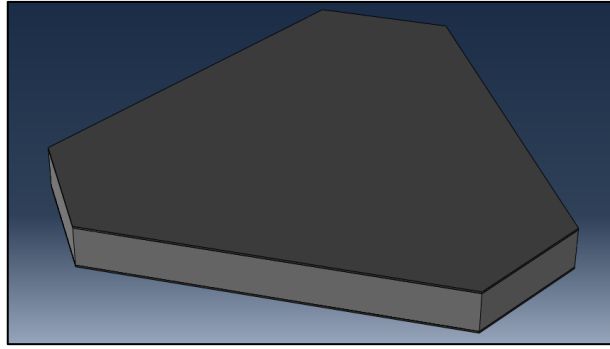


Figure 26: ABAQUS® - Sandwich panel model

### 3.4.3 Constraints and mesh

Once defined the geometrical features and the assembly, a proper constraint setting is required. In fact, the two skins and the honeycomb core need to stack over themselves to form a single platform, subsequently connected to the aluminum cubes. In order to do so, two kind of constraints have been applied to the assembly, exploiting the definition of master (red) and slave (violet) surfaces:

- Face-to-face position constraint
- Tie constraint

The first one is a positional constraint, useful for maintaining the alignment of two or more surfaces from the beginning to the end of the simulation. This has been applied to the three external surfaces of the cubes and to the short sides of the platform layers, as shown in Figure 27, choosing the upper skin lateral surface as the fixed instance (master):

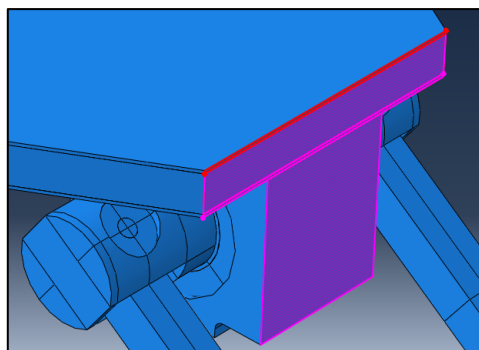


Figure 27: ABAQUS® - Face-to-face positional constraint

The second one, instead, forces the connected nodes of the involved surfaces to move simultaneously. Here too, the master and slave surfaces need to be defined: usually, the

master is the coarser surface, often referring to the bigger objects, while the slave mesh is the finer one and its nodes are forced to follow the master surface motion. Thus, according to the mesh dimension and to the involved instances, the following couplings have been adopted (Table 20) and they show up as proposed in Figure 28.

Master surface (red)			Slave surface (violet)		
Instance	Top/Bottom	Mesh size	Instance	Top/Bottom	Mesh size
Lower Skin	Bottom	6 mm	Cubes	Top	5 mm
Lower Skin	Top	6 mm	Honeycomb	Bottom	5 mm
Upper Skin	Bottom	6 mm	Honeycomb	Top	5 mm

Table 20: Relative tie constraints of composite layup

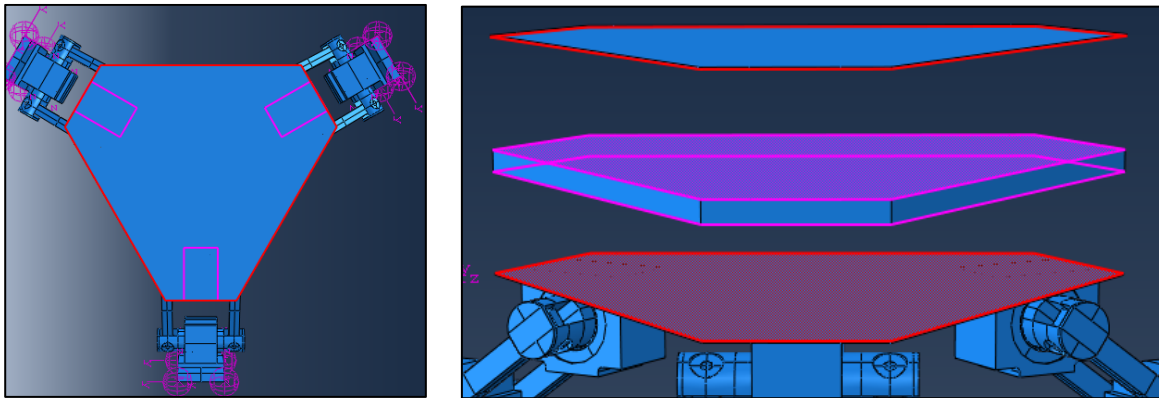


Figure 28: ABAQUS® - Tie constraint

So, the FEM model of the new platform is now completely defined. In the next paragraph, a series of simulations will be performed, with the aim of optimizing the custom parameters of the structure.

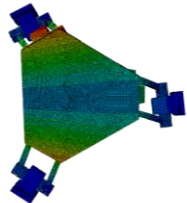
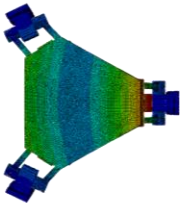
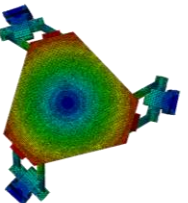
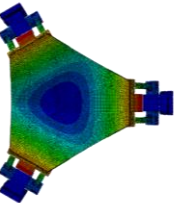
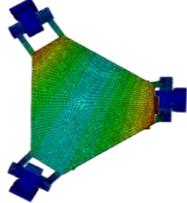
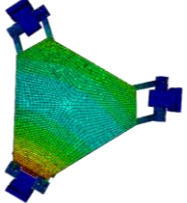
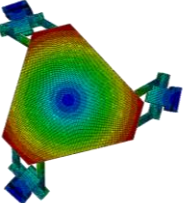
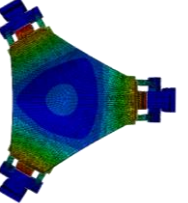
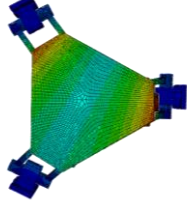
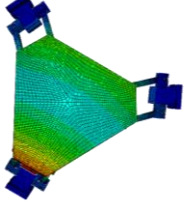
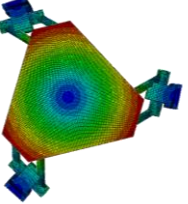
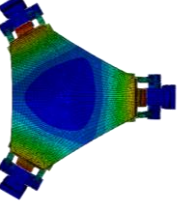
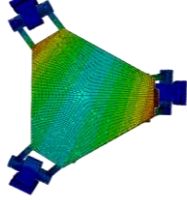
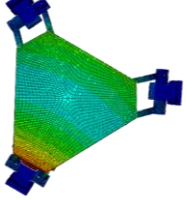
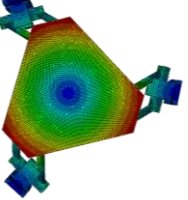
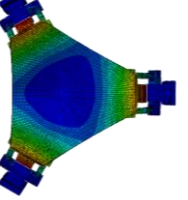
### 3.5 Optimal parameter definition through FEM modal analysis

Both the number of woven layers for the two skins and the aluminum honeycomb thickness can be considered as user-defined parameters, to be optimized in order to get the best bandwidth enhancement of the suspended mass system. Hence, the shaker modal behavior needs to be examined alternatively changing only one of the two parameters, while leaving the other fixed, thus verifying if an optimal combination of the two variables exists.



### 3.5.1 Number and pattern of skin layers

The effect of the number and pattern of the skin layers has been simulated, using a fixed thickness of 25 mm for the three-layered structure. This means that, for each added layer on the two skins, the aluminum honeycomb would reduce its thickness of 0.6 mm. These analyses are aimed to assess the actual influence of the carbon fiber skins on the overall vibrational behavior of the structure, and to understand if the difference in patterning the fibers could be a relevant parameter to lean onto. The obtained results are shown in Table 21 where, in the left column, the number of layers and the adopted pattern are indicated and separated by a dash. Finally, the trend of the bandwidth is represented in Figure 29.

Vibration modes - Changes in number and pattern of skin layers				
# Layers - Pattern	MODE 1 (Hz)	MODE 2 (Hz)	MODE 3 (Hz)	MODE 4 (Hz)
Current	32.7 	32.7 	39.9 	124.0 
2-A	34.7 	35.2 	51.9 	162.7 
3-A	35.6 	38.3 	51.9 	186.1 
3-B	36.8 	37.4 	51.9 	186.7 

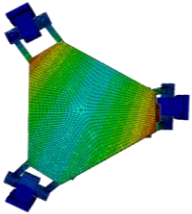
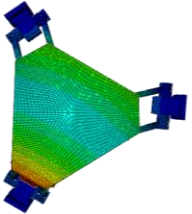
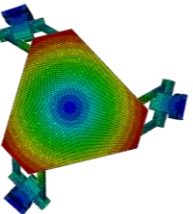
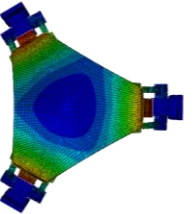
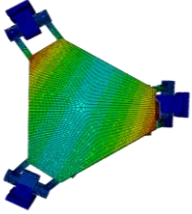
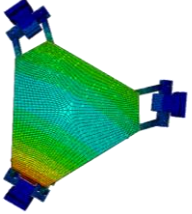
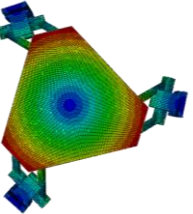
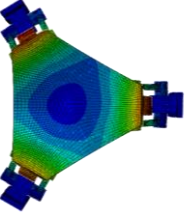
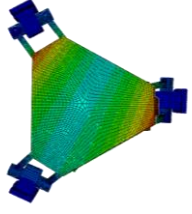
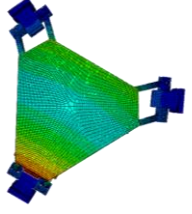
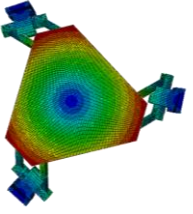
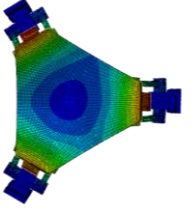
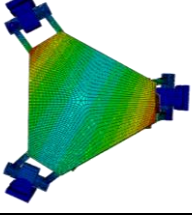
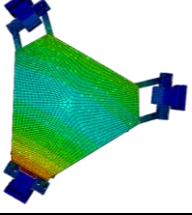
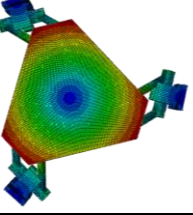
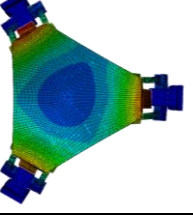
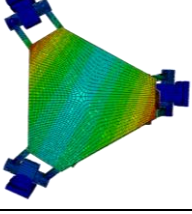
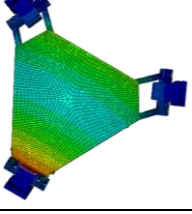
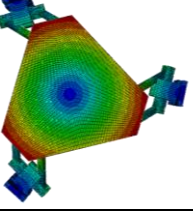
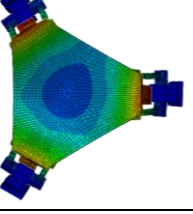
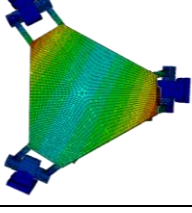
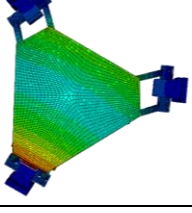
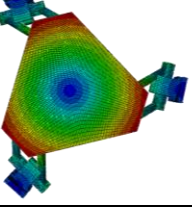
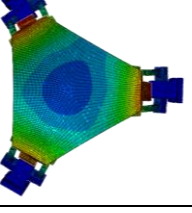
4-A	38.0 	38.7 	51.9 	204.0 
6-A	39.4 	40.2 	51.6 	227.2 
6-B	39.4 	40.2 	51.6 	227.2 
8-A	40.1 	40.9 	51.3 	241.9 
9-A	40.1 	41.3 	51.1 	247.22 
9-B	40.2 	41.1 	51.1 	247.37 

Table 21: Vibration modes - Changes in number and pattern of skin layers

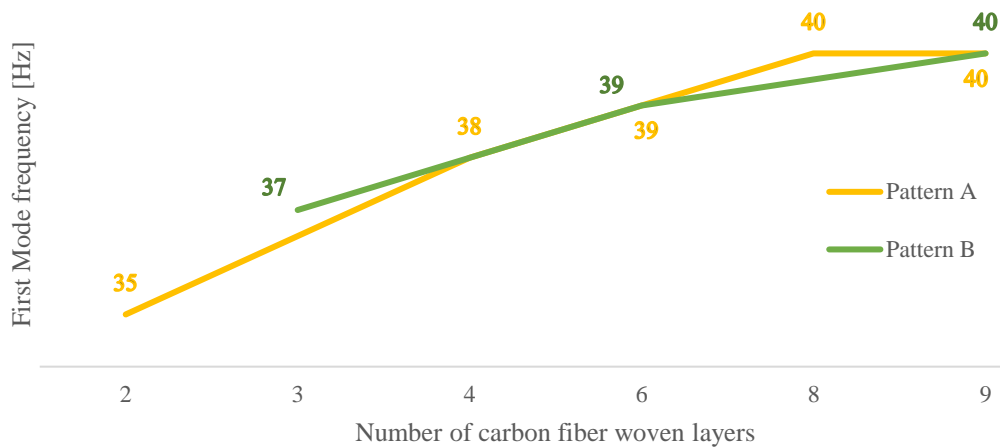
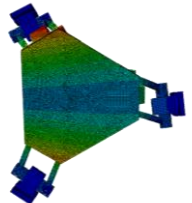
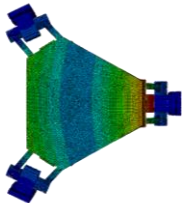
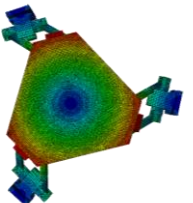
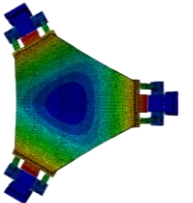
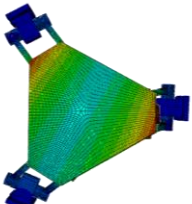
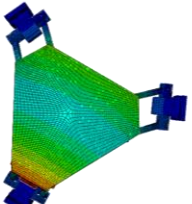
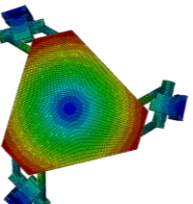
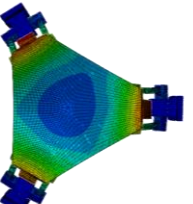
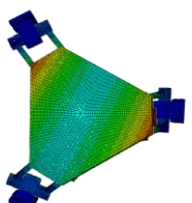
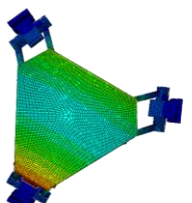
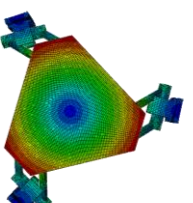
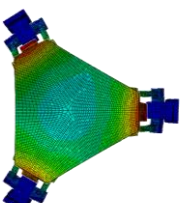
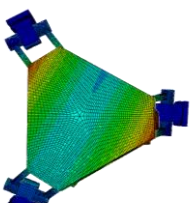
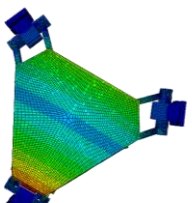
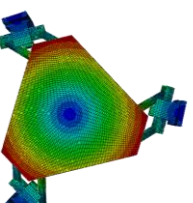
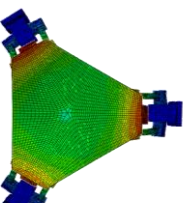
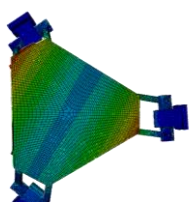
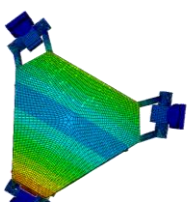
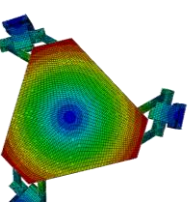
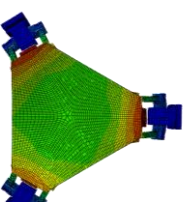
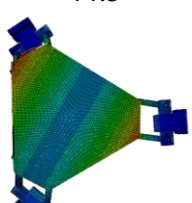
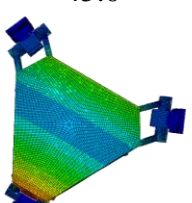
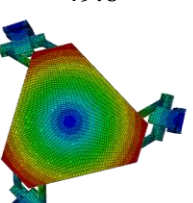
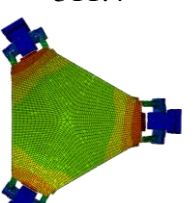


Figure 29: First Mode frequency vs Number of carbon fiber woven layers

As shown in Figure 29, the pattern B could be more effective only for a number of layers lower than six. In fact, for this value, the two patterns will become indifferent. Moreover, the trend reaches its maximum for eight layers, approaching the asymptotic value of 40 Hz of bandwidth. Hence, both the above-listed statements have been demonstrated by induction, simulating the employment of nine layers: in this case, almost no difference has been appreciated, neither between the two patterns nor between eight or nine layers. Therefore, eight layers are enough to achieve the best performances, while the choice of pattern A would ease the stacking procedure.

### 3.5.2 Thickness of the aluminum honeycomb layer

Once defined the optimal number of woven carbon fiber layers, the analysis moved to the evaluation of the optimal thickness of the central aluminum honeycomb. In fact, in opposition to the results of Table 7, a greater thickness could be effective for a bandwidth enlargement. Thus, another series of FEM simulations has been carried out, fixing the properties of each skin to eight layers (thereby, 2.4 mm of thickness) with the fibers arranged in the pattern A. Additionally, in Table 22, the thickness refers to the total thickness of the three-layered structure, while the aluminum honeycomb thickness would result by subtracting 4.8 mm to the total specified thickness. Finally, the trend of the bandwidth is represented in Figure 30.

Vibration modes - Changes in total platform thickness				
Thickness	MODE 1 (Hz)	MODE 2 (Hz)	MODE 3 (Hz)	MODE 4 (Hz)
Current	32.7 	32.7 	39.9 	124.0 
25 mm	40.1 	40.9 	51.3 	241.9 
35 mm	42.7 	43.4 	51.0 	278.8 
45 mm	43.8 	44.4 	50.6 	297.6 
55 mm	44.3 	44.8 	50.1 	307.1 
65 mm	44.5 	45.0 	49.6 	311.4 

75 mm	44.6	45.0	49.2	312.8
85 mm	44.6	44.9	48.7	312.6

Table 22: Vibration modes - Changes in total platform thickness

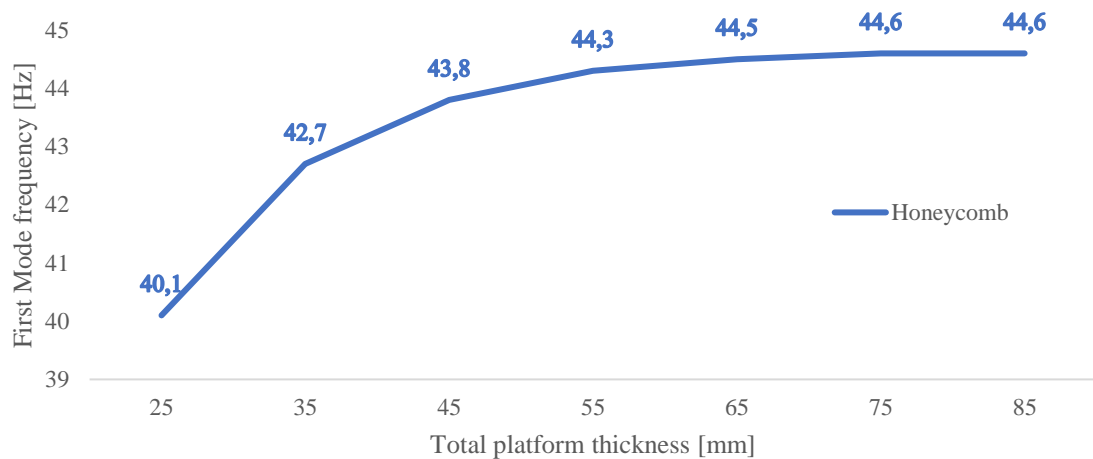


Figure 30: First Mode frequency vs Total platform thickness

As inferred from Figure 30, the bandwidth approaches the asymptotic value few points above 44 Hz, in correspondence of 55 mm of total platform thickness. In fact, increasing the honeycomb thickness of 10, 20 or 30 mm more, the improvement on bandwidth is almost null. Hence, for economic issues and in order to maintain the second and third modes far enough among them, avoiding mode inversion or coupling, the total thickness of 55 mm would be the most suitable. Therefore, the optimized platform would show eight layers for each skin, oriented according to the pattern A, and a honeycomb layer 50.2 mm thick, for a total platform thickness of 55 mm and a mass of 3.75 kg. Unfortunately, only 25 mm thick aluminum honeycomb was available in stock with the desired mechanical properties: thus, for cost reasons and because the target level of 40 Hz bandwidth had been reached in any case, the final platform (whose mechanical drawing is available in the Appendix A) has been purchased with a 25 mm of total thickness and a mass of 2.43 kg. The new platform allowed



---

for saving 14.26 kg of redundant mass (10.18 kg by changing the platform materials, 4.08 by suppressing the three wedges). Moreover, the previous modal analyses have been performed in the unloaded condition, but the presence of a person on the platform can affect its vibrational behavior, according to Subashi, Griffin and Matsumoto [34]. For these reasons, a further simulation has been performed, in order to demonstrate that the vibration modes of the body and the shaker are decoupled and do not mutually excite.

### 3.6 Effect of the apparent mass

Another interesting simulation to be performed on the new platform regards the apparent mass effects. In fact, as already mentioned in the introduction, the vibrational behavior of a structure and of a body standing on it may mutually affect, resulting in a particular resonance phenomenon, where the mass of the subject is perceived as it was 1.5-2 times greater than its static value. The actual, perceived value of mass is the apparent one, and an eventual oversight of its contribution could lead to dramatic undervaluation of the real loading conditions on the platform [36].

Hence, this simulation is aimed to assess if the platform dynamic behavior is affected or not by the human body which stands on it. The answer depends on the values of the first natural frequencies of the two entities: in fact, if they result distant in the spectrum, they cannot affect each other in a hypothetical combined mode of vibration, so they can be called as independent or decoupled. Instead, if their resonant frequencies are very close to each other, they can mutually excite, causing a dynamic overload on the structure around that frequency.

Matsumoto and Griffin, basing on the experimental campaigns carried out by Subashi et al. [34], proposed a model to schematize the human body as a mass/dashpot/spring system, whose mass-normalized values of inertia, damping and stiffness are shown in Table 23. These optimized model parameters are based on the mean-normalized apparent masses of twelve subjects in a standing posture [36]. Indeed, the mass normalization fits the model to any static mass standing on the shaker, allowing to get the actual parameters just by multiplying the tabled values times the actual static mass.

This time, the subject has been thought to have a mass of 100 kg which, in case of dynamic amplification at low frequencies, can reach an apparent mass value of almost 200 kg.

Stiffness [N/m·kg]		Damping [N·s/m·kg]		Mass [-]	
$k_1$	$k_2$	$c_1$	$c_2$	$m_1$	$m_2$
4390	553	37.1	11.8	0.574	0.394

Table 23: Mass-normalized parameters for Matsumoto and Griffin's model

Basing on the optimized platform obtained in the previous paragraph, the model has been developed in *ABAQUS*®. First, a point instance has been created in the existing assembly, and made it coincide with the centre of the upper surface of the platform by means of a positional constraint. Then, the motion of both the point instance and the platform have been bonded together through a tie constraint, while two other points in free space have been created by vertical projection from the platform centre. Then, the parameters of Table 23, multiplied times 100 kg, have been assigned using the “Special” tab. In particular, the two point masses have been attached to the two free points, by means of “Inertia” > “Point Mass/Inertia” > “Isotropic”, while the command “Spring/Dashpots” > “Connect two points” has been employed to set up the two couples of springs and dampers. The obtained model is shown in Figure 31, along with a schematic provided from the authors [36].

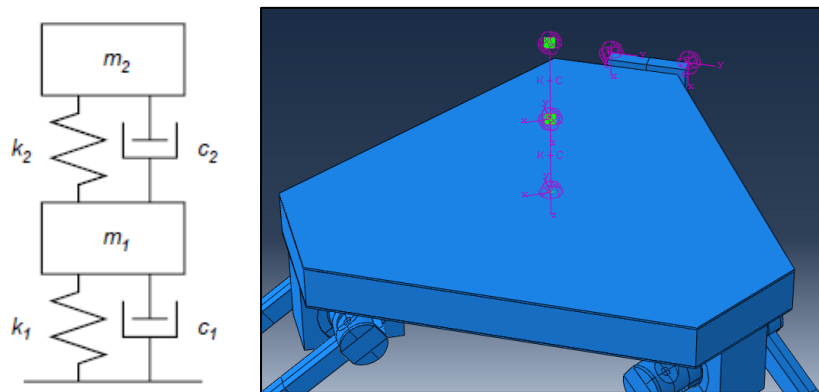


Figure 31: Matsumoto and Griffin: a) Human body scheme; b) FEM model of human body

The obtained first four modes are provided in Table 24. Comparing these results with the ones obtained for the 55 mm platform simulation (line 5 of the Table 22), it arises that the first two modes of the whole assembly are now the two synchronous and asynchronous modes of the standing subject (5.6 Hz and 14.8 Hz respectively), while pitch and roll of the platform remain fixed to 44.3 Hz and 44.8 Hz, although now representing the third and fourth mode of the entire structure. Thereby, the modes of the subject and the ones of the platform result well decoupled, confirming that no mutual excitation occurs between the two entities.



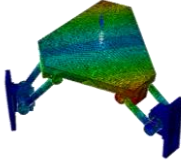
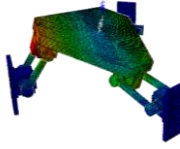
Vibration modes - Standing subject and platform			
MODE 1 (Hz)	MODE 2 (Hz)	MODE 3 (Hz)	MODE 4 (Hz)
5.6	14.8	44.3	44.8
			

Table 24: Vibration modes - Standing subject and platform

Once studied the dynamic behavior of the new platform, the last analysis to perform regards the study on its static resistance. Therefore, further simulations have been run and proposed in the next paragraph.

### 3.7 Static model

#### 3.7.1 Weight distributed on two footprints

In order to verify the structural behavior of the platform, a static analysis has been carried out, simulating the pressure that the human body weight exerted on the structure. A standard mass of 100 kg has been taken as a reference, but a multiplying coefficient of 2 has been employed, in order to consider any apparent mass effect that would overload the platform at low frequencies of excitation, as explained in the previous paragraph. So, the weight related to a mass  $m$  of 200 kg has been set up and distributed on two rectangles ( $b = 290 \text{ mm}$ ,  $h = 110 \text{ mm}$ ), representing the footprints of the subject standing on the platform. The following data have been employed for the simulation, as shown in Figure 32:

$$Area_{footprint} = bh = 290 \cdot 110 = 31900 \text{ mm}^2 \quad (3.1)$$

$$Weight = mg = 200 \cdot 9.81 = 1962 \text{ N} \quad (3.2)$$

$$Pressure_{footprint} = \frac{1}{2} \frac{Weight}{Area_{footprint}} = \frac{1}{2} \cdot \frac{1962}{31900} = 0.03 \text{ MPa} \quad (3.3)$$



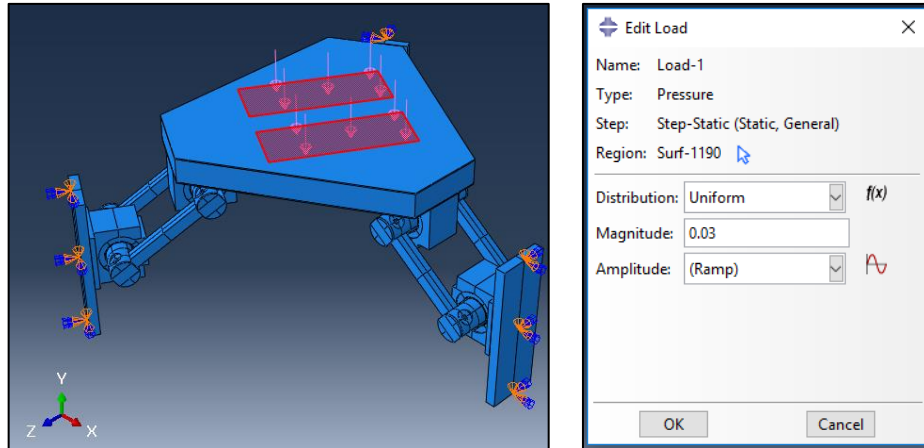


Figure 32: ABAQUS® - Load application on two footprints: a) Model; b) Commands

From the exposed loading conditions, both the values of maximum deflection and maximum principal stress have been derived (Figure 33, Figure 34 and Figure 35). Although resulting in values very close to the ones obtained by Von Mises' criterion, this kind of stress seemed to be more representative in describing the real behavior of the component. In fact, the platform is composed by fragile carbon skins and ductile aluminum honeycomb, but the most stressed point is expected to be at the interface between the lower skin and the cubes. So, being the lower skin a fragile material, the maximum principal stress has been preferred to the Von Mises' one.

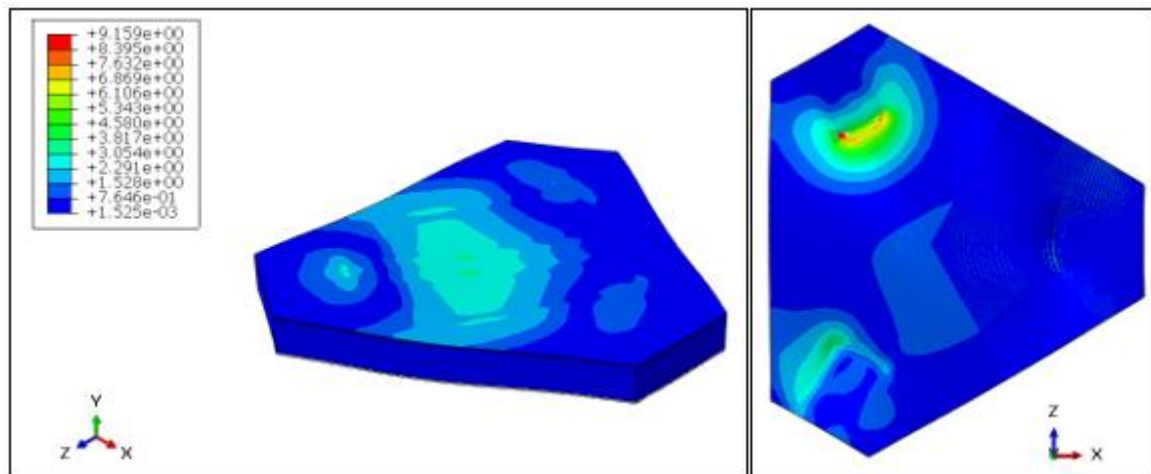


Figure 33: Static loading, two feet - Max principal stress: a) Global top view; b) Bottom view

As expected, the maximum principal stress of 9.16 MPa has been reached at the interface between platform and cubes, as shown in Figure 33b.

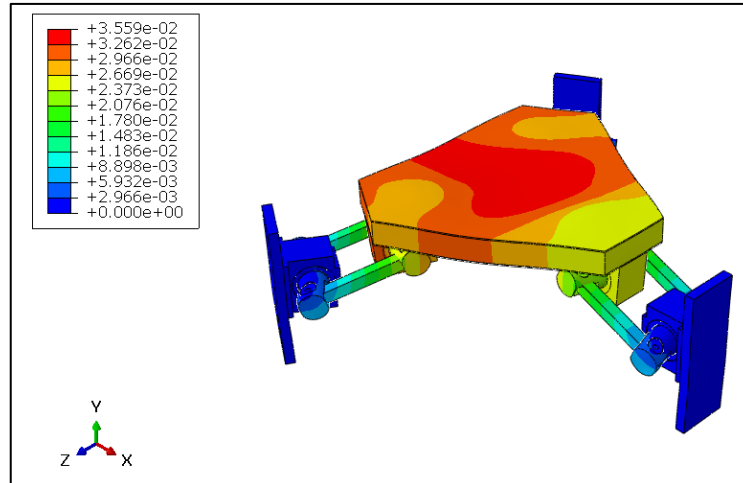


Figure 34: Static loading, two feet - Max deflection on the whole structure

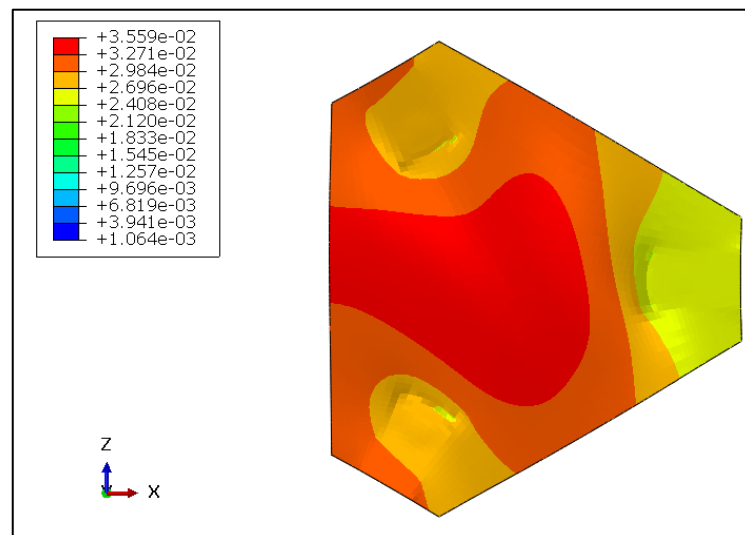


Figure 35: Static loading, two feet - Max deflection on the platform only (Bottom view)

From Figure 34 and Figure 35 arises that the highest deflection (0.036 mm) of the overall structure of lumped masses occurs, as expected, at the centre of the platform, in a node belonging to the honeycomb layer. From these data, no structural issue would occur in steady-state conditions.

### 3.7.2 Weight distributed on a single footprint

The previous analysis can be useful in a steady-state situation, but the maximum loading condition occurs in the moment when the subject jumps on the shaker. In this case, the platform needs to stand the whole weight of the person on the area of a single footprint, as inferred from the next simulations (Figure 36, Figure 37 and Figure 38).

Here, the pressure acting on the footprint doubles, reaching the value of 0.06 MPa.

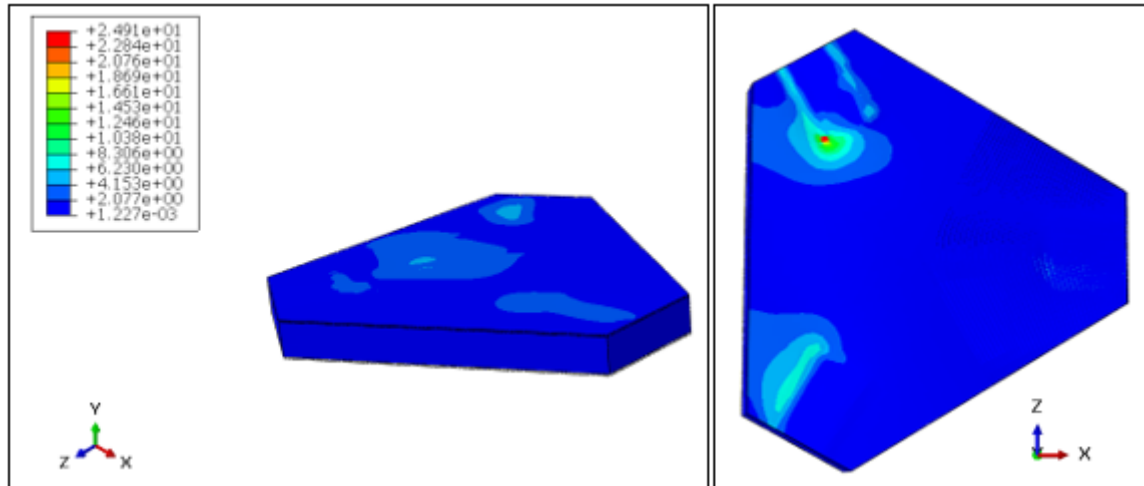


Figure 36: Static loading, one foot - Max principal stress: a) Global top view; b) Bottom view

Again, as shown in Figure 36, the maximum principal stress has been reached at the interface between platform and cubes, but its value of 24.91 MPa is much higher than before. However, for what concerns the deflection, the asymmetry of the applied weight causes an unbalance of the platform, which behaves as it was in roll/pitch conditions. In this case, the maximum deflection of the overall structure reaches 0.982 mm on the cube which opposes the load, which forces it to move upwards (Figure 37). The platform, instead, presents a minor deflection at the interface with the above-mentioned cube, corresponding to 0.911 mm (Figure 38).

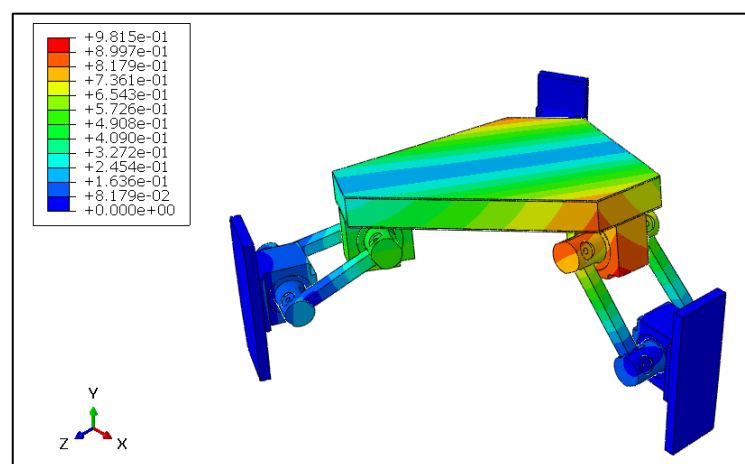


Figure 37: Static loading, one foot - Max deflection on the whole structure

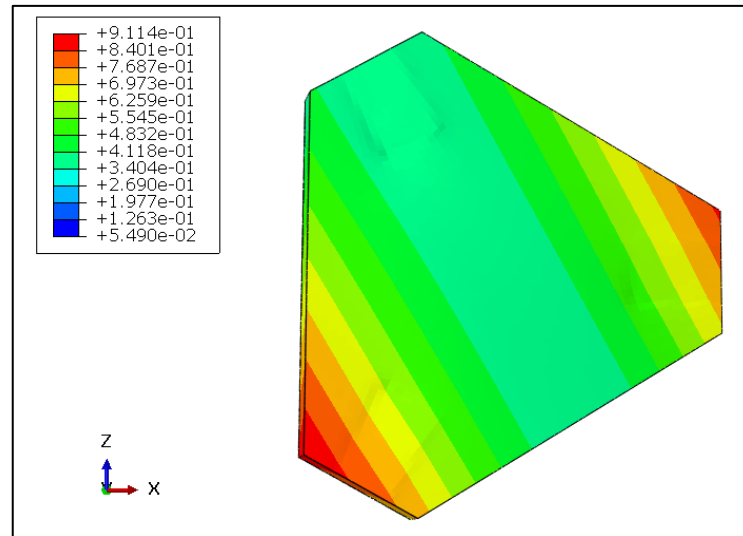


Figure 38: Static loading, one foot - Max deflection on the platform only (Bottom view)

Therefore, also in the most demanding case of one-foot loading, it has been demonstrated that the stress levels of the platform lie well below the yield limit of the layers, concentrating on the interfaces between cubes and lower skin. For what concerns the maximum deflection, instead, its order of magnitude results well below the warning zone in all the situations. Hence, this last analysis closes the design phase, confirming that neither excessive displacements nor overstresses would be encountered.

Thus, the present work will move from the structural optimization of the shaker to the implementation of an integrated force sensing system. As a starting point, a static equilibrium of the forces will be performed, in order to obtain the relationship between applied and measured loads.

## Chapter 4

# Static equilibrium of forces and instability

### 4.1 Introduction and previous works

In the previous chapters, the lightweight design principles and the composite materials have been employed to improve the dynamic behavior of the multiaxial shaker, in terms of bandwidth enlargement. In this section, instead, the initial steps for designing a force platform have been undertaken. In fact, measuring the force applied from a standing human body subjected to multiaxial vibrations, configures as a crucial step for deriving the three-dimensional human body apparent mass, as demonstrated in [34], [35] and [36]. Thus, safety of use and high accuracy are required, without compromising the lightweight design of the structure.

The present work is intended to analytically model the shaker structure, then to evaluate the generic wrench (three forces and three moments) acting at the platform centre, starting from the loads measured in different points of the shaker. Unfortunately, very few sources on this specific argument are available in literature, but Dwarakanath et al. [56] and Ruiz' [62] studies on the chance to convert a Stewart's platform in a force-sensing structure, can be assumed as a guiding reference. In detail, Dwarakanath et al. stated that a force equilibrium among an externally applied wrench and the axial reaction forces of six links exists, but only if the links are stiff enough. In other words, the stiffness value needs to be much higher than inertial and damping coefficients, in order to make the acceleration and speeds negligible with respect to the displacements. Instead, Ruiz developed a six-axis load cell for ergonomic purposes, whose design involved the transportation of forces from the links to the centre of a moving platform, bearing in mind the assumptions about the stiffness of the linkages. Basing on these two sources, the present work aims to transport the loads among different locations of the structure, using local reference systems placed on the various components. Finally, the relationships among the different frames have been derived and resumed in a transformation matrix, relating measured and actually applied loads.

## 4.2 Transportation of the forces acting on the structure

The aim of the analytical model is to describe the static behavior of the platform centre, that continuously changes in function of the direct kinematics of the links. In fact, knowing the instantaneous position of the platform centre, expressed through the vector  $\mathbf{p} = [x_P \ y_P \ z_P]$ , it is possible to determine the vector  $\mathbf{q}_i$  containing the heights reached in the  $z$ -direction by each slider ( $i = 1, 2, 3$ ), that moves along its column [14]. Then, it is worth to remind that the positions of the links are fully described by two main angles,  $\theta_i$  (on the  $xy$  plane, Figure 39a) and  $\beta_i$  (on the  $xz$  plane, Figure 39b) depending on the vector  $\mathbf{p}$ , on the length of the links  $l$  [mm], on the platform radius  $R_P$  [mm], on the distance between the basement centre and the sliders  $s$  [mm] and on the  $\gamma$  angle that describes the mutual orientation of the three sliders in the  $xy$  plane:

$$\theta_i = \sin^{-1} \frac{x_P \sin \gamma_i + y_P \cos \gamma_i}{l} \quad (4.1)$$

$$\beta_i = \cos^{-1} \frac{s - R_P}{l \cos \theta_i} \quad (4.2)$$

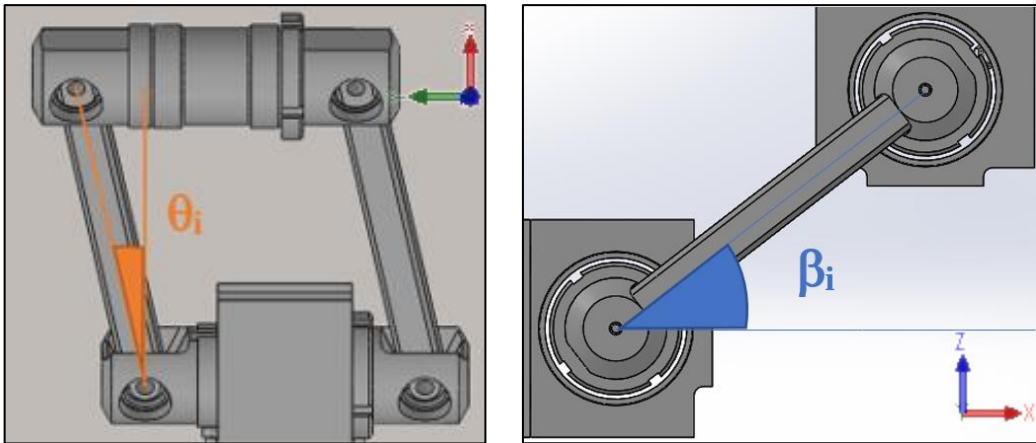


Figure 39: Link angles: a)  $\theta$  on the  $xy$  plane; b)  $\beta$  on the  $xz$  plane

As shown in the previous chapters, the links are mainly standing axial stresses, and eventually a torsional moment can appear, but only in case of an improper use of the shaker. For the sake of simplicity, then, that moment has been neglected, and a column vector  $\mathbf{N}$  containing the normal force components of the six links has been built up in the following way [62]:

$$\mathbf{N}^T = [\mathbf{N}_{ij}] = [\mathbf{N}_{11} \mathbf{N}_{12} \mathbf{N}_{21} \mathbf{N}_{22} \mathbf{N}_{31} \mathbf{N}_{32}] \quad (4.3)$$

where  $i = 1, 2, 3$  points out the slider (or cube) that supports each couple of links, while  $j = 1, 2$  points out one link of the  $i$ -th couple.

Moreover, each link has been assigned with its own reference system  $\{x_L y_L z_L\}_{ij}$ , as shown in Figure 40a, which needed to be rotated according to  $\theta_i$  and  $\beta_i$ , in order to be joined to the  $i$ -th cube. For these reasons, two new frames  $\{x_B y_B z_B\}_{ij}$ , corresponding to the centre of the bearings (Figure 40b) have been introduced, thanks to a rotation matrix  $\mathbf{J}_{\text{couple\_of\_bearings\_}i}$ , whose columns refer to the two bearings mounted on the  $i$ -th cube:

$$\mathbf{J}_{\text{couple\_of\_bearings\_}i} = \begin{bmatrix} \cos \theta_i \cos \beta_i & \cos \theta_i \cos \beta_i \\ \sin \theta_i & \sin \theta_i \\ \cos \theta_i \sin \beta_i & \cos \theta_i \sin \beta_i \end{bmatrix} \quad (4.4)$$

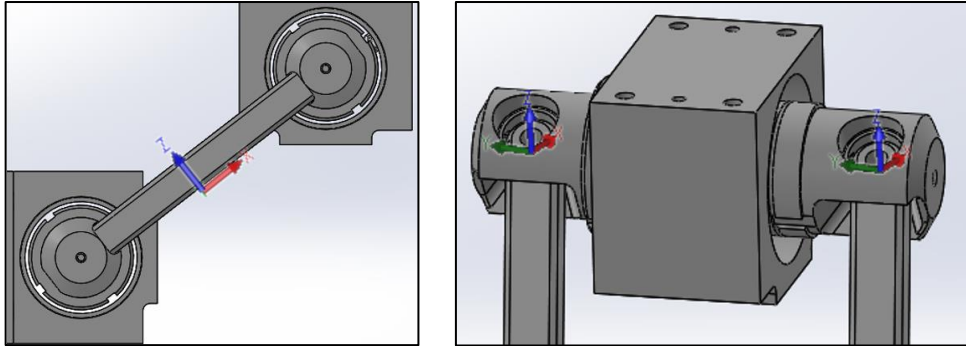


Figure 40: Reference frames - a) Link centre:  $\{x_L y_L z_L\}$ ; b) Bearings centre:  $\{x_B y_B z_B\}$

Moreover, in order to pass from the two  $\{x_B y_B z_B\}_{ij}$  frames to a single  $\{x_C y_C z_C\}_i$  frame located in the centre of each cube, the introduction of the transportation moments became necessary, taking place in three additional rows of the matrix  $\mathbf{J}_{\text{couple\_of\_bearings\_}i}$ . Therefore, the newly created  $6 \times 2$   $\mathbf{J}_{\text{cube\_}i}$  matrix appears as follows:

$$\mathbf{J}_{\text{cube\_}i} = \begin{bmatrix} \cos \theta_i \cos \beta_i & \cos \theta_i \cos \beta_i \\ \sin \theta_i & \sin \theta_i \\ \cos \theta_i \sin \beta_i & \cos \theta_i \sin \beta_i \\ -c \cos \theta_i \sin \beta_i & c \cos \theta_i \sin \beta_i \\ 0 & 0 \\ c \cos \theta_i \cos \beta_i & -c \cos \theta_i \cos \beta_i \end{bmatrix} \quad (4.5)$$

In this matrix, the value  $c$  [mm] has been introduced. In fact, as shown in Figure 41, both the centres of the bearings are equally distant from the centre of the cube on which they are mounted, and this distance corresponds to  $c$ .

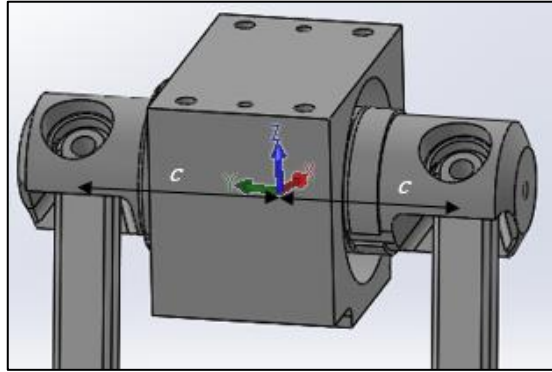


Figure 41: Reference frames - Cube centre:  $\{x_c y_c z_c\}$

Once the matrices  $\mathbf{J}_{cube_i}$  resulted available for each one of the three cubes, they have been put as diagonal elements of a newly created 18x6 matrix,  $\mathbf{J}_{cube}$ , that allowed to express the initial  $\mathbf{N}$  vector of axial forces in the new frame located in the centres of the three cubes, thus obtaining the array  $\mathbf{F}_{cubes}$ :

$$\mathbf{F}_{cubes} = \begin{bmatrix} [\mathbf{J}_{cube_1}] & [0] & [0] \\ [0] & [\mathbf{J}_{cube_2}] & [0] \\ [0] & [0] & [\mathbf{J}_{cube_3}] \end{bmatrix} \cdot \mathbf{N} = \mathbf{J}_{cube} \cdot \mathbf{N} \quad (4.6)$$

Of course,  $\mathbf{F}_{cubes}$  contains three forces and three moments for each one of the three cubes, respectively read in this 18x1 array of elements.

After that, the three reference systems  $\{x_c y_c z_c\}_i$  will be repeatedly translated in the  $z$ -direction, in order to move up to the top of the platform. Moreover, the possibility of installing a tension/compression load cell between the bottom of the platform and the top of the cubes has been taken into account, thus calling for an additional transportation matrix. Of course, if this would not be mounted, no further transportation moments would be created, thus this matrix would convert in a neutral identity matrix, not affecting the calculations. Therefore, as shown in Figure 42, the three new frames will move, respectively:



- From the centre of the cubes to the top surface of the cubes
- From the top surface of the cubes to the bottom surface of the platform (load cell)
- From the bottom surface of the platform to the top surface of the platform

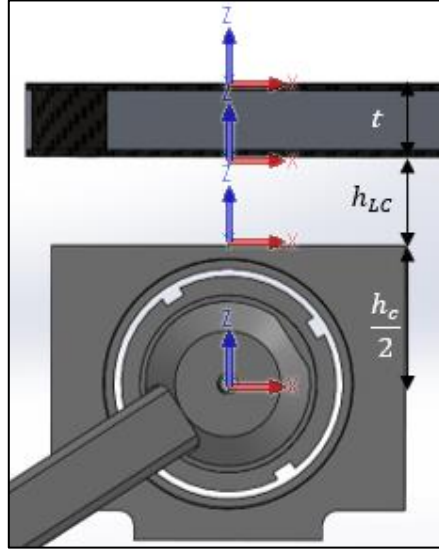


Figure 42: Reference frames - Translations:  $\{X_{BLC} Y_{BLC} Z_{BLC}\}$ ,  $\{X_{TLC} Y_{TLC} Z_{TLC}\}$ ,  $\{X_S Y_S Z_S\}$

Namely, the first translation would occur from  $\{X_C Y_C Z_C\}_i$  to  $\{X_{BLC} Y_{BLC} Z_{BLC}\}_i$ , knowing that the transportation moment acts on an arm equal to half the height of the cubes,  $\frac{h_c}{2}$  [mm]. The matrix  $\mathbf{J}_{bottom\_load\_cell\_i}$  allowed this transformation for each cube:

$$\mathbf{J}_{bottom\_load\_cell\_i} = \begin{bmatrix} 1 & 0 & 0 & 0 & 0 & 0 \\ 0 & 1 & 0 & 0 & 0 & 0 \\ 0 & 0 & 1 & 0 & 0 & 0 \\ 0 & \frac{h_c}{2} & 0 & 1 & 0 & 0 \\ -\frac{h_c}{2} & 0 & 0 & 0 & 1 & 0 \\ 0 & 0 & 0 & 0 & 0 & 1 \end{bmatrix} \quad (4.7)$$

Then, the matrices  $\mathbf{J}_{bottom\_load\_cell\_i}$  have been put as diagonal elements of a newly created 18x18 matrix,  $\mathbf{J}_{bottom\_load\_cell}$ , that allowed to express the previously obtained vector  $\mathbf{F}_{cubes}$  into the 18x1 vector  $\mathbf{F}_{bottom\_load\_cell}$ , containing all the forces and moments acting at the interface between the cubes and the hypothetical load cell:

$$\begin{aligned}
& \mathbf{F}_{bottom\_load\_cell} = \\
& = \begin{bmatrix} [\mathbf{J}_{bottom\_load\_cell\_1}] & [0] & [0] \\ [0] & [\mathbf{J}_{bottom\_load\_cell\_2}] & [0] \\ [0] & [0] & [\mathbf{J}_{bottom\_load\_cell\_3}] \end{bmatrix} \cdot \mathbf{F}_{cubes} = \quad (4.8) \\
& = \mathbf{J}_{bottom\_load\_cell} \cdot \mathbf{F}_{cubes}
\end{aligned}$$

The second translation would occur from  $\{x_{BLC} y_{BLC} z_{BLC}\}_i$  to  $\{x_{TLC} y_{TLC} z_{TLC}\}_i$ , knowing that the transportation moment acts on an arm equal to the height of a hypothetical load cell,  $h_{LC}$  [mm]. The matrix  $\mathbf{J}_{top\_load\_cell\_i}$  allowed this transformation for each hypothetical load cell:

$$\mathbf{J}_{top\_load\_cell\_i} = \begin{bmatrix} 1 & 0 & 0 & 0 & 0 & 0 \\ 0 & 1 & 0 & 0 & 0 & 0 \\ 0 & 0 & 1 & 0 & 0 & 0 \\ 0 & h_{LC} & 0 & 1 & 0 & 0 \\ -h_{LC} & 0 & 0 & 0 & 1 & 0 \\ 0 & 0 & 0 & 0 & 0 & 1 \end{bmatrix} \quad (4.9)$$

Then, the matrices  $\mathbf{J}_{top\_load\_cell\_i}$  have been put as diagonal elements of a newly created 18x18 matrix,  $\mathbf{J}_{top\_load\_cell}$ , that allowed to express the previously obtained vector  $\mathbf{F}_{bottom\_load\_cell}$  into the 18x1 vector  $\mathbf{F}_{top\_load\_cell}$ , containing all the forces and moments acting at the interface between the hypothetical load cell and the platform:

$$\begin{aligned}
& \mathbf{F}_{top\_load\_cell} = \\
& = \begin{bmatrix} [\mathbf{J}_{top\_load\_cell\_1}] & [0] & [0] \\ [0] & [\mathbf{J}_{top\_load\_cell\_2}] & [0] \\ [0] & [0] & [\mathbf{J}_{top\_load\_cell\_3}] \end{bmatrix} \cdot \mathbf{F}_{bottom\_load\_cell} = \quad (4.10) \\
& = \mathbf{J}_{top\_load\_cell} \cdot \mathbf{F}_{bottom\_load\_cell}
\end{aligned}$$

The third translation would occur from  $\{x_{TLC} y_{TLC} z_{TLC}\}$  to  $\{x_S y_S z_S\}$ , knowing that the transportation moment acts on an arm equal to the thickness of the platform,  $t$  [mm].

The matrix  $\mathbf{J}_{surface\_i}$  allowed this transformation for each one of the three points of the platform, corresponding to the cubes positions:

$$\mathbf{J}_{surface\_i} = \begin{bmatrix} 1 & 0 & 0 & 0 & 0 & 0 \\ 0 & 1 & 0 & 0 & 0 & 0 \\ 0 & 0 & 1 & 0 & 0 & 0 \\ 0 & t & 0 & 1 & 0 & 0 \\ -t & 0 & 0 & 0 & 1 & 0 \\ 0 & 0 & 0 & 0 & 0 & 1 \end{bmatrix} \quad (4.11)$$

Then, the matrices  $\mathbf{J}_{surface\_i}$  have been put as diagonal elements of a newly created 18x18 matrix,  $\mathbf{J}_{surface}$ , that allowed to express the previously obtained vector  $\mathbf{F}_{top\_load\_cell}$  into the 18x1 vector  $\mathbf{F}_{surface}$ , containing all the forces and moments acting in the three points found on the surface of the platform:

$$\begin{aligned} \mathbf{F}_{surface} &= \\ &= \begin{bmatrix} [\mathbf{J}_{surface\_1}] & [0] & [0] \\ [0] & [\mathbf{J}_{surface\_2}] & [0] \\ [0] & [0] & [\mathbf{J}_{surface\_3}] \end{bmatrix} \cdot \mathbf{F}_{top\_load\_cell} = \\ &= \mathbf{J}_{surface} \cdot \mathbf{F}_{top\_load\_cell} \end{aligned} \quad (4.12)$$

Finally, the last step to perform consisted in the transportation of the  $\mathbf{F}_{surface}$  components to the centre of the platform, identified in a new frame  $\{x_P y_P z_P\}$ . The previously obtained frames  $\{x_S y_S z_S\}_i$  have been respectively shifted for three values of the  $\gamma$  angles ( $0^\circ$ ,  $120^\circ$ ,  $240^\circ$ ), with respect to the  $\{x_P y_P z_P\}$  reference system, as shown in Figure 43:

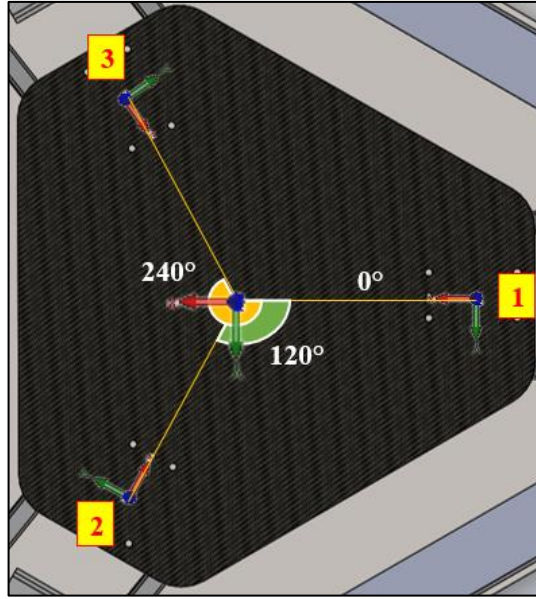


Figure 43: Reference frames - Central  $\{x_P y_P z_P\}$  and peripheral  $\{x_S y_S z_S\}$  frames on the platform

The presence of three peripheral frames implied the employment of three different transformation matrices, in order to get a new 18x1 vector that could express the same elements of  $\mathbf{F}_{surface}$  in coordinates of the new frame. Being  $R_P$  the distance between each of the three peripheral points and the centre of the platform, the expressions have been found as shown, in function of the three shifting angles  $\gamma$ :

$$\gamma = 0^\circ \quad \begin{bmatrix} F_{XC1} \\ F_{YC1} \\ F_{ZC1} \\ M_{XC1} \\ M_{YC1} \\ M_{ZC1} \end{bmatrix} = \begin{bmatrix} F_{X1} \\ F_{Y1} \\ F_{Z1} \\ M_{X1} \\ M_{Y1} + F_{Z1}R_P \\ M_{Z1} - F_{Y1}R_P \end{bmatrix} \quad (4.13)$$

$$\text{Finding out the transport matrix } \mathbf{J}_{to\_centre\_1} = \begin{bmatrix} 1 & 0 & 0 & 0 & 0 & 0 \\ 0 & 1 & 0 & 0 & 0 & 0 \\ 0 & 0 & 1 & 0 & 0 & 0 \\ 0 & 0 & 0 & 1 & 0 & 0 \\ 0 & 0 & R_P & 0 & 1 & 0 \\ 0 & -R_P & 0 & 0 & 0 & 1 \end{bmatrix} \quad (4.14)$$

$$\gamma = 120^\circ \quad \begin{bmatrix} F_{XC2} \\ F_{YC2} \\ F_{ZC2} \\ M_{XC2} \\ M_{YC2} \\ M_{ZC2} \end{bmatrix} = \begin{bmatrix} \frac{\sqrt{3}}{2}F_{Y2} - \frac{1}{2}F_{X2} \\ -\frac{\sqrt{3}}{2}F_{X2} - \frac{1}{2}F_{Y2} \\ F_{Z2} \\ -\frac{1}{2}M_{X2} + \frac{\sqrt{3}}{2}M_{Y2} + \frac{\sqrt{3}}{2}F_{Z2}R_P \\ -\frac{\sqrt{3}}{2}M_{X2} - \frac{1}{2}M_{Y2} - \frac{1}{2}F_{Z2}R_P \\ M_{Z2} - \frac{1}{2} \cdot \frac{\sqrt{3}}{2}F_{X2}R_P + \frac{1}{2} \cdot \frac{\sqrt{3}}{2}F_{X2}R_P - \frac{1}{2} \cdot \frac{1}{2}F_{Y2}R_P - \frac{\sqrt{3}}{2} \cdot \frac{\sqrt{3}}{2}F_{Y2}R_P \end{bmatrix} \quad (4.15)$$

$$\text{Finding out the transport matrix } \mathbf{J}_{to\_centre\_2} = \begin{bmatrix} -\frac{1}{2} & \frac{\sqrt{3}}{2} & 0 & 0 & 0 & 0 \\ -\frac{\sqrt{3}}{2} & -\frac{1}{2} & 0 & 0 & 0 & 0 \\ 0 & 0 & 1 & 0 & 0 & 0 \\ 0 & 0 & \frac{\sqrt{3}}{2}R_P & -\frac{1}{2} & \frac{\sqrt{3}}{2} & 0 \\ 0 & 0 & -\frac{1}{2}R_P & -\frac{\sqrt{3}}{2} & -\frac{1}{2} & 0 \\ 0 & -R_P & 0 & 0 & 0 & 1 \end{bmatrix} \quad (4.16)$$

$$\gamma = 240^\circ \quad \begin{bmatrix} F_{XC3} \\ F_{YC3} \\ F_{ZC3} \\ M_{XC3} \\ M_{YC3} \\ M_{ZC3} \end{bmatrix} = \begin{bmatrix} -\frac{\sqrt{3}}{2}F_{Y3} - \frac{1}{2}F_{X3} \\ \frac{\sqrt{3}}{2}F_{X3} - \frac{1}{2}F_{Y3} \\ F_{Z3} \\ -\frac{1}{2}M_{X3} - \frac{\sqrt{3}}{2}M_{Y3} - \frac{\sqrt{3}}{2}F_{Z3}R_P \\ \frac{\sqrt{3}}{2}M_{X3} - \frac{1}{2}M_{Y3} - \frac{1}{2}F_{Z3}R_P \\ M_{Z3} - \frac{1}{2} \cdot \frac{\sqrt{3}}{2}F_{X3}R_P + \frac{1}{2} \cdot \frac{\sqrt{3}}{2}F_{X3}R_P - \frac{1}{2} \cdot \frac{1}{2}F_{Y3}R_P - \frac{\sqrt{3}}{2} \cdot \frac{\sqrt{3}}{2}F_{Y3}R_P \end{bmatrix} \quad (4.17)$$

$$\text{Finding out the transport matrix } \mathbf{J}_{to\_centre\_3} = \begin{bmatrix} -\frac{1}{2} & -\frac{\sqrt{3}}{2} & 0 & 0 & 0 & 0 \\ \frac{\sqrt{3}}{2} & -\frac{1}{2} & 0 & 0 & 0 & 0 \\ 0 & 0 & 1 & 0 & 0 & 0 \\ 0 & 0 & -\frac{\sqrt{3}}{2}R_P & -\frac{1}{2} & -\frac{\sqrt{3}}{2} & 0 \\ 0 & 0 & -\frac{1}{2}R_P & \frac{\sqrt{3}}{2} & -\frac{1}{2} & 0 \\ 0 & -R_P & 0 & 0 & 0 & 1 \end{bmatrix} \quad (4.18)$$

Then, the matrices  $\mathbf{J}_{to\_centre\_i}$  have been put as diagonal elements of a newly created 18x18 matrix,  $\mathbf{J}_{to\_centre}$ , that allowed to express the previously obtained vector  $\mathbf{F}_{surface}$  into the 18x1

vector  $\mathbf{F}_{centre\_full}$ , containing the same components of the  $\mathbf{F}_{surface}$  vector, but with reference to the central frame of the platform  $\{X_P Y_P Z_P\}$ :

$$\begin{aligned} \mathbf{F}_{centre\_full} &= \\ &= \begin{bmatrix} [\mathbf{J}_{to\_center\_1}] & [0] & [0] \\ [0] & [\mathbf{J}_{to\_center\_2}] & [0] \\ [0] & [0] & [\mathbf{J}_{to\_center\_3}] \end{bmatrix} \cdot \mathbf{F}_{surface} = \\ &= \mathbf{J}_{to\_centre} \cdot \mathbf{F}_{surface} \end{aligned} \quad (4.19)$$

Finally, in order to obtain a vector of six elements instead of eighteen, it was necessary to use a new 6x18 transformation matrix,  $\mathbf{J}_{reduction}$ , so that the  $F_X$ ,  $F_Y$ ,  $F_Z$ ,  $M_X$ ,  $M_Y$ ,  $M_Z$  components evaluated on the peripheral points of the surface, could be summed up together:

$$\begin{aligned} \mathbf{F}_{centre\_final} &= \\ &= \begin{bmatrix} 1 & 0 & 0 & 0 & 0 & 0 & 1 & 0 & 0 & 0 & 0 & 0 & 1 & 0 & 0 & 0 & 0 & 0 \\ 0 & 1 & 0 & 0 & 0 & 0 & 0 & 1 & 0 & 0 & 0 & 0 & 0 & 1 & 0 & 0 & 0 & 0 \\ 0 & 0 & 1 & 0 & 0 & 0 & 0 & 0 & 1 & 0 & 0 & 0 & 0 & 0 & 1 & 0 & 0 & 0 \\ 0 & 0 & 0 & 1 & 0 & 0 & 0 & 0 & 0 & 1 & 0 & 0 & 0 & 0 & 0 & 1 & 0 & 0 \\ 0 & 0 & 0 & 0 & 1 & 0 & 0 & 0 & 0 & 0 & 1 & 0 & 0 & 0 & 0 & 0 & 1 & 0 \\ 0 & 0 & 0 & 0 & 0 & 1 & 0 & 0 & 0 & 0 & 0 & 1 & 0 & 0 & 0 & 0 & 0 & 1 \end{bmatrix} \cdot \mathbf{F}_{centre\_full} = \\ &= \mathbf{J}_{reduction} \cdot \mathbf{F}_{centre\_full} \end{aligned} \quad (4.20)$$

In the end, all the transformation matrices obtained until now have been included in a global 6x6 transformation matrix  $\mathbf{M}_5$ :

$$\mathbf{F}_{centre\_final} = \mathbf{J}_{reduction} \cdot \mathbf{J}_{to\_centre} \cdot \mathbf{J}_{surface} \cdot \mathbf{J}_{top\_load\_cell} \cdot \mathbf{J}_{bottom\_load\_cell} \cdot \mathbf{J}_{cube} \cdot \mathbf{N} = \mathbf{M}_5 \cdot \mathbf{N} \quad (4.21)$$

Of course, the expression above can be reversed for calculating the axial forces acting on the links, starting from the applied wrench at the platform centre, but  $\mathbf{M}_5$  needs to be invertible, so its determinant needs to be different from zero. Otherwise, some singularity problems may arise in the transformation matrix, leading to system instability, as it will be described in the next paragraph.

## 4.3 Singularities and conditioning problems

### 4.3.1 The Dwarakanath's studies on singularities

The Dwarakanath's observations about the Stewart's platform singularities [56] can be exploited as a useful reference for the evaluation of incipient instability condition of the system under analysis. In particular, the crucial aspect to be evaluated is the stiffness of the sensor, because if it is stiff, then the deformations do not appreciably alter the geometry of the mechanism and the configuration will be decided only by the design parameters. Therefore, in order to sense the external forces, the platform is constrained by six contact points, thus hindering any rigid body motion due to the applied forces. Only this way the externally applied wrench vector  $\mathbf{W}$  would be statically balanced by the vector of the six leg forces  $\mathbf{F}$ , thanks to a 6x6 transformation matrix  $\mathbf{H}$ :

$$\mathbf{W} = \mathbf{H} \cdot \mathbf{F} \quad (4.22)$$

However, the six components of  $\mathbf{F}$  need to be linearly independent, otherwise the system matrix  $\mathbf{H}$  would be singular, and the sensor could not support any load in a given direction, undergoing finite deformation for small loads. Moreover, even when the sensor approaches the near-singularity condition, the system matrix  $\mathbf{H}$  behaves as ill-conditioned and it would result in highly uneven distribution of leg forces in response to loads in specific directions. To ensure the quality of the assumption, the conditioning number of the matrix  $\mathbf{H}$  needs to be computed, paying attention to excessive differences in dimensions and order of magnitude of the involved quantities. In fact, the first three rows of  $\mathbf{H}$  are non-dimensional, while the last three rows contain linear parameters (i.e. the torques arms), that should not exceed too much the order of magnitude of the forces. Anyway, the condition number of  $\mathbf{H}$  is given by:

$$\text{Cond}(\mathbf{H}) = \|\mathbf{H}\| \cdot \|\mathbf{H}\|^{-1} \quad (4.23)$$

where  $\|\mathbf{H}\|$  is identified with the norm of matrix  $\mathbf{H}$ , computed as:

$$\|\mathbf{H}\| = \text{Tr}(\mathbf{H}\mathbf{D}\mathbf{H}^T) \quad (4.24)$$

where  $\mathbf{D} = \text{diag} \left( \frac{1}{n}, \dots, \frac{1}{n} \right)$ , being  $n$  the order of matrix  $\mathbf{H}$ .

Therefore, in order to obtain the design parameters, an optimization problem needs to be formulated as the minimization of  $\text{Cond}(\mathbf{H})$ , establishing that the two radii of the platforms and their relative distance need to assume real, positive values. Moreover, the three angular domains that each link can depict in space are properly defined. Thus, the optimization problem can be solved by means of numerical methods, returning a set of optimal solutions (clusters), in function of the above-mentioned parameters.

### 4.3.2 Conditions of instability of the old version of the shaker

The above-mentioned singularity problems can be useful for the explanation of some issues involving the first version of the shaker, treated in [13], [15] and [16]. As shown in Figure 44, the old structure involved only three single Cardan joints connecting the sliders to the platform, but they resulted unable to stand any torque acting on them. This fact could depend on singularities arising from an ill-conditioned transformation matrix, as illustrated by Dwarakanath.

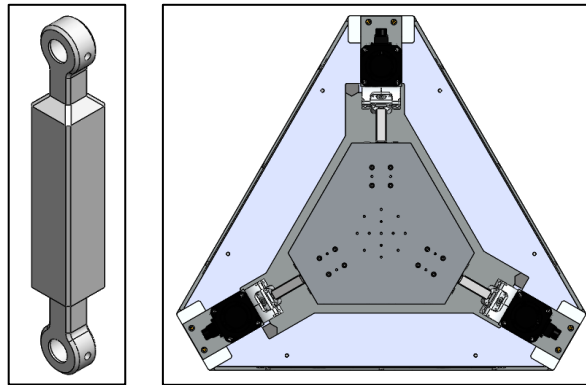


Figure 44: The old version of the shaker: a) Single link; b) Assembly

Hence, the equations derived in the paragraph 4.2 can be employed to demonstrate the instability of the old version of the shaker, even if provided for the new structure. In fact, the only difference between the two models lies in the parameter  $c$  (Figure 41), representing the distance between the centre of each cube and the centre of a bearing, which needs to be set to zero for a correct representation of the old version. Accordingly, the demonstration has been carried out either when the shaker is still and in motion, by the employment of symbolic variables in a *MATLAB*® environment. The code used for such demonstration is shown in



the Appendix B. In particular, in case of zero-position, only two variables  $\beta$  and  $\theta$  can describe all the link angles, assumed constant and independent on the platform motion. Hence, calculating the transformation matrix  $\mathbf{M}_5$  as shown in the previous paragraph, it is possible to obtain the expression of the determinant of this matrix, which reads:

$$\text{Det}(\mathbf{M}_5) = 54c^3 \cos \beta^3 \sin \beta \cos \theta (\cos \beta^2 - 1) \quad (4.25)$$

Consequently, the previous equation can annihilate for specific conditions, leading to singularity of  $\mathbf{M}_5$  that reflects into system instability. In detail:

- $\beta = \pm k \frac{\pi}{2}$  with  $k \in N$ : when this condition occurs, the links would be all positioned horizontally ( $k \in 2N$ ) or vertically ( $k \in 2N + 1$ ) with respect to the ground, thus being unable to stand any vertical or horizontal load respectively.
- $\theta = \pm k \frac{\pi}{2}$  with  $k \in 2N + 1$ : when this condition occurs, the links would be all positioned parallel to the short sides of the platform, thus leading to the same consequences of the previous point.
- $c = 0$ : in this case, a null distance between the links (i.e. a single Cardan joint), would lead to the inability of properly compensating for the torques acting on the links.

Anyway, the instability would never come from the angles, because the domains of  $\beta$  and  $\theta$  will never include the above-mentioned values that lead to singularities [14]. For these reasons, the only way to meet instability comes from the parameter  $c$ , which must be different from zero.

Additionally, a more general computation of the determinant has been performed in function of the platform motion, by means of the *MATLAB*® code reported in the Appendix B. In this case, the position vector  $\mathbf{p} = [x_P \ y_P \ z_P]$  is no more null and it can change according to the three spatial variables values. Therefore, also the angles  $\beta$  and  $\theta$  will change time by time, in function of the position of the end-effector in space, as shown from the equations of the paragraph 4.2. Apart from this, all the equations will remain the same, resulting in a new, complex expression for  $\text{Det}(\mathbf{M}_5)$ . Such equation is cumbersome and its exact expression is

not useful to the discussion, therefore it will not be reported. However, it can be obtained through the above-mentioned script in the Appendix B. Finally, by replacing the  $c$  parameter with zero into the  $Det(\mathbf{M}_5)$  equation, by means of the command “subs”, the overall expression of the determinant annihilates, confirming again the singularity occurrence for a configuration with a single link.

# Chapter 5

## Design of the force platform

### 5.1 Wheatstone's bridge and strain gauges overview

Along with the equations derived in the previous chapter, the logical implementation of a force platform involves the measurement of the axial force into the links. In order to maintain the pre-existing configuration of the shaker, a set of metallic strain gauges has to be applied on the links, according to a Wheatstone's bridge arrangement. Therefore, the measured strain values would be converted into the corresponding axial forces.

#### 5.1.1 The Wheatstone's bridge

The Wheatstone's bridge is a resistive circuit, very common for the strain measurements. The most widespread configuration is the so-called *full bridge*, involving four resistors ( $R_1$ ,  $R_2$ ,  $R_3$  and  $R_4$  [ $\Omega$ ]) and a voltage generator,  $V_S$  [V]. The arrangement consists in three parallel sub-circuits (series of  $R_1$  and  $R_2$ , series of  $R_3$  and  $R_4$ , voltage generator  $V_S$ ), all characterized by the same tension  $V_S$ . The electrical scheme is provided in Figure 45:

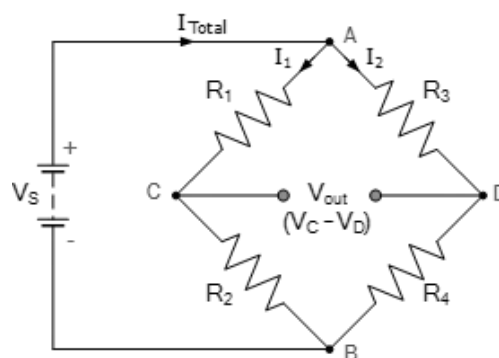


Figure 45: The Wheatstone's full bridge

Using the *voltage divider rule*, it is possible to determine the tensions  $V_C$  (acting on  $R_2$ ) and  $V_D$  (acting on  $R_4$ ), both depending on the voltage generator tension,  $V_S$ . Then, performing a subtraction, it is possible to get the potential difference  $V_{out}$ , representing the output voltage of the circuit, namely:

$$V_{out} = V_C - V_D = V_S \left( \frac{R_1}{R_1 + R_2} - \frac{R_4}{R_3 + R_4} \right) \quad (5.1)$$

Of course, being  $V_S$  a constant, the value of  $V_{out}$  can change only if a variation in the resistors occurs, leading to a bridge unbalance. A balanced bridge  $\left(\frac{R_1}{R_2} = \frac{R_4}{R_3}\right)$ , instead, will always return a null value of  $V_{out}$ , not useful for measurement purposes. Moreover, when acting around the bridge equilibrium, a linearized expression for the  $V_{out}$  holds, stating that the effects on opposite legs of the bridge will sum up, while the effects on adjacent legs will subtract. Therefore, with reference to Figure 45:

$$V_{out} = \frac{V_S G}{4} \left( \frac{\Delta R_1}{R_1} - \frac{\Delta R_2}{R_2} - \frac{\Delta R_3}{R_3} + \frac{\Delta R_4}{R_4} \right) \quad (5.2)$$

where the coefficient  $G$  is called *gauge factor*, it is generally set to 2 and it relates the resistance changes to the strain experienced by a resistor, according to the formula:

$$G = \frac{\Delta R/R}{\Delta L/L} = \frac{\Delta R/R}{\varepsilon} \quad (5.3)$$

Starting from the above-mentioned relationships between resistance and strain, the working principle of the strain gauge has been derived.

### 5.1.2 Strain gauge working principle

The strain gauges (Figure 46) are simple measurement sensors, consisting in a metallic or semiconductor filaments that act as resistors when employed in a Wheatstone's circuit. The gauges need to be glued on the components where to monitor the state of stress and, to some extent, they become part of it, detecting the deformation which the component is undergoing under a certain load. Basically, if the transversal section of a resistor reduces (e.g. in case of tension), a related increase in the resistance, equal to  $\Delta R$ , will be noticed; otherwise (e.g. in case of compression), a  $\Delta R$  reduction will be observed.

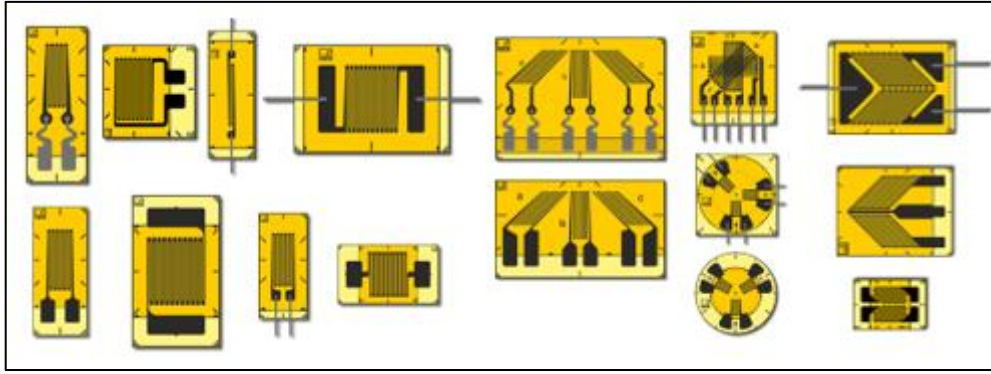


Figure 46: Examples of strain gauges

Of course, the typology and the mutual position of gauges would change in function of the stress state to be detected and of the environmental conditions in which the measure needs to be performed (e.g. chemical reactivity, high temperatures, underwater...).

### 5.1.3 Configuration for axial strain measurement

As mentioned in the previous paragraph, the choice of proper gauges and their arrangement in a Wheatstone's bridge depend on the kind of stress to be measured. In the present work, the need for measuring an axial strain acting on a link subjected to traction or compression load, calls for using the *full bridge type III*, whose configuration is provided in Figure 47:

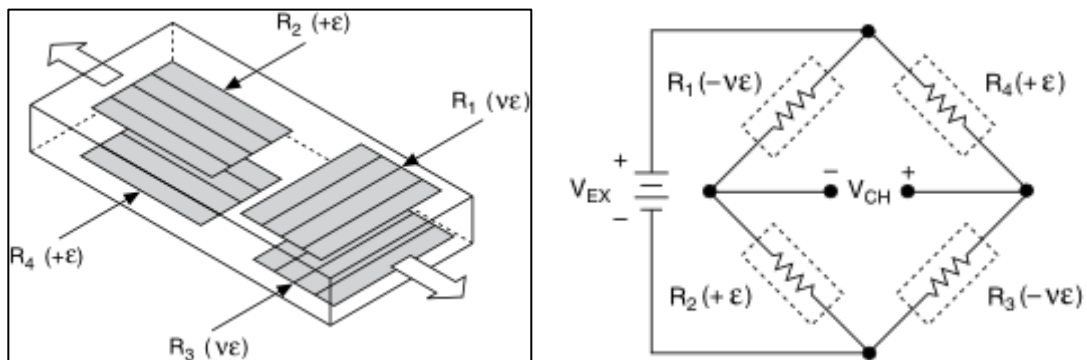


Figure 47: Full bridge type III: a) Gauges arrangement on a beam; b) Electrical scheme

For this configuration, the expressions of the strains can be resumed as follows:

$$\begin{cases} \varepsilon_{1,3} = -\frac{v\sigma}{E} = -\frac{vN}{EA} \\ \varepsilon_{2,4} = \frac{\sigma}{E} = \frac{N}{EA} \end{cases} \quad (5.4)$$

where the gauges 2 and 4 (called *principal active gauges*) experience a tension along their axes, with consequent reduction of section and a corresponding positive resistance change; instead, the gauges 1 and 3 (called *Poisson's active gauges*) compress laterally, increasing their cross-section, thus resulting in a negative resistance change. In this case, the linearized expression for  $V_{out}$  reads:

$$V_{out} = \frac{V_S G}{4} \left[ \frac{2(1 + \nu)N}{EA} \right] \quad (5.5)$$

Moreover, the employment of the *full bridge type III* configuration allows to compensate for the temperature effects, for the strain generated by bending and for the lead resistance of the wires, thus providing only the axial strain contribution [63].

## 5.2 Experimental equipment

In order to perform the tests, linear standard strain gauges with solder tabs, model *LY-41 10/120* by *HBM*, have been employed and their features are then provided in Table 25:

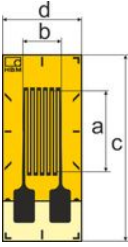
	Dimension		Feature	Value
	a	10 mm	Resistance	$120 \Omega \pm 0.35\%$
b	4.9 mm	Gauge factor	$2.06 \pm 1.0\%$	
c	18 mm	Transverse sensitivity	0.2%	
d	8 mm	Max $V_S$ of excitation	13 V	

Table 25: HBM's LY-41 10/120 strain gauge features

The thermal characteristics have not been considered because they would be compensated in a *full bridge* arrangement while, in a half bridge pattern, they would not induce any relevant measurement corruption. Anyway, the above-mentioned strain gauges are easy to install, thanks to their solder tabs, and provide good reliability with both steel and aluminum.

Hence, the bridge has been connected to a *National Instruments' 9237* simultaneous bridge module (Figure 48) with an input range of  $\pm 25$  mV/V and up to 10 V of internal voltage excitation. It is worth to underline that the bridge module choice has been almost free, because only one out of the four channels was needed for plugging the connector.



Figure 48: National Instruments' 9237 simultaneous bridge module

### 5.3 Floor noise evaluation

Before installing the gauges on the shaker, a floor noise evaluation has been performed, in order to assess the gauge capability in detecting strain variations in unloaded conditions. Thus, the above-mentioned gauges have been arranged in a Wheatstone's *half bridge type II*, while the signal has been acquired and processed through the already described bridge module. The circuit lied on the upper and lower surfaces of an aluminum suspended beam, clamped at one end through a manual vice, as shown in Figure 49:

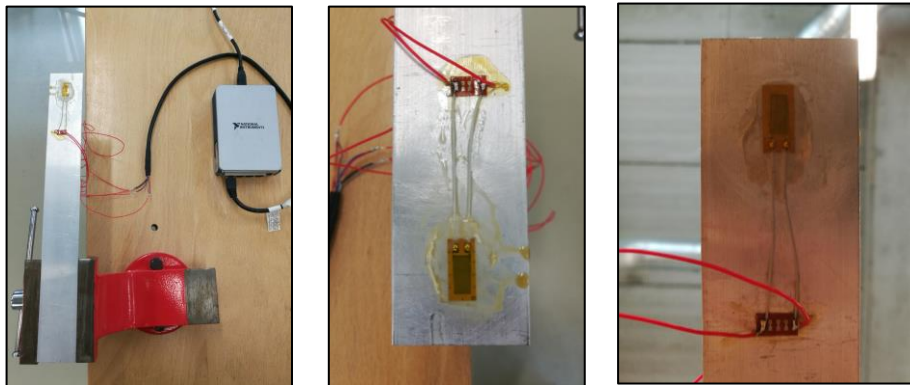


Figure 49: Floor noise evaluation - a) Setup; b) Top view; c) Bottom view

Once connected the gauges to the bridge module, three different measurement campaigns have been performed in three different moments of the day, ensuring the independence of the sampling stories. Moreover, for each campaign, ten records of 10 seconds each have been acquired through *MeasLab© Data Acquisition*, choosing a sampling frequency of 2 kHz. Then, the temporal history has been filtered through a Butterworth's high-pass filter of eighth order with a cutting frequency of 100 Hz. The obtained data have been manipulated

in the *MeasLab*© *Analyzer* suite, that allowed to perform a statistical analysis on the temporal profiles shown in Figure 50, Figure 51 and Figure 52.

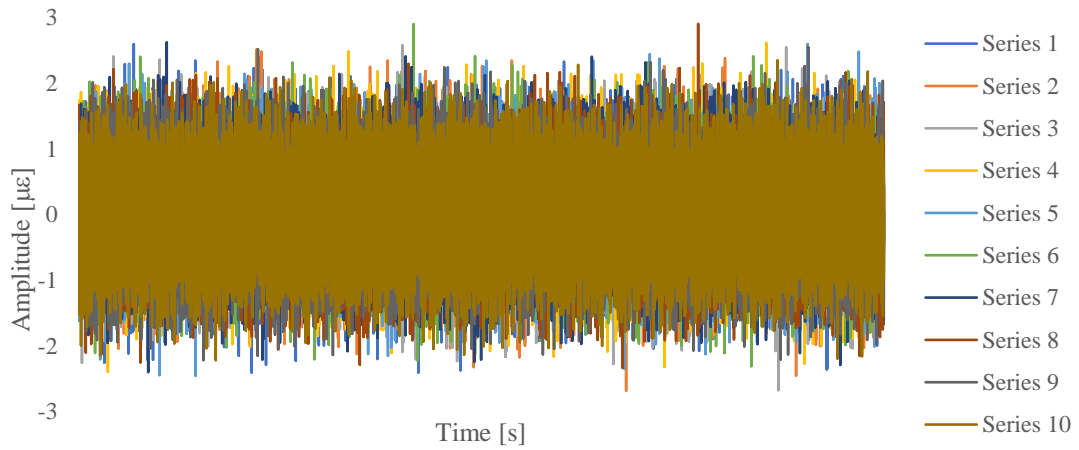


Figure 50: Floor noise evaluation - First series

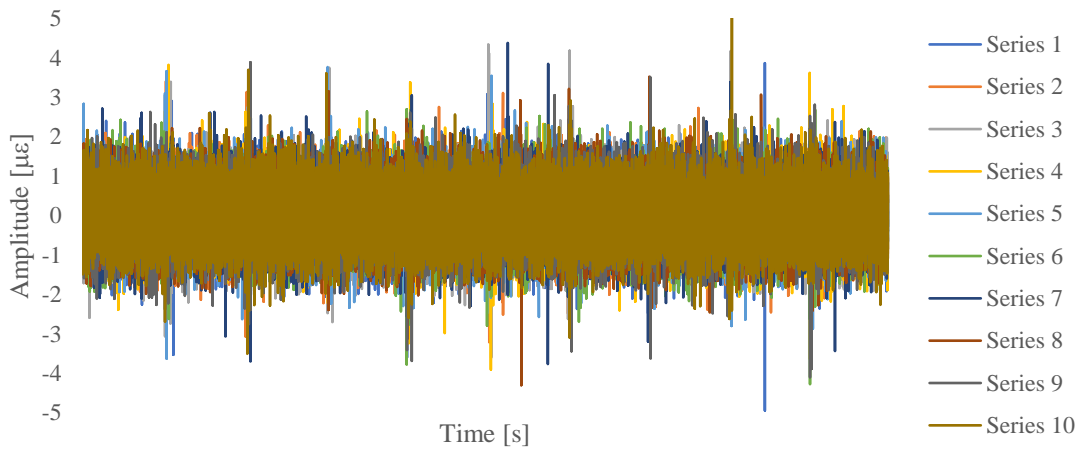


Figure 51: Floor noise evaluation - Second series

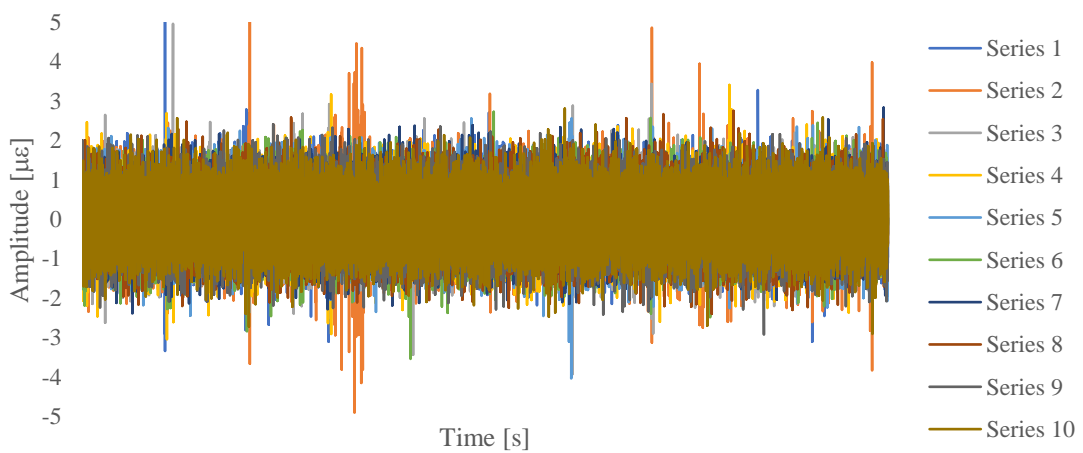


Figure 52: Floor noise evaluation - Third series



In particular, for each campaign, the RMS and the variance have been calculated over the ten histories belonging to the mentioned campaign, using the data provided in Table 26.

#	$\sigma^2$	RMS	#	$\sigma^2$	RMS	#	$\sigma^2$	RMS
1	0.403	0.635	11	0.419	0.648	21	0.407	0.638
2	0.402	0.634	12	0.406	0.637	22	0.440	0.663
3	0.400	0.633	13	0.413	0.643	23	0.415	0.644
4	0.399	0.631	14	0.413	0.643	24	0.408	0.639
5	0.397	0.630	15	0.413	0.642	25	0.404	0.636
6	0.405	0.637	16	0.409	0.640	26	0.408	0.639
7	0.404	0.636	17	0.411	0.641	27	0.398	0.631
8	0.395	0.628	18	0.398	0.631	28	0.404	0.636
9	0.398	0.631	19	0.420	0.648	29	0.406	0.637
10	0.396	0.629	20	0.409	0.640	30	0.400	0.632
$\Sigma$	3.999		$\Sigma$	4.113		$\Sigma$	4.091	
$\Sigma/10$	0.400		$\Sigma/10$	0.411		$\Sigma/10$	0.409	
$\sqrt{\quad}$	0.632	<b>0.632</b>	$\sqrt{\quad}$	0.641	<b>0.641</b>	$\sqrt{\quad}$	0.640	<b>0.640</b>

Table 26: Floor noise evaluation - Variance and RMS of the three series

After that, the ten variances of each series have been summed up, then divided by 10 (i.e. the sample size). Extracting the root of the obtained values, the standard deviations of the three series have been derived. Moreover, being the floor noise mean equal to zero, the latter standard deviation values directly corresponded to the averaged RMSs of the three series. Finally, performing a further average of the three RMSs, the minimum strain value that could be perceived from the gauges has been obtained, corresponding to  $0.638 \mu\epsilon$ .

## 5.4 Preliminary experiments

### 5.4.1 Strain gauges installation

The experimental arrangement entails the installation of a *full bridge type III* onto only one of the six links of the shaker, aiming to demonstrate the system capability in detecting strain variations when undergoing static vertical loads. Indeed, in case of a positive outcome, the same bridge configuration would be applied onto all the other links, otherwise a different sensing technique might be employed. Thus, the installation involved two couples of strain gauges, glued on opposite sides of the link subjected to axial load, as shown in Figure 53:

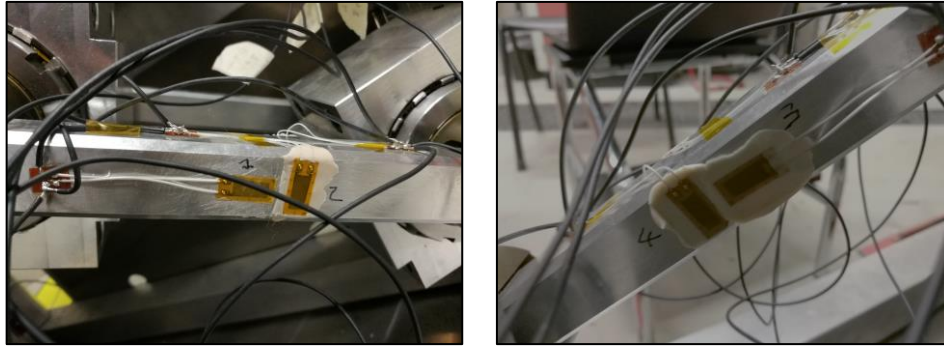


Figure 53: Strain gauges installation on a link: a) Left view; b) Right view

Therefore, in order to get the axial strain signal, each principal gauge has been connected to both the Poisson gauges, obtaining four cables from the initial eight ones, to be further linked to a pinned ethernet terminal. Finally, the two cables derived from joining the two gauges of the same side, have been connected to the measurement signal output pins, while the other two have been welded to the excitation voltage and sensor line pins.

### 5.4.2 Methodology

In order to reconstruct the evolution of the signal in a calibration curve, a simple method has been deployed and reiterated for three times, so as to ensure the repeatability of the tests. Indeed, a first signal acquisition has been performed without any mass at the platform centre, in order to determine the floor noise of the measurement chain. After that, the loading phase has been undertaken, by sequentially adding 10, 20, 40, 50 and 60 kg. Then, the same methodology has been employed for the unloading phase, until a floor noise final acquisition closed the experiment. In order to acquire the signal, *MeasLab*© *Data Acquisition* has been run without using any filter, according to the setup parameters shown in Table 27:

Bridge information		Strain gage information	
Information	Value	Information	Value
Measurement type	Strain gage	Gage factor	2.06
Units	Strain	Nominal gage resistance	120 $\Omega$
Strain configuration	Full Bridge III	Poisson's ratio	0.3
Initial bridge voltage	0 V	Sampling	
Voltage excitation source	Internal	Sampling rate	2048 Hz
Voltage excitation value	5 V	Buffer time length	10 s

Table 27: *MeasLab*© setup for signal acquisition

### 5.4.3 Results

Thereby, the acquired signals have been filtered and plotted by means of *MeasLab*® *Analyzer*, a post-processing dedicated software. In particular, an eighth order Butterworth's low-pass filter, with a cutting frequency of 30 Hz, has been employed to better observe the signals. In the following plots, an initial experiment (Figure 54) has been performed, varying the mass on the platform every 15 seconds without stopping the acquisition. This continuous record would visually help distinguishing the loading and unloading phases. Then, the first series (Figure 55), the second series (Figure 56) and the third series (Figure 57) of signals are shown, bearing in mind that each single observation lasted 10 seconds.

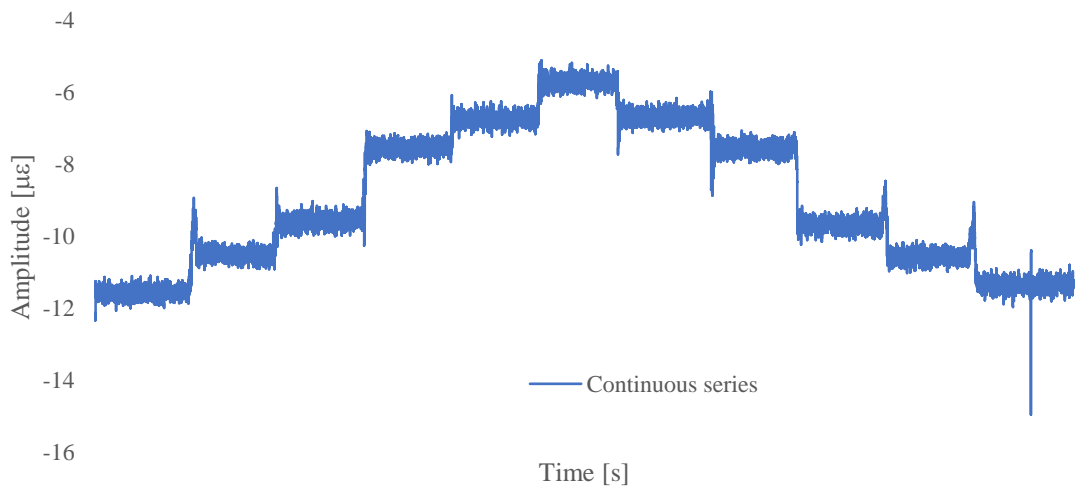


Figure 54: Signal acquisition - Continuous series

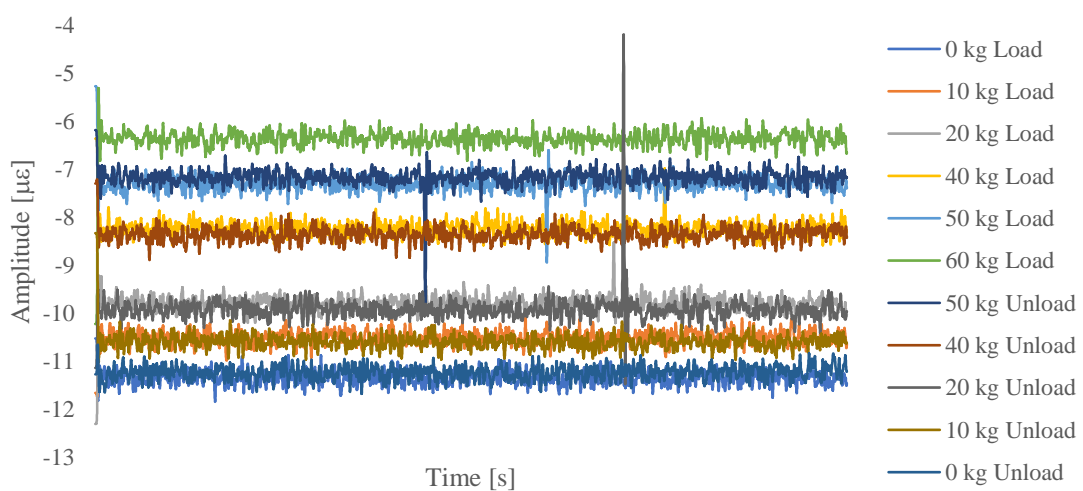


Figure 55: Signal acquisition - First series

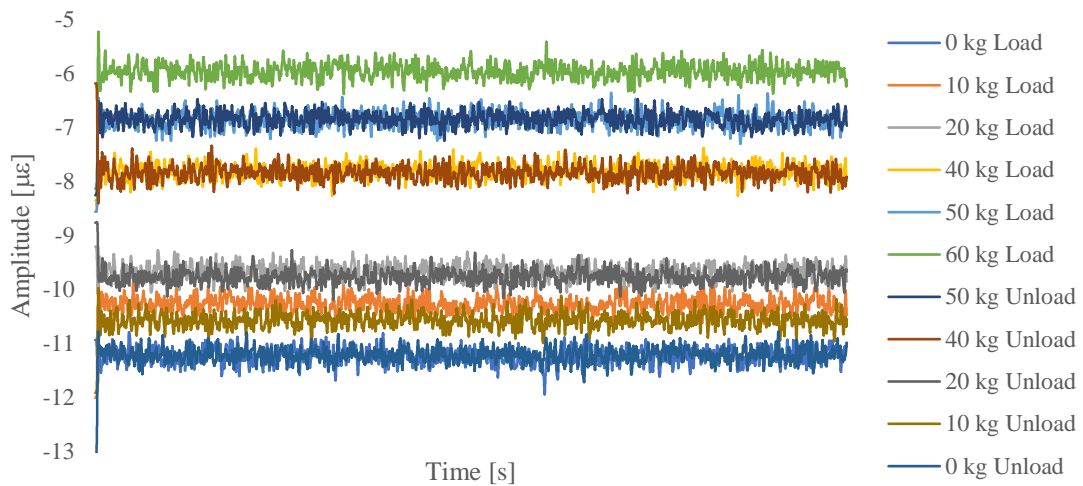


Figure 56: Signal acquisition - Second series

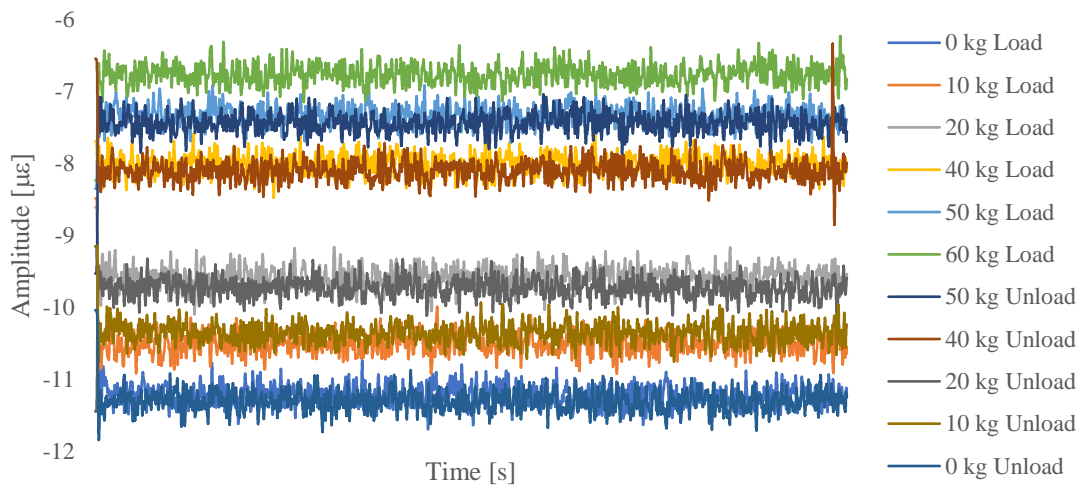


Figure 57: Signal acquisition - Third series

As inferred from the previous plots, the signals proved the desired repeatability of the experiments. In fact, for the same amount of load at the platform centre, the registered strain values are almost the same in all the three series; indeed, in the same series, the measured strain results in higher values for higher applied masses, confirming the expectations. Moreover, no significant differences have been noticed between the loading and unloading phases for the same applied mass. Hence, the plots attest that the measurement system installed on a link is able to detect the axial strain variations with sufficient accuracy. Additionally, it is possible to use *MeasLab*© Analyzer to make a comparison between the floor noise evaluated in the paragraph 5.3 and the one inferred from the above tables. In fact, using a Butterworth's high-pass filter of eighth order with a cutting frequency of 100 Hz on the signals coming from the links in presence of no load ("0 kg"), an averaged RMS of 0.763

$\mu\epsilon$  can be obtained. This result has the same order of magnitude of the value computed with the suspended beam chain ( $0.638 \mu\epsilon$ ), attesting only a slight difference in the measurement, probably due to little variations in the environmental conditions where the tests have been performed. After that, a further analysis of the statistical data related to the signal can be deployed, in order to obtain a calibration curve of the measurement chain.

#### 5.4.4 Calibration curve

The acquired signals of the three series are all characterized by two main statistical indicators, the mean and the standard deviation. These two descriptors have been computed for the first series in Table 28, for the second series in Table 29, and for the third series in Table 30.

<b>First series of experiments</b>				
<b>Mass on the platform [kg]</b>	<b>Mean [<math>\mu\epsilon</math>]</b>		<b>Standard deviation [<math>\mu\epsilon</math>]</b>	
	<b>Loading</b>	<b>Unloading</b>	<b>Loading</b>	<b>Unloading</b>
0	-11.34	-11.24	0.14	0.14
10	-10.50	-10.59	0.15	0.18
20	-9.80	-9.92	0.20	0.27
40	-8.23	-8.36	0.17	0.15
50	-7.30	-7.17	0.18	0.18
60	-6.37	-6.37	0.24	0.24

Table 28: Mean and standard deviation of the first series of signals

<b>Second series of experiments</b>				
<b>Mass on the platform [kg]</b>	<b>Mean [<math>\mu\epsilon</math>]</b>		<b>Standard deviation [<math>\mu\epsilon</math>]</b>	
	<b>Loading</b>	<b>Unloading</b>	<b>Loading</b>	<b>Unloading</b>
0	-11.24	-11.22	0.14	0.16
10	-10.28	-10.58	0.16	0.15
20	-9.68	-9.77	0.14	0.14
40	-7.82	-7.84	0.13	0.16
50	-6.87	-6.85	0.16	0.15
60	-5.97	-5.97	0.18	0.18

Table 29: Mean and standard deviation of the second series of signals

Third series of experiments				
Mass on the platform [kg]	Mean [ $\mu\epsilon$ ]		Standard deviation [ $\mu\epsilon$ ]	
	Loading	Unloading	Loading	Unloading
0	-11.22	-11.31	0.18	0.15
10	-10.51	-10.36	0.17	0.15
20	-9.59	-9.74	0.15	0.16
40	-8.01	-8.11	0.13	0.17
50	-7.34	-7.45	0.14	0.17
60	-6.77	-6.77	0.16	0.16

Table 30: Mean and standard deviation of the third series of signals

From the previous data, a scatterplot (Figure 58) of the mean  $\mu$  values has been derived and the standard deviation  $\sigma$  values have been employed to determine the error bands for each loading or unloading condition, being added to or subtracted from the mean values.

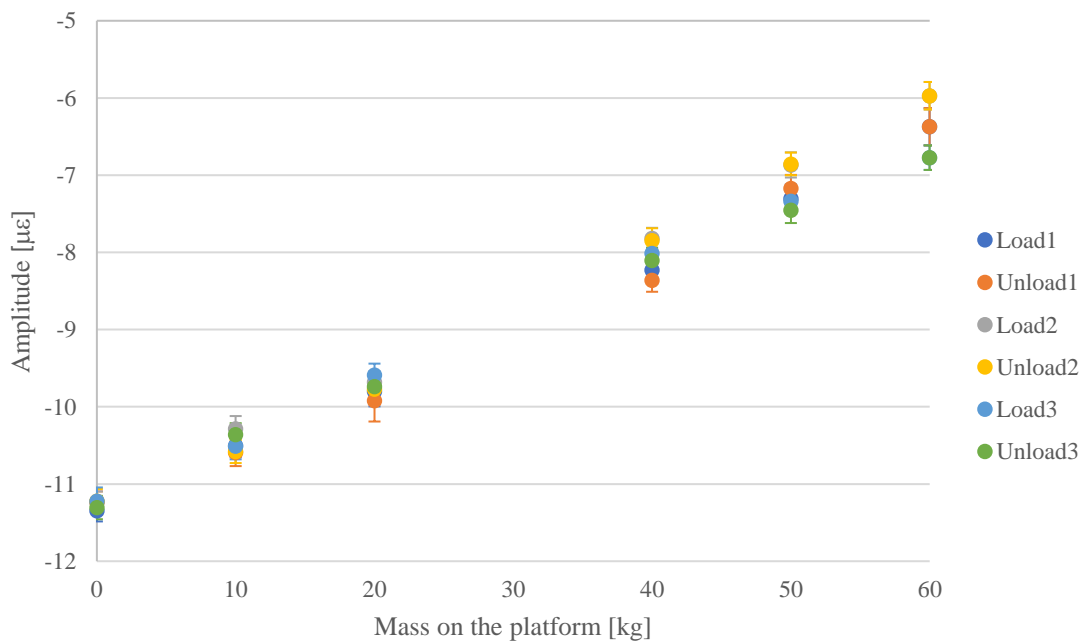


Figure 58: Signal acquisition - Scatterplot with error bands

The trend clearly shows a proportional increase in the strain output and in the width of the error bands for higher values of mass applied on the platform. Furthermore, these data can be employed to build up a regression model, useful for determining the calibration curve. This curve is useful for describing the actual relationship between the input and output quantities, and it needs to be derived by means of more experimental points, because of [64]:

- *Nonlinearity errors*: random errors or internal nonlinearities of the instrument, that do not ensure the perfect linearity of the relationship. In fact, given a line passing through two experimental points, it is impossible to know if, a priori, a third experimental point would lie on the same line.
- *Hysteresis*: the output obtained from the loading phase can be different from the one obtained from the unloading phase, even if the input is the same.
- *Repeatability*: different series of testing, although performed in the same environmental conditions, can return different outputs. This means that more cycles are needed to correctly represent the output for a given input.

In particular, the method of *least squares error* (LSE) has been employed to minimize the sum of the squares of the residuals, namely the differences between the experimental output and the expected output lying on the interpolating line, in presence of the same input:

$$LSE = \min \left[ \sum_{i=1}^n \left( y_{i,experimental} - y_i(x_i) \right)^2 \right] \quad (5.6)$$

In order to proceed, the dependent and independent variables have been switched, so as to have the applied mass (input) on the y-axis, and the strain amplitude (output) on the x-axis. Then, the linear regression function has been computed, obtaining the following interpolating equation and *linear correlation coefficient*,  $R^2$ :

$$y = 12.04x + 136.51 \quad (5.7)$$

$$R^2 = 0.988 \quad (5.8)$$

The value of  $R^2$  close to the unity testifies that the linear approximation of the measurements is acceptable, while the interpolating equation has been employed to compute the strain values lying on the regression line, to be compared with the experimental outputs, in order to get the residuals for any input. After that, in order to reconstruct the uncertainty bands

over the regression line, the value  $u$  has been computed, according to the formulation of the so-called *mean squared error* (MSE):

$$u = MSE = \sqrt{\frac{\sum_{i=1}^n (y_{i,experimental} - y_i(x_i))^2}{n}} \quad (5.9)$$

After that, given a confidence level of the 95% based on a normal distribution (because working on 36 samples, so  $n > 10$  forbids for using a t-student curve), the  $u$  value has been multiplied times 1.96, obtaining:

$$u_{95\%} = 1.96 u = 0.39 \mu\epsilon \quad (5.10)$$

The  $u_{95\%}$  value allowed the calculation of the upper and lower bands of uncertainty, simply by summing and subtracting its value from the expected one, lying on the interpolating line, as plotted in Figure 59 and shown in Table 31. In particular, the blue line represents the expected, interpolating line, while the upper band (orange) and the lower band (grey) have been obtained as mentioned above.

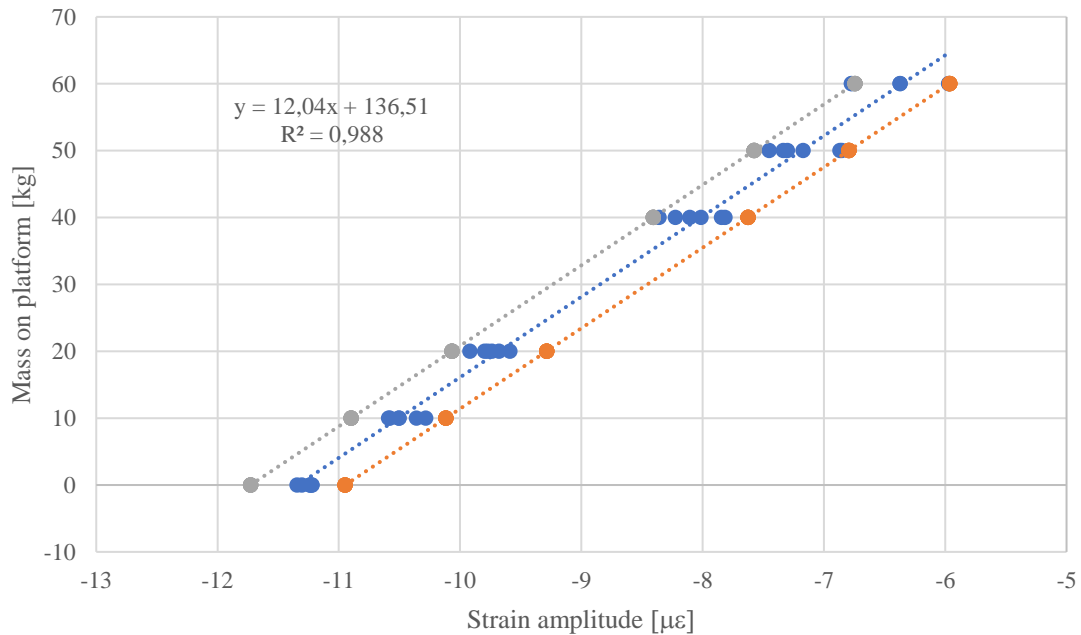


Figure 59: Signal acquisition - Calibration curve and uncertainty bands (plot)



Mass on the platform [kg]	Output value [ $\mu\epsilon$ ]		
	Expected	Upper band	Lower band
0	-11.34	-10.95	-11.73
10	-10.51	-10.12	-10.90
20	-9.68	-9.29	-10.07
40	-8.02	-7.63	-8.41
50	-7.19	-6.79	-7.58
60	-6.35	-5.96	-6.75

Table 31: Signal acquisition - Calibration curve and uncertainty bands (values)

Therefore, the experiments demonstrated a good linearity and repeatability, testifying a good response of the system to the static inputs. This would allow applying the same procedure to the other five links, and then combining the output strain data. Moreover, a study on error propagation would be suitable, in order to understand if the model is robust enough for the representation of the force transmission.

## 5.5 MonteCarlo simulations for error propagation

### 5.5.1 Methodology

Once determined the calibration curve for the strain gauge chain mounted on a link, it is possible to study the measurement error propagation by means of a MonteCarlo simulation. Anyway, being the calibration curve derived from averaged measurement values, its uncertainty would not be suitable for simulating the actual, greater uncertainty that characterizes the signal. Therefore, in the following method, the uncertainty has been set to  $0.763 \mu\epsilon$  (the floor noise value computed in the paragraph 5.4.3), representing the minimum strain detectable by the measurement chain.

Then, the procedure (available in the Appendix C) started with the determination of the transformation matrix  $\mathbf{M}_5$  as shown in the previous chapter, paying attention to its singularity, because the relationship to derive the axial forces vector  $\mathbf{N}$  from the central wrench vector  $\mathbf{F}_{centre\_final}$  reads:

$$\mathbf{N} = \text{inv}(\mathbf{M}_5) \cdot \mathbf{F}_{centre\_final} \quad (5.11)$$

Once obtained  $\mathbf{M}_5$ , the analysis required to define the components of the vector  $\mathbf{F}_{centre\_final}$ . For this purpose, three load levels (10, 100 and 1000) have been applied, one at a time, over all the six directions, so to obtain eighteen different vectors  $\mathbf{F}_{centre\_final}$ , each one characterized by five null components and only one non-zero quantity. This procedure, included in a cycle, led to the determination of the vector  $\mathbf{N}$  for each one of the eighteen loading conditions. Then, the vector of axial strains has been found, by means of the stress-strain relationship:

$$\varepsilon = \frac{\sigma}{E} = \frac{N}{EA_0} \quad (5.12)$$

After that, the core of the MonteCarlo simulation has been developed, starting from above-mentioned uncertainty value  $u$  of  $0.763 \mu\varepsilon$ . This value can be intended as a standard deviation value, characterizing the normal distribution from which random error values have been generated time by time. In fact, once chosen the number of iterations to be performed,  $n$ , a  $6 \times n$  matrix has been created, providing  $n$  error values for each of the six loading directions and for every load level. Hence, a strain matrix with the same dimensions has been built-up, replicating the  $6 \times 1$  strain vector over the  $n$  columns. Then, the two matrices of errors and strains have been summed up, obtaining a new strain matrix, made up by strain components affected by random errors. Of course, the higher the number of iterations  $n$ , the more robust would be the algorithm, because many samples allow to smooth the results appearance: in the present work, a set of 100000 iterations has been performed. After that, a  $6 \times n$  matrix of axial stresses  $\mathbf{N}_{mat}$  has been obtained by multiplying the strain-error matrix times  $EA_0$ , and subsequently employed for the derivation of the  $6 \times n$  matrix  $\mathbf{F}_{centre\_final\_mat}$ , containing the central wrench components corresponding to the measured axial stresses affected by error, according to the formulation:

$$\mathbf{F}_{centre\_final\_mat} = \mathbf{M}_5 \cdot \mathbf{N}_{mat} \quad (5.13)$$

Thereafter, the mean squared error has been computed for each one of the eighteen loading conditions, converting an output matrix of  $6 \times n$  force components into a six-sized vector containing only MSEs. In order to do so, the reference vector  $\mathbf{F}_{centre\_final}$  has been transformed into a  $6 \times n$  matrix, made up of  $n-1$  null columns, and one column equal to the actual  $\mathbf{F}_{centre\_final}$

vector. The comparison of the two vectors returned an estimation of the error lying between the actual applied load and the measured one, although the result might slightly vary time by time, given the random nature of the error generated in the MonteCarlo routine.

## 5.5.2 Results

In order to absorb the fluctuations, the simulations have been run twelve times, so as to observe twelve values of each component of error. Then, discarding the maximum and the minimum value in each case, an average on the ten remaining samples has been performed, resulting in the quantities shown in Table 32. In the same table, no distinction among the three different load levels has been made, because from the iterations arose the independence of the error from the applied load level, thus allowing to prescind from it.

Load Direction	Mean Squared Error on $F_{centre\_final}$ components					
	$F_X$ [N]	$F_Y$ [N]	$F_Z$ [N]	$M_X$ [Nm]	$M_Y$ [Nm]	$M_Z$ [Nm]
$F_X$ [N]	40.26	40.25	44.05	5.49	5.50	4.55
$F_Y$ [N]	40.24	40.30	44.03	5.50	5.49	4.56
$F_Z$ [N]	40.17	40.23	44.06	5.49	5.48	4.56
$M_X$ [Nm]	40.25	40.19	44.07	5.48	5.49	4.55
$M_Y$ [Nm]	40.30	40.22	44.04	5.49	5.50	4.56
$M_Z$ [Nm]	40.24	40.25	44.04	5.49	5.49	4.55

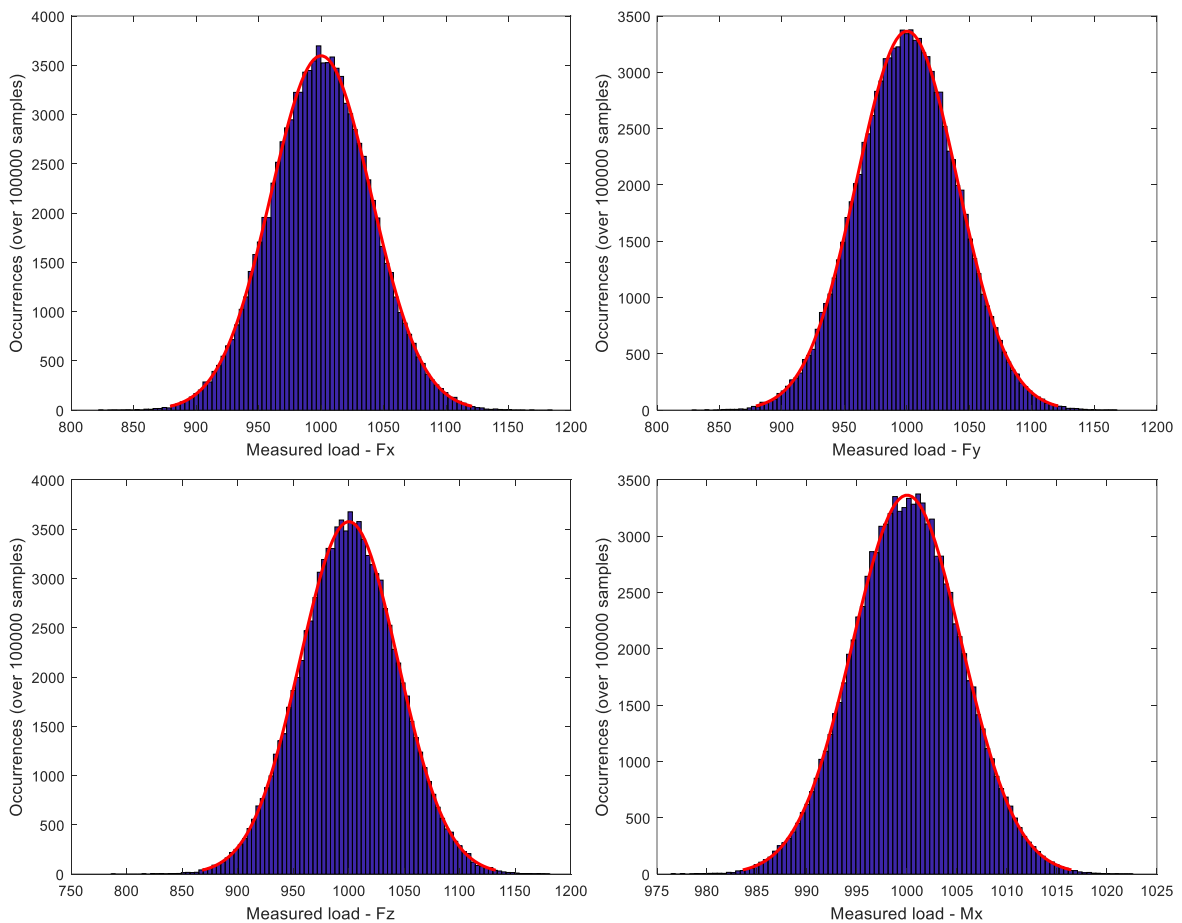
Table 32: MSEs from MonteCarlo simulations

Then, repeating that the applied load would not affect the measurement error, a set of histograms has been generated for a load level equal to 1000, and then plotted in Figure 60 for showing the difference between a load applied on a certain direction, and its measured value on the same direction. In particular, plotting histograms of a hundred frequency classes with a normal fitting (*MATLAB*® command “histfit”) and extracting their mean and standard deviation values (*MATLAB*® command “fitdist”), it has been possible to show that the obtained measurements were distributed on a Gaussian curve. This assumption has then confirmed by performing a hypothesis test and computing its p-value. In detail, the null hypothesis  $H_0$  has been set to 1000 (i.e. the mean of the measured forces distribution coincides with the actual applied load) and the  $\alpha$  significance level set to 0.05, reflecting the already adopted experimental confidence of 95%. Then, for each distribution, a set of ten

routines has been run, and their values of mean and standard deviation employed to perform a z-normalization process. As a result, all the normalized z-values converged to 0, corresponding to a p-value of 0.5. Therefore, the null hypothesis  $H_0$  would never be refused, because the p-value is greater than the chosen  $\alpha$ , thus confirming that the distributions can be fitted very well by a normal curve. Also graphically, the obtained histograms closely resemble to a Gaussian, with a mean value almost coincident to the actually applied load, and a standard deviation close to the MSEs tabled in Table 32. These data are all available in Table 33:

	Load direction					
	$F_x$ [N]	$F_y$ [N]	$F_z$ [N]	$M_x$ [Nm]	$M_y$ [Nm]	$M_z$ [Nm]
$\mu$ [N]	1000.04	1000.06	1000.06	1000.01	1000.02	1000
$\sigma$ [N]	40.26	40.30	44.06	5.48	5.50	4.55

Table 33: Normal distributions parameters of Figure 60



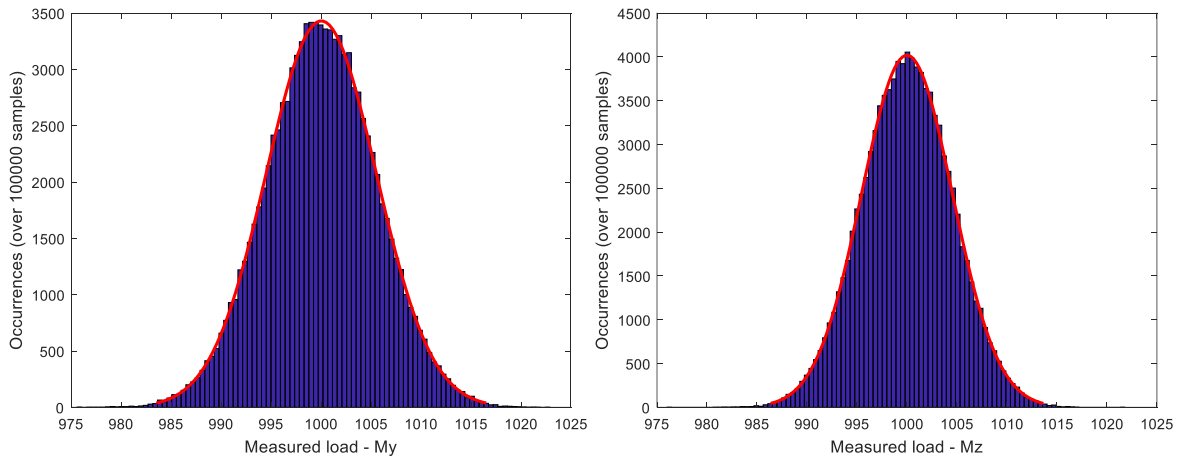


Figure 60: Normal distributions from histograms for the measured force components

Therefore, as inferred from the previous analyses, the error characterizing the load measurements resulted in about 40 N for the forces and more than 4 Nm for the torques. Indeed, the two error values are still too high for ensuring a good reliability of the measurement system when a subject is standing on the platform. Of course, the first improvements to be adopted may deal with the measurement uncertainty reduction, in order to diminish the standard deviations of the experiments, thus centering the distributions around the mean values. Once cleared this issue, some suggestions and possible developments have been proposed.

# Chapter 6

## Discussion and future developments

### 6.1 Installation of strain gauge bridges on all the links

As demonstrated in the previous chapter, the feasibility study about the axial strain measurements on the gauge-equipped link returned a positive match, in terms of sensitivity and signal uncertainty. Therefore, the first step to perform in the future would be the installation of the same Wheatstone's *full bridge type III* on all the other five links, capturing the data with the same procedure and deriving the related calibration curves. Anyway, the new measurement system would involve six distinct channels, each one related to a single link, thus calling for dropping out the *National Instruments' 9237* bridge module employed up to now, because equipped with only four channels. This fact implies the choice of a similar bridge module in terms of input range and internal voltage excitation, in order to derive calibration curves analogous to the one obtained in the present work. Finally, once installed the extensimetric bridges on all the links, it would be also possible to employ the previously derived static equations, so to correctly reconstruct the vector of forces and torques acting at the centre of the platform.

### 6.2 RC circuit for low-pass filter installation

Another interesting solution for getting an improved output from the strain gauge chain can involve the installation of a physical low-pass filter. In fact, this device is made up by a passive circuit that can modify, reshape or reject the frequencies of a signal that lie above a certain threshold, mostly useful if the expected output is characterized by the same order of magnitude of the high frequency floor noise. Thereby, for low frequency applications, the series of a *resistor* and a *capacitor* (RC) would be the cheapest and easiest solution to be employed in an existing bridge circuit, and because of the presence of only one reactive component (the capacitor), the device is also known as *first order filter* (Figure 61):

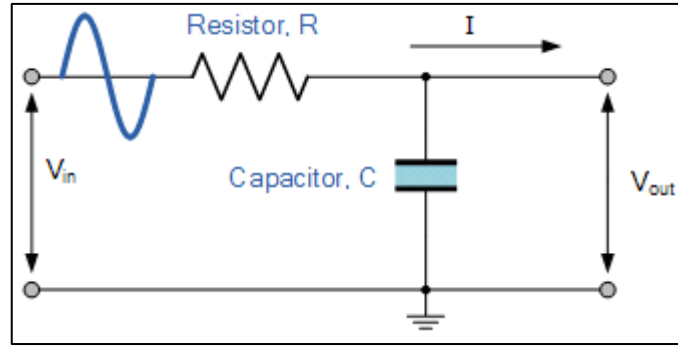


Figure 61: RC circuit for low-pass filter installation

In particular, the input signal  $V_{in}$  is applied to both the components, while the output signal  $V_{out}$  is taken across the capacitor only, linked together by the formulation of the voltage divider equation for an *alternate current* (AC) circuit:

$$V_{out} = V_{in} \frac{X_C}{Z} = \frac{X_C}{\sqrt{R^2 + X_C^2}} = \frac{\frac{1}{2\pi f C}}{\sqrt{R^2 + \left(\frac{1}{2\pi f C}\right)^2}} \quad (6.1)$$

where  $X_C [\Omega]$  is the capacitor reactance, inversely proportional to the signal frequency  $f [Hz]$  and the capacity of the component  $C [F]$ , while  $Z [\Omega]$  is the impedance, function of the reactance (imaginary part) and resistance  $R [\Omega]$  (real part). From the above formulation arises that, for increasing values of frequency, the output of the signal will decrease, thus leading to a filtering effect. Moreover, if two or  $n$  RC circuits of the first order will be connected in series, a second (or  $n$ -th) order filter can be obtained, leading to an increased filtering capacity, though involving a decrease in gain and accuracy of the output signal.

### 6.3 Sensitivity improvement and amplification

Once completed the previous procedures, some considerations about the amplification of the signal can be done. In fact, in presence of structures similar to the shaker involved in the present work, the axial strain contribution along the links can assume very little values, often of the same order of magnitude of the floor noise, or anyway too small for being detected properly. Therefore, the creation of a notch on a link body would increase the stress concentration in the measurement zone, in a way that the gauges could return better results

in terms of amplification. Then, in relation to the ease of realization, the best notch to choose would be a passing hole, whose diameter needs to be determined in the next steps.

### 6.3.1 Notch model

Considering the hypothesis of linear stress-strain dependence (valid for aluminum, the material used for the links), and the presence of a notch of diameter  $d$  [mm], the following expression holds for an axial force  $N$  [N] acting on the cross-section of the link (Figure 62):

$$\varepsilon = \frac{\sigma_{max}}{E} = \frac{N}{EA_{eff}} k_t(d) = \frac{N}{E(A_0 - bd)} k_t(d) \quad (6.2)$$

where all the variables depend on the geometry of the link and the material properties, as reported in Table 34.

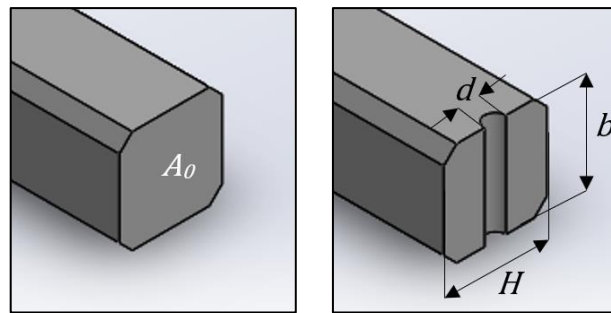


Figure 62: Link geometry: a) Full section; b) Notched section

Link Properties	E [MPa]	A <sub>0</sub> [mm <sup>2</sup> ]	b [mm]	H [mm]
	69000	558	24	24

Table 34: Geometric and elastic properties of a link

The only missing value is the  $k_t$  expression, which represents the notch coefficient for a hole in a finite plate subjected to axial load. Anyway, empirical diagrams and formulations are easily available in literature, as the one proposed by Stewart [65], provided in Figure 63:

$$k_t = 3 - 3.14 \left(\frac{d}{H}\right) + 3.667 \left(\frac{d}{H}\right)^2 - 1.527 \left(\frac{d}{H}\right)^3 \quad (6.3)$$



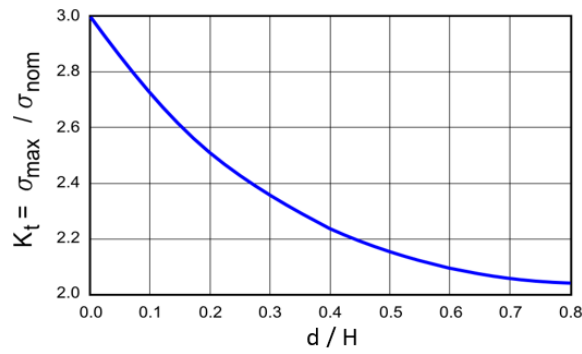


Figure 63: Notch coefficient  $k_t$  diagram [65]

Then, substituting the  $k_t$  into the strain expression,  $\varepsilon$ , the following third order equation in  $d$  can be obtained:

$$\varepsilon = \frac{N}{E(A_0 - bd)} \left[ 3 - 3.14 \left( \frac{d}{H} \right) + 3.667 \left( \frac{d}{H} \right)^2 - 1.527 \left( \frac{d}{H} \right)^3 \right] \quad (6.4)$$

Hence, being  $\varepsilon$  the measurement strain value read on the measuring device and fixed as shown in Figure 64, and changing time by time the value of  $d$  itself, it is possible to compute the measured force value,  $N$ :

$$N = \frac{E\varepsilon (A_0 - bd)}{\left[ 3 - 3.14 \left( \frac{d}{H} \right) + 3.667 \left( \frac{d}{H} \right)^2 - 1.527 \left( \frac{d}{H} \right)^3 \right]} \quad (6.5)$$

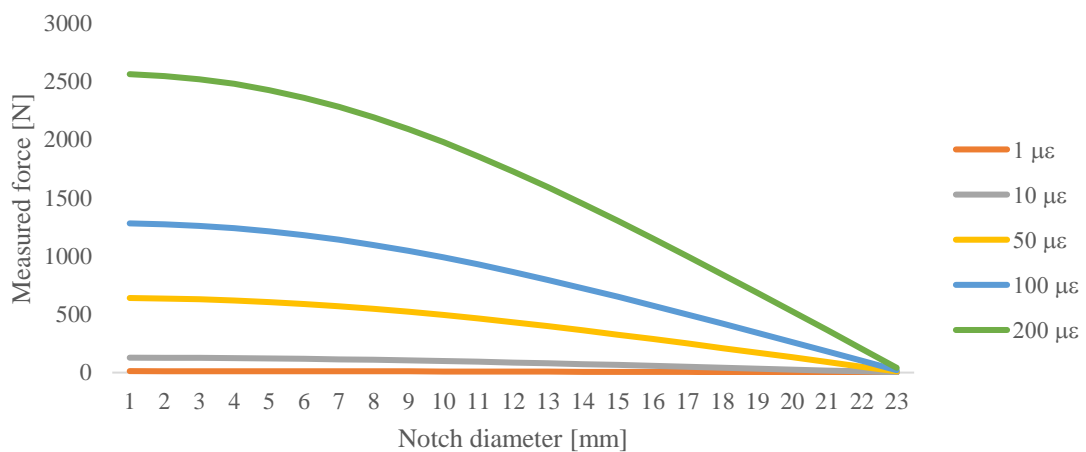


Figure 64: Measured forces vs Notch diameter for fixed strain values

In particular, when choosing a strain value equal to the floor noise computed in the paragraph 5.4.3, the measured force shows the trend of Figure 65, built up by using the data of Table 35. The chosen value ( $0.763 \mu\epsilon$ ) allows to be more conservative than using the floor noise value of  $0.638 \mu\epsilon$  registered in the paragraph 5.3 and refers directly to the measurement chain mounted on the link.

<b>d [mm]</b>	<b><math>k_t</math></b>	<b>N [N]</b>	<b>d [mm]</b>	<b><math>k_t</math></b>	<b>N [N]</b>	<b>d [mm]</b>	<b><math>k_t</math></b>	<b>N [N]</b>
1	2.88	9.78	9	2.26	7.98	17	2.07	3.81
2	2.76	9.72	10	2.22	7.55	18	2.06	3.21
3	2.66	9.61	11	2.18	7.09	19	2.05	2.61
4	2.57	9.46	12	2.16	6.59	20	2.05	2.01
5	2.49	9.26	13	2.13	6.07	21	2.04	1.40
6	2.42	9.01	14	2.11	5.53	22	2.03	0.78
7	2.36	8.71	15	2.10	4.97	23	2.01	0.16
8	2.30	8.36	16	2.08	4.40	24	2.00	-

Table 35: Measured force in function of notch diameter for a fixed strain value of  $0.763 \mu\epsilon$

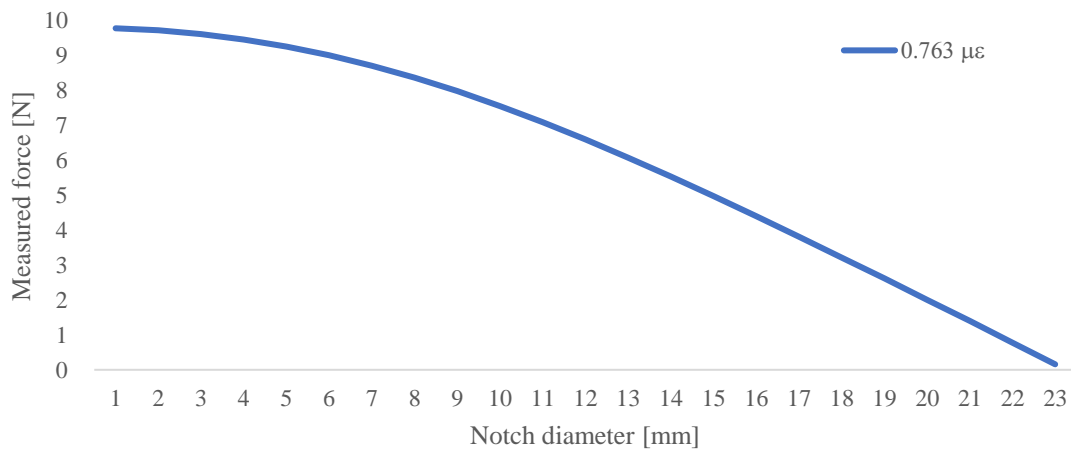


Figure 65: Measured force vs Notch diameter for a fixed strain value of  $0.763 \mu\epsilon$

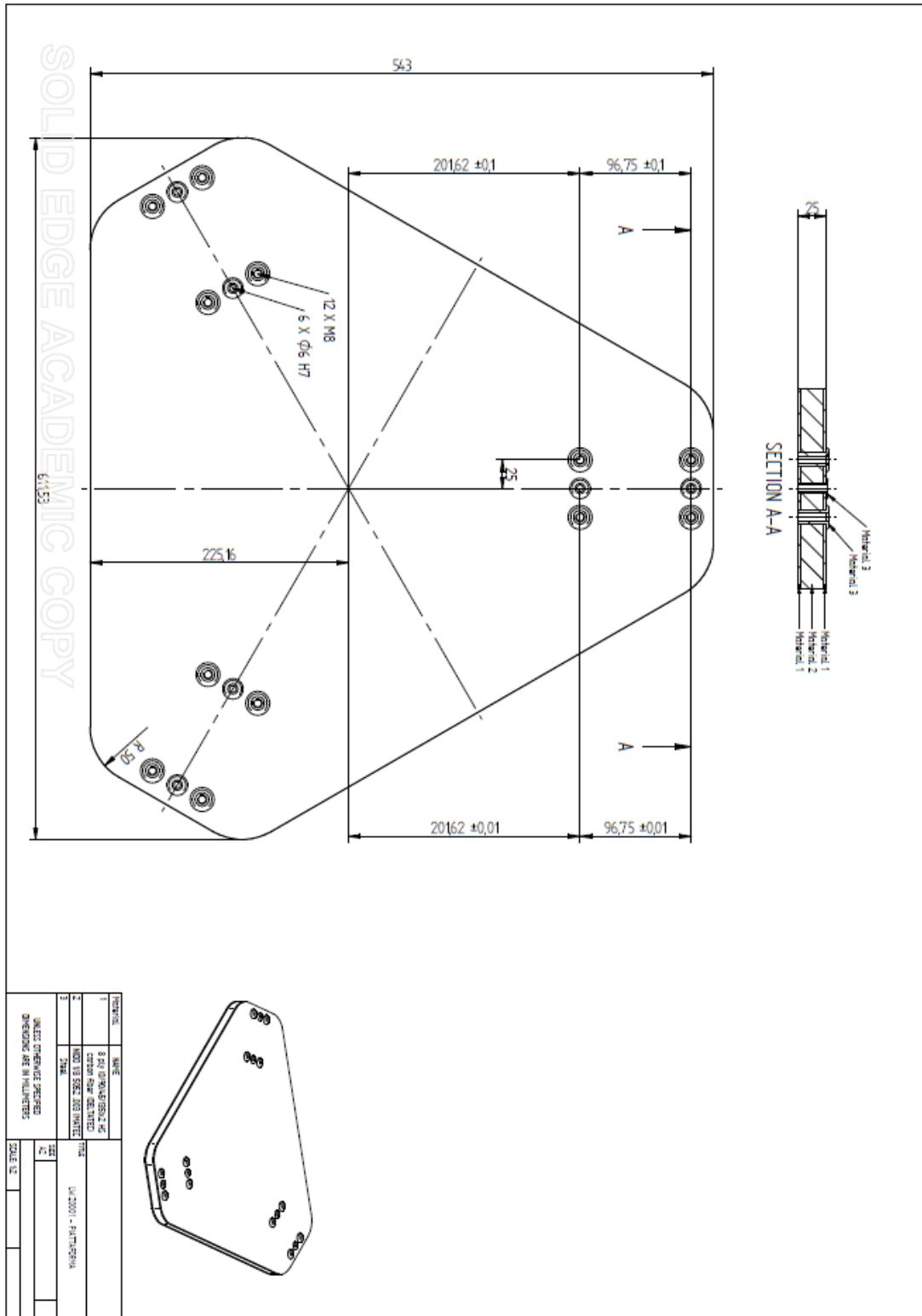
Hence, drilling 1 mm hole on the link body would make the system able to detect a force of 9.78 N, while increasing the hole diameter, better accuracy could be achieved. However, a limit on the hole diameter needs to be set, because a bigger hole would worsen the link stiffness, contributing to the overall decrease of the shaker bandwidth. For these reasons, a trade-off solution between the accuracy and the stiffness needs to be determined.

## Conclusions and remarks

The presented work intended to improve the performances and the employs of an existing multiaxial shaker for the measurement of WBV acting on a standing person. In order to extend the structure bandwidth up to 40 Hz, namely the range of frequencies inherent to the apparent mass studies, the first part of the work focused on the use of lightweight design principles and composite materials, so to redesign in a smarter way the most critical assembly parts in terms of mass and stiffness. In particular, the platform has been converted in a sandwich panel, made up of two skins of eight woven carbon fiber layers each, enclosing an aluminum honeycomb core, allowing the cut of 14 kg of redundant mass. Moreover, static simulations resulted in low levels of stresses and deflection, whereas proper models demonstrated that no mutual dynamic excitation would occur between the vibration modes of the platform and of the subject standing on it. Then, the second part of the work aimed to the realization of a force measurement system directly mounted on the platform, in order to ease the apparent mass matrix evaluation process. First, a set of equilibrium equations has been formulated, in order to establish the relationship among a generic wrench applied at the platform centre and the discharged forces on different points of the structure. After that, the same equations have been employed to demonstrate the unfeasibility of previous projects due to singularity issues related to the transformation matrices of the system. Then, a set of strain gauges connected in a Wheatstone's *full bridge type III* has been installed on one link, in order to evaluate the axial strains occurring on it, thus verifying linearity, hysteresis and repeatability of the measurements. From the obtained signals, a calibration curve and an uncertainty level have been derived. Furthermore, a MonteCarlo simulation has been run so as to estimate the MSE occurring between the axial forces measured on the links and the actual wrench acting at the platform centre. The final results witnessed errors of about 40 N on the measured forces and more than 4 Nm on the torque values, calling for a refinement in a possible future development, maybe reducing the measurement uncertainty. Finally, some advices on possible pre-conditioning of the signal have been proposed, including the installation of a low-pass filter to cancel out the floor noise or the creation of small holes on the links bodies, so as to naturally amplify the strain signal through a notch factor.

# Appendix A

## Platform mechanical drawings



# Appendix B

## MATLAB® script for instability

```

clc
close all
clear all

%Geometrical properties
Rp = sym('Rp'); %Platform radius [m]
t = sym('t'); %Platform thickness [m]
hlc = sym('hlc'); %Hypothetic load cell height [m]
hc = sym('hc'); %Cube height [m]
L = sym('L'); %Link length [m]
Rb = sym('Rb'); %Basement radius [m]
c = sym('c'); %Half of link clearance [m]
gamma = [0 120 240]*pi/180; %Fixed angles among the three joints

%End-effector coordinates and position vector
x=sym('x');
y=sym('y');
z=sym('z');
p=[x y z];

%Link angles in xy plane (theta) and xz plane (beta)
theta = [asin(((p(1))*sin(gamma(1)))+(p(2))*cos(gamma(1)))/L,
         asin(((p(1))*sin(gamma(1)))+(p(2))*cos(gamma(1)))/L,
         asin(((p(1))*sin(gamma(2)))+(p(2))*cos(gamma(2)))/L,
         asin(((p(1))*sin(gamma(2)))+(p(2))*cos(gamma(2)))/L,
         asin(((p(1))*sin(gamma(3)))+(p(2))*cos(gamma(3)))/L,
         asin(((p(1))*sin(gamma(3)))+(p(2))*cos(gamma(3)))/L)];
beta = [acos((Rb-Rp)/(L*cos(theta(1)))),acos((Rb-Rp)/(L*cos(theta(2)))),
        acos((Rb-Rp)/(L*cos(theta(3)))),acos((Rb-Rp)/(L*cos(theta(4)))),
        acos((Rb-Rp)/(L*cos(theta(5)))),acos((Rb-Rp)/(L*cos(theta(6))))];

%Transformation matrix construction
J_reduction = [eye(6), eye(6), eye(6)];
J_to_centre1 = [1 0 0 0 0 0; 0 1 0 0 0 0; 0 0 1 0 0 0;
               0 0 0 1 0 0; 0 0 Rp 0 1 0; 0 -Rp 0 0 0 1];
J_to_centre2 = [-0.5 sqrt(3)/2 0 0 0 0; -sqrt(3)/2 -0.5 0 0 0 0;
               0 0 1 0 0 0; 0 0 sqrt(3)*Rp/2 -0.5 sqrt(3)/2 0;
               0 0 -0.5*Rp -sqrt(3)/2 -0.5 0; 0 -Rp 0 0 0 1];
J_to_centre3 = [-0.5 -sqrt(3)/2 0 0 0 0; sqrt(3)/2 -0.5 0 0 0 0;
               0 0 1 0 0 0; 0 0 -sqrt(3)*Rp/2 -0.5 -sqrt(3)/2 0;
               0 0 -0.5*Rp sqrt(3)/2 -0.5 0; 0 -Rp 0 0 0 1];
J_to_centre = [J_to_centre1 zeros(6) zeros(6);
               zeros(6) J_to_centre2 zeros(6);
               zeros(6) zeros(6) J_to_centre3];
J_surface_i = [1 0 0 0 0 0; 0 1 0 0 0 0; 0 0 1 0 0 0;
               0 t 0 1 0 0; -t 0 0 0 1 0; 0 0 0 0 0 1];
J_surface = [J_surface_i zeros(6) zeros(6);
             zeros(6) J_surface_i zeros(6);
             zeros(6) zeros(6) J_surface_i];
M1 = J_to_centre*J_surface;
J_top_load_cell_i = [1 0 0 0 0 0; 0 1 0 0 0 0; 0 0 1 0 0 0;
                    0 hlc 0 1 0 0; -hlc 0 0 0 1 0; 0 0 0 0 0 1];

```

---

```

J_top_load_cell = [J_top_load_cell_i zeros(6) zeros(6);
                  zeros(6) J_top_load_cell_i zeros(6);
                  zeros(6) zeros(6) J_top_load_cell_i];
M2 = M1*J_top_load_cell;
J_bottom_load_cell_i = [1 0 0 0 0 0; 0 1 0 0 0 0;
                       0 0 1 0 0 0; 0 0.5*hc 0 1 0 0;
                       -0.5*hc 0 0 0 1 0; 0 0 0 0 0 1];
J_bottom_load_cell = [J_bottom_load_cell_i zeros(6) zeros(6);
                     zeros(6) J_bottom_load_cell_i zeros(6);
                     zeros(6) zeros(6) J_bottom_load_cell_i];
M3 = M2*J_bottom_load_cell;
J_cube_1 =
    [cos(theta(1))*cos(beta(1)) cos(theta(2))*cos(beta(2));
     sin(theta(1))*cos(beta(1)) sin(theta(2))*cos(beta(2));
     sin(beta(1)) sin(beta(2));
     c*sin(beta(1)), -c*sin(beta(2));
     0 0;
     -c*cos(theta(1))*cos(beta(1)) c*cos(theta(2))*cos(beta(2))];
J_cube_2 =
    [cos(theta(3))*cos(beta(3)) cos(theta(4))*cos(beta(4));
     sin(theta(3))*cos(beta(3)) sin(theta(4))*cos(beta(4));
     sin(beta(3)) sin(beta(4));
     c*sin(beta(3)), -c*sin(beta(4));
     0 0;
     -c*cos(theta(3))*cos(beta(3)) c*cos(theta(4))*cos(beta(4))];
J_cube_3 =
    [cos(theta(5))*cos(beta(5)) cos(theta(6))*cos(beta(6));
     sin(theta(5))*cos(beta(5)) sin(theta(6))*cos(beta(6));
     sin(beta(5)) sin(beta(6));
     c*sin(beta(5)), -c*sin(beta(6));
     0 0;
     -c*cos(theta(5))*cos(beta(5)) c*cos(theta(6))*cos(beta(6))];
J_cube = [J_cube_1 zeros(6,2) zeros(6,2);
          zeros(6,2) J_cube_2 zeros(6,2);
          zeros(6,2) zeros(6,2) J_cube_3];
M4 = M3*J_cube;

M5 = J_reduction*M4; %Transformation matrix

D=det(M5) %Determinant of the transformation matrix

subs(D,c,0) %Substitutes 0 to the link clearance variable 'c', so to
            verify if the singularity of M5 directly depends on it.
            If D becomes 0, then the singularity depends on it.

```

## Appendix C

### MATLAB® script for MonteCarlo simulation

```

clc
close all
clear all

%Geometrical and material properties
Rp = 0.250; %Platform radius [m]
t = 0.025; %Platform thickness [m]
hlc = 0; %Hypothetic load cell height [m]
hc = 0.094; %Cube height [m]
L = 0.215; %Link length [m]
Rb = 0.420; %Basement radius [m]
c = 0.080; %Half of link clearance (set to 0 in case of a single link)[m]
gamma = [0 120 240]*pi/180; %Fixed angles among the three joints
A = 558e-6; %Link cross-section [m^2]
E = 69e9; %Aluminum Young Modulus [N/m^2]

%End-effector position vector
p = [0 0 0]; %Three coordinates [m]

%Link angles in xy plane (theta) and xz plane (beta)
theta = [asin(((p(1))*sin(gamma(1))+(p(2))*cos(gamma(1)))/L),
         asin(((p(1))*sin(gamma(1))+(p(2))*cos(gamma(1)))/L),
         asin(((p(1))*sin(gamma(2))+(p(2))*cos(gamma(2)))/L),
         asin(((p(1))*sin(gamma(2))+(p(2))*cos(gamma(2)))/L),
         asin(((p(1))*sin(gamma(3))+(p(2))*cos(gamma(3)))/L),
         asin(((p(1))*sin(gamma(3))+(p(2))*cos(gamma(3)))/L)];
beta = [acos((Rb-Rp)/(L*cos(theta(1)))) , acos((Rb-Rp)/(L*cos(theta(2)))) ,
        acos((Rb-Rp)/(L*cos(theta(3)))) , acos((Rb-Rp)/(L*cos(theta(4)))) ,
        acos((Rb-Rp)/(L*cos(theta(5)))) , acos((Rb-Rp)/(L*cos(theta(6))))];

%MonteCarlo simulation

Load_vector = [10 100 1000]; %Examples of load modules
dim_MC = 10000; %Number of MonteCarlo iterations

for ii = 1:6
    for jj = 1:length(Load_vector)
        F_centre_final = [0 0 0 0 0 0];
        F_centre_final(ii) = Load_vector(jj);
        J_reduction = [eye(6), eye(6), eye(6)];

        J_to_centre1 = [1 0 0 0 0 0; 0 1 0 0 0 0; 0 0 1 0 0 0;
                        0 0 0 1 0 0; 0 0 Rp 0 1 0; 0 -Rp 0 0 0 1];
        J_to_centre2 = [-0.5 sqrt(3)/2 0 0 0 0; -sqrt(3)/2 -0.5 0 0 0 0;
                        0 0 1 0 0 0; 0 0 sqrt(3)*Rp/2 -0.5 sqrt(3)/2 0;
                        0 0 -0.5*Rp -sqrt(3)/2 -0.5 0; 0 -Rp 0 0 0 1];
        J_to_centre3 = [-0.5 -sqrt(3)/2 0 0 0 0; sqrt(3)/2 -0.5 0 0 0 0;
                        0 0 1 0 0 0; 0 0 -sqrt(3)*Rp/2 -0.5 -sqrt(3)/2 0;
                        0 0 -0.5*Rp sqrt(3)/2 -0.5 0; 0 -Rp 0 0 0 1];
    end
end

```

---

```

J_to_centre = [J_to_centre1 zeros(6) zeros(6);
               zeros(6) J_to_centre2 zeros(6);
               zeros(6) zeros(6) J_to_centre3];

J_surface_i = [1 0 0 0 0 0; 0 1 0 0 0 0; 0 0 1 0 0 0;
               0 t 0 1 0 0; -t 0 0 0 1 0; 0 0 0 0 0 1];

J_surface = [J_surface_i zeros(6) zeros(6);
             zeros(6) J_surface_i zeros(6);
             zeros(6) zeros(6) J_surface_i];

M1 = J_to_centre*J_surface;

J_top_load_cell_i = [1 0 0 0 0 0; 0 1 0 0 0 0; 0 0 1 0 0 0;
                    0 hlc 0 1 0 0; -hlc 0 0 0 1 0; 0 0 0 0 0 1];

J_top_load_cell = [J_top_load_cell_i zeros(6) zeros(6);
                  zeros(6) J_top_load_cell_i zeros(6);
                  zeros(6) zeros(6) J_top_load_cell_i];

M2 = M1*J_top_load_cell;

J_bottom_load_cell_i = [1 0 0 0 0 0; 0 1 0 0 0 0;
                       0 0 1 0 0 0; 0 0.5*hc 0 1 0 0;
                       -0.5*hc 0 0 0 1 0; 0 0 0 0 0 1];

J_bottom_load_cell = [J_bottom_load_cell_i zeros(6) zeros(6);
                     zeros(6) J_bottom_load_cell_i zeros(6);
                     zeros(6) zeros(6) J_bottom_load_cell_i];

M3 = M2*J_bottom_load_cell;

J_cube_1 =
[cos(theta(1))*cos(beta(1)) cos(theta(2))*cos(beta(2));
 sin(theta(1))*cos(beta(1)) sin(theta(2))*cos(beta(2));
 sin(beta(1)) sin(beta(2));
 c*sin(beta(1)), -c*sin(beta(2));
 0 0;
 -c*cos(theta(1))*cos(beta(1)) c*cos(theta(2))*cos(beta(2))];

J_cube_2 =
[cos(theta(3))*cos(beta(3)) cos(theta(4))*cos(beta(4));
 sin(theta(3))*cos(beta(3)) sin(theta(4))*cos(beta(4));
 sin(beta(3)) sin(beta(4));
 c*sin(beta(3)), -c*sin(beta(4));
 0 0;
 -c*cos(theta(3))*cos(beta(3)) c*cos(theta(4))*cos(beta(4))];

J_cube_3 =
[cos(theta(5))*cos(beta(5)) cos(theta(6))*cos(beta(6));
 sin(theta(5))*cos(beta(5)) sin(theta(6))*cos(beta(6));
 sin(beta(5)) sin(beta(6));
 c*sin(beta(5)), -c*sin(beta(6));
 0 0;
 -c*cos(theta(5))*cos(beta(5)) c*cos(theta(6))*cos(beta(6))];

```



---

```

J_cube = [J_cube_1 zeros(6,2) zeros(6,2);
          zeros(6,2) J_cube_2 zeros(6,2);
          zeros(6,2) zeros(6,2) J_cube_3];

M4 = M3*J_cube;

M5 = J_reduction*M4;

N = M5\F_centre_final';

strain = N/(E*A); %derived strain vector from axial components

u = 7.63e-7; %uncertainty from floor noise

error = u*randn(6,dim_MC); %generates random error from a normal
distribution with standard deviation equal to u

strain_mat = ones(6,dim_MC).*strain;

strain_mat_err = strain_mat+error;

N_mat = strain_mat_err*E*A;
%recreates the axial forces on the links adding the error

F_centre_final_mat = M5*N_mat;
%recreates the forces at the platform centre adding the error

%Mean Squared Error calculation

Load_vector_mat = zeros(6,dim_MC);

Load_vector_mat(ii,:) = Load_vector_mat(ii,:)+Load_vector(jj);

MSE = sqrt(mean(((F_centre_final_mat-Load_vector_mat).^2)'));

eval('res.loadlevel',num2str(jj),'.loaddir',num2str(ii),'=MSE;');
%recreates a structured matrix including the MSEs over the six directions
of measurement and for each load level.

end
end

```

---

# Bibliography

- [1] C. Nelson, *Vibration Test Evolution. Single-Axis, Single-Shaker to 6DoF*, Burlington, WA: TeamCorporation, 2002.
- [2] J. Roesch, "Electrodynamic vs Hydraulic Shakers: Which is best for your product?," Austin Reliability Labs, 2019. [Online]. Available: <https://www.austinrl.com/electrodynamic-vs-hydraulic-shakers-which-is-best-for-your-product/>.
- [3] C. Harman, "Historical development of high performance multi-axial vibration test systems," *MIRA New Technology*, pp. 128-130, 2003.
- [4] MTS Product Catalogue, "MAST™ (Multi-axial Simulation Table) Systems," MTS, 2018. [Online]. Available: <https://www.mts.com>.
- [5] Sentek Dynamics, "Simultaneous three axis (MA-series) shakers," 2018. [Online]. Available: <https://www.sentekdynamics.com/three-axis-system-shakers>.
- [6] IMV Corporation, "TS-series (3-axis simultaneous systems)," 2018. [Online]. Available: <https://www.imv.co.jp/e/products/vibrationtest/axis/tsseries/>.
- [7] E. Habtour, D. Mortin, C. Choi and others, "Improved Reliability Testing and Modeling of Electronics with Multi-DOF Vibration in Unmanned Army Ground Vehicles," in *2010 NDIA Ground Vehicle Systems Engineering and Technology Symposium*, Dearborn, MI, 2010.
- [8] P. Nataletti, E. Marchetti, A. Lunghi and others, "Occupational exposure to mechanical vibration: the Italian vibration database for risk assessment," *International Journal of Occupational Safety and Ergonomics*, vol. 14, no. 4, pp. 379-386, 2008.
- [9] Centro Ricerche INAIL, *ISPESL 353 Multi-Axis Simulation Table (MAST) System Performance*, Monte Porzio Catone, Rome, 2008.
- [10] Robot Institute of America, *Definition of Robot*, Dearborn, MI, 1979.
- [11] Z. Pandilov and V. Dukovski, "Comparison of the characteristics between serial and parallel robots," *Acta Technica Corviniensis - Bulletin of Engineering*, vol. VII, no. 1, 2014.
- [12] Y. Li, D. Shang, X. Fan and others, "Motion Reliability Analysis of the Delta Parallel Robot considering Mechanism Errors," *Mathematical Problems in Engineering*, vol. 1, pp. 1-10, 2019.
- [13] P. Marzaroli, A. Albanetti, E. Negri and others, "Design and Testing of a 3-DOF robot for studying the human response to vibration," *Machines*, vol. 7, no. 4, p. 67, 2019.
- [14] A. Albanetti, *Model and test of a 3 DOF shaker for the study of human response to multiaxial vibrations*, Politecnico di Milano: M. Sc. thesis, 2018.

- 
- [15] M. Elgeziry, *Modelling the dynamic behaviour of 3D shakers for testing the human response to vibration*, Politecnico di Milano: M. Sc. thesis, 2018.
- [16] E. Negri, *3D shaker. Vibrating machine used for tests designed to damp and reduce vibrations harmful to the human body*, Politecnico di Milano: M. Sc. thesis, 2018.
- [17] M. Valsecchi, *Whole body vibration in kitesurfing*, Politecnico di Milano: M. Sc. thesis, 2010.
- [18] S. Maugeri, *Modelling the response of the human feet to vertical whole-body vibration*, Politecnico di Milano: M. Sc. thesis, 2019.
- [19] M. J. Griffin, *Handbook of human vibrations*, London: Academic Press, 1990.
- [20] N. Mansfield, *Human Response to Vibration*, New York: CRC Press, 2004.
- [21] C. Berlin and C. Adams, *Production Ergonomics: Designing Work Systems to Support Optimal Human Performance*, London: Ubiquity Press, 2017.
- [22] D. Wieckowski, *An attempt to estimate natural frequencies of parts of child body*, Warszawa: Automotive Industry Institute, 2012.
- [23] M. Della Pasqua, A. Messineo and S. Battistini, *Vibrazioni meccaniche negli ambienti di lavoro*, Roma: EPC Libri, 2006.
- [24] European Agency for Safety and Health at Work, *OSH in figures - Work-related musculoskeletal disorders in the EU - Facts and figures*, Luxembourg, 2010.
- [25] European Agency for Safety and Health at Work, *Workplace exposure to vibration in Europe: an expert review*, Luxembourg, 2008.
- [26] European Parliament, *Directive 2002/44/EC of the European Parliament and of the Council*, Luxembourg, 2002.
- [27] Ministero del Lavoro e delle Politiche Sociali, *D.lgs. 9 aprile 2008, n. 81 - Testo Unico sulla salute e sicurezza sul lavoro*, Roma, 2008.
- [28] M. Bovenzi, "Low back pain disorders and exposure to whole-body vibration in the workplace," *Seminars in Perinatology*, vol. 20, no. 1, pp. 38-53, 1996.
- [29] M. Bovenzi, "An overview of low back pain and occupational exposures to whole-body vibration and mechanical shocks," *Med Lav.*, pp. 108(6): 419-433, 2017.
- [30] L. E. Charles, C. C. Ma, C. M. Burchfiel and others, "Vibration and Ergonomic Exposures Associated With Musculoskeletal Disorders of the Shoulder and Neck," *Saf Health Work*, p. 9(2): 125-132, 2018.
- [31] UNI ISO, *2631-1: 2014 - Mechanical vibration and shock: Evaluation of human exposure to whole-body vibration*, International Standard, 2014.

- 
- [32] Acoustic Glossary, "Frequency Weighting Terms, Definitions, Units, Measurements," [Online]. Available: <http://www.acoustic-glossary.co.uk/frequency-weighting.htm>.
- [33] N. Shibata, "Subjective response of standing persons exposed to fore-aft, lateral and vertical whole-body vibration," *International Journal of Industrial Ergonomics*, vol. 49, pp. 116-123, 2015.
- [34] G. H. M. J. Subashi, Y. Matsumoto and M. J. Griffin, "Apparent mass and cross-axis apparent mass of standing subjects during exposure to vertical whole-body vibration," *Journal of Sound and Vibration*, vol. 293, pp. 78-95, 2006.
- [35] M. Tarabini, S. Solbiati, B. Saggin and others, "Apparent mass matrix of standing subjects," *Ergonomics*, vol. 59, no. 8, pp. 1038-1049, 2016.
- [36] Y. Matsumoto and M. J. Griffin, "Mathematical models for the apparent masses of standing subjects exposed to vertical whole-body vibration," *Journal of Sound and Vibration*, vol. 260, pp. 431-451, 2003.
- [37] R. Bekhti, *Geometrical, mechanical and transduction techniques for designing multi-axis force-torque sensors for robotic applications*, Université du Québec - Montréal: Ph. D. thesis, 2015.
- [38] C. Kang, "Closed-form force sensing of a 6-axis force transducer based on the Stewart platform," *Sensors and Actuators A: Physical*, vol. 90, no. 1-2, pp. 31-37, 2001.
- [39] B. Kirking, J. Krevolin, C. Townsend and others, "A multiaxial force-sensing implantable tibial prosthesis," *Journal of Biomechanics*, vol. 39, no. 9, pp. 1744-1751, 2006.
- [40] G. Sommer, M. Eder, L. Kovacs and others, "Multiaxial mechanical properties and constitutive modeling of human adipose tissue: A basis for preoperative simulations in plastic and reconstructive surgery," *Acta Biomaterialia*, vol. 9, no. 11, pp. 9036-9048, 2013.
- [41] G. Sommer, A. Schriefl, A. Zeindlinger and others, "Multiaxial mechanical response and constitutive modeling of esophageal tissues: Impact on esophageal tissue engineering," *Acta Biomaterialia*, vol. 9, no. 12, pp. 9379-9391, 2013.
- [42] A. Bejczy, "Smart sensors for smart hands," in *Conference on smart sensors*, Hampton, VA, 1979.
- [43] S. Hogleve and K. Tracht, "Design and implementation of multiaxial force sensing gripper fingers," *Production Engineering*, vol. 8, no. 6, pp. 765-772, 2014.
- [44] G. Kim, "Design of a six-axis wrist force/moment sensor using FEM and its fabrication for an intelligent robot," *Sensors and Actuators A: Physical*, vol. 133, no. 1, pp. 27-34, 2007.
- [45] C. Jacq, B. Lüthi, T. Maeder and others, "Thick-film multi-DOF force/torque sensor for wrist rehabilitation," *Sensors and Actuators A: Physical*, vol. 162, no. 2, pp. 361-366, 2010.
- [46] K. Kim, J. Park, J. Su and others, "3D printing of multiaxial force sensors using carbon nanotube (CNT)/thermoplastic polyurethane (TPU) filaments," *Sensors and Actuators A: Physical*, vol. 263, pp. 493-500, 2017.

- 
- [47] J. Yao, H. Zhang, X. Xiang and others, "A 3-D printed redundant six-component force sensor with eight parallel limbs," *Sensors and Actuators A: Physical*, vol. 247, pp. 90-97, 2016.
- [48] J. Yao, D. Cai, H. Zhang and others, "Task-oriented design method and research on force compliant experiment of six-axis wrist force sensor," *Mechatronics*, vol. 35, pp. 109-121, 2016.
- [49] K. A. Morris, "Has Force/Torque Sensing Gained Factory Acceptance?," in *Proceedings of the 1992 IEEE/RSJ International Conference on Intelligent Robots and Systems*, Raleigh, NC, 1992.
- [50] Y. Sun, L. Liu, T. Zou and others, "Design and optimization of a novel six-axis force/torque sensor for space robot," *Measurement*, vol. 65, pp. 135-148, 2015.
- [51] D. Chen, A. Song and A. Li, "Design and Calibration of a Six-axis Force/torque Sensor with Large Measurement Range Used for the Space Manipulator," *Procedia Engineering*, vol. 99, pp. 1164-1170, 2015.
- [52] B. Dasgupta and T. S. Mruthyunjaya, "The Stewart platform manipulator: a review," *Mechanism and Machine Theory*, vol. 35, no. 1, pp. 15-40, 2000.
- [53] A. Gaillet and C. Reboulet, "An isostatic six component force and torque sensor," in *Proceedings of the 13th International Symposium of Industrial Robots*, Chicago, IL, 1983.
- [54] D. R. Kerr, "Analysis, properties and design of a Stewart-platform transducer," *ASME Journal of Mechanical Design*, vol. 111, no. 1, pp. 25-28, 1989.
- [55] M. M. Svinin and M. Uchiyama, "Optimal Geometric Structures of Force/Torque Sensors," *The International Journal of Robotics Research*, vol. 14, no. 6, pp. 560-573, 1995.
- [56] T. A. Dwarakanath, B. Dasgupta and T. S. Mruthyunjaya, "Design and development of a Stewart platform based force–torque sensor," *Mechatronics*, vol. 11, no. 7, pp. 793-809, 2001.
- [57] Q. Jiang and C. M. Gosselin, "Determination of the maximal singularity-free orientation workspace for the Gough–Stewart platform," *Mechanism and Machine Theory*, vol. 44, no. 6, pp. 1281-1293, 2009.
- [58] R. Ranganath, P. S. Nair, T. S. Mruthyunjaya and others, "A force–torque sensor based on a Stewart Platform in a near-singular configuration," *Mechanism and Machine Theory*, vol. 39, no. 9, pp. 971-998, 2004.
- [59] I.MA.TEC. Product Catalogue, "5052 Alloy Hexagonal Aluminum Honeycomb – Specification Grade," I.MA.TEC., 2016. [Online]. Available: <https://www.imatec.it/wp-content/uploads/2016/05/Nido-dape-alluminio-5052-IT-7.pdf>.
- [60] Delta-Tech Product Catalogue, "UD Tapes," Delta-Tech, 2009. [Online]. Available: [https://www.delta-tech.it/products.php?m=2&item=ud\\_tapes](https://www.delta-tech.it/products.php?m=2&item=ud_tapes).

- [61] B. Tuberosa, *Proprietà meccaniche a trazione di compositi polimerici rinforzati con fibre lunghe di carbonio di interesse per il settore automotive*, Università di Bologna: B. A. Thesis, 2012.
- [62] M. R. Ruiz, *Design and analysis of a Stewart-platform-based six-axis load cell*, Massachusetts Institute of Technology - Cambridge, MA: B. A. Thesis, 2017.
- [63] K. Hoffmann, *Applying the Wheatstone bridge*, Darmstadt: Hottinger Baldwin Messtechnik GmbH.
- [64] P. Marzaroli, *Taratura statica di un trasduttore di spostamento induttivo - Misure Meccaniche e Termiche*, Politecnico di Milano - Milano: Course notes, 2018.
- [65] C. M. Stewart, *Mechanical Design ME334*, UTEP - El Paso, TX: Course notes, 2018.